

# **Mitotic Dynamics of Normally and Mis-attached Chromosomes and Post-mitotic Behavior of Missegregated Chromosomes**

**Bin He**

Dissertation submitted to the faculty of the Virginia Polytechnic Institute and State University in partial fulfillment of the requirements for the degree of

Doctor of Philosophy  
In  
Biological Sciences

Daniela Cimini  
Gul Civelekoglu-Scholey  
Richard A. Walker  
Jianhua Xing  
William R. Huckle

April 28, 2015  
Blacksburg, VA

Keywords: Mitosis; chromosome; spindle; kinetochore; computational model; micronucleus

Copyright 2015 Bin He

# **Mitotic Dynamics of Normally and Mis-attached Chromosomes and Post-mitotic Behavior of Missegregated Chromosomes**

**Bin He**

## **Abstract**

Equal segregation of the replicated genomic content to the two daughter cells is the major task of mitotic cells. The segregation is controlled by a complex system in the cell and relies mainly on the interaction between microtubules (MTs) of the mitotic spindle and kinetochores (KTs), specialized protein structures that assemble on each chromatid of each mitotic chromosome. By combining computational modeling and quantitative light microscopy, we established a quantitative model of the forces and regulators controlling metaphase chromosome movement in the mammalian cell line derived from *Potorous tridactylis* kidney epithelial cells (PtK1) (Chapter 2). This model can explain key features of metaphase chromosome dynamics and related chromosome structural changes experimentally observed. Moreover, the model made predictions, which we tested experimentally, on how changes in spindle dynamics affect certain aspects of chromosome structure. This quantitative model was next used to study the metaphase dynamics of chromosomes with erroneous KT-MT attachments (Chapter 3). Once again, the model predictions were tested experimentally and showed that erroneous KT-MT attachment alters the dynamics not only of the mis-attached KT, but also of its sister KT. Even more strikingly, experimental data showed that the presence of a single mis-attached KT could perturb the dynamics of all other, normally attached, KT in anaphase. Chapter 3 also describe how MT poleward flux ensures correct KT-MT attachment and correct chromosome segregation. Indeed, reduced flux is associated with an increase in merotelically attached anaphase lagging chromosomes (LCs). These LCs form micronuclei (MNI) upon mitotic

exit. The final effort of this work focused on the fate of MNi and micronuclated (MNed) cells (Chapter 4). Experimental observations showed that most of the chromosomes in MNi missegregated at the cell division following MN formation and that frequently the chromatin in the MN displayed delayed condensation. This work, thus, established a direct link between LCs and aneuploidy through the MN cell cycle.

## **Dedication**

To my beloved family

## Acknowledgements

This dissertation would have not been possible without the guidance from my committee members and support from my family and friends.

First, I would like to express my deepest gratitude to Dr. Daniela Cimini, my advisor and chair of my committee. Daniela is a great scientist who is passionate about research, and more importantly, she is an amazing mentor. Daniela has taught me how to perform and present research, how to achieve high scientific standards, and has helped me tremendously throughout my PhD career in many aspects.

I am grateful to all my committee members for the guidance and encouragement over the years. Special thanks are due to Dr. Gul Civelekoglu-Scholey, who has introduced me to the world of computational biology, and she showed me how to look at experimental biology from a quantitative perspective. Her input has been very important in the process of my dissertation. Dr. William Huckle has asked a lot of inspiring questions that have stimulated my deeper thoughts, and he has provided suggestions that helped me improve my research. Dr. Richard Walker has always carefully evaluated all the results that I presented to him, and has patiently read my dissertation and provided valuable feedback. Dr. Jianhua Xing has generously shared his time and insight during our many discussions. He has provided unique and inspiring advice on many of the problems I worked on.

I am also indebted to the Department of Biological Sciences. Great thanks are due to Dr. Brenda Winkel for her advice and encouragement to help me grow toward a well-rounded scholar. I would cherish my time in the Department with all my friends and fellow graduate students, especially all the past and present members of the Cimini Lab, without whom it would not have been so much fun.

Most importantly, none of this would have been possible without the love of my family. I would like to thank my parents Jingsheng He and Fengqin Liu, and my wife Sihui Zhang, for their love and patience. My gratitude towards them is beyond words. Special thanks to my son Leonardo He. He has brought so much joy in my life.

# Table of contents

<b>Abstract</b> .....	<b>ii</b>
<b>Dedication</b> .....	<b>iv</b>
<b>Acknowledgements</b> .....	<b>v</b>
<b>Abbreviation list</b> .....	<b>xi</b>
<b>Chapter 1. Literature Review</b> .....	<b>1</b>
1.1. Overview.....	1
1.2. Mitotic chromosome segregation.....	4
1.3. The mitotic apparatus.....	5
1.3.1. <i>The mitotic spindle</i> .....	5
1.3.2. <i>Mitotic chromosomes</i> .....	6
1.3.3. <i>Centromere and KT</i> .....	8
1.4. The dynamics of mitosis.....	9
1.4.1. <i>Mitotic spindle assembly mechanisms</i> .....	9
1.4.2. <i>KT-MT attachment and the spindle assembly checkpoint</i> .....	10
1.4.3. <i>Metaphase, chromosome oscillations, and microtubule dynamics</i> .....	13
1.4.4. <i>Anaphase chromosome segregation</i> .....	14
1.4.5. <i>Telophase: completion of mitosis</i> .....	16
1.4.6. <i>Cytokinesis</i> .....	17
1.5. Causes of chromosome mis-segregation.....	18
1.5.1. <i>Spindle assembly checkpoint defects</i> .....	18
1.5.2. <i>Cohesion defects</i> .....	20
1.5.3. <i>Merotelic KT attachment</i> .....	20
1.5.4. <i>Multipolar mitotic spindles and centrosome abnormalities</i> .....	21
1.5.5. <i>Defective correction of KT-MT mis-attachments</i> .....	22
<b>Chapter 2. Dynamic bonds and polar ejection force distribution explain kinetochore oscillations in PtK1 cells</b>	<b>36</b>
2.1. Abstract.....	37
2.2. Introduction.....	37
2.3. Results.....	39
2.3.1. <i>Dynamics of metaphase chromosomes in PtK1 cells: oscillating and steady KT pairs</i> .....	39
2.3.2. <i>Force-Balance model for metaphase chromosome dynamics in PtK1 cells</i> .....	40
2.3.3. <i>New mathematical model: KT attachment to MTs through dynamic non-motor, viscoelastic bonds</i> .....	42
2.3.4. <i>Model results: robust attachment of KTs to spindle MTs, and oscillations of middle sister KT pairs</i> .....	44
2.3.5. <i>Model results: identification of parameters that suppress oscillations of the peripheral KT pairs</i> .....	47
2.3.6. <i>Model predictions and experimental tests</i> .....	48
2.4. Discussion.....	50
2.4.1. <i>What causes the inhomogeneity in the distribution of PEFs within the PtK1 cells metaphase spindle?</i> .....	50
2.4.2. <i>Comparison with previous models</i> .....	51

2.4.3. <i>The importance of understanding kinetochore dynamics</i> .....	54
2.5. Materials and Methods .....	55
2.5.1. <i>Experimental methods</i> .....	55
2.5.2. <i>Modeling methods</i> .....	59
2.6. <i>Supplemental material</i> .....	70
Acknowledgements .....	72
<b>Chapter 3. Metaphase and anaphase chromosome dynamics in cells with normal versus merotelic KT attachment and role of MT poleward flux in correction of merotelic attachment</b> .....	<b>91</b>
3.1. Abstract .....	92
3.2. Introduction.....	92
3.3. Results and Discussion.....	94
3.3.1. Metaphase dynamics of merotelic KTs .....	94
3.3.2. <i>Role of MT poleward flux in correction of KT mis-attachments</i> .....	94
3.3.3. <i>Anaphase KT/chromosome dynamics</i> .....	96
3.3.4. <i>How does kif2a inhibition affect anaphase chromosome dynamics</i> .....	98
3.4. Materials and Methods .....	99
3.4.1. <i>Cell culture</i> .....	99
3.4.2. <i>Microinjection</i> .....	99
3.4.3. <i>Microscopy and image acquisition</i> .....	100
3.4.4. <i>Kinetochore tracking</i> .....	100
3.4.5. <i>Photoactivation of PAGFP-Tubulin</i> .....	101
3.4.6. <i>MT poleward flux quantification</i> .....	101
<b>Chapter 4. Chromosomes missegregated into micronuclei contribute to CIN by missegregating at the next division</b> <b>112</b>	
4.1. Abstract .....	113
4.2 Introduction.....	114
4.3 Results and Discussion.....	116
4.3.1. <i>Cells with whole-chromosome MNi are as likely as non-MNed cells to enter mitosis</i> .....	116
4.3.2. <i>MNed cells display high rates of chromosome segregation errors and further MN formation</i> .....	117
4.3.3. <i>The mnChr is responsible for the segregation errors</i> .....	118
4.3.4. <i>Delayed condensation of the mnChr and cytokinesis failure in MNed cells</i> .....	119
4.3.5. <i>Conclusion</i> .....	121
4.4. Materials and Methods .....	122
4.4.1. <i>Generation of H2B-PAGFP PtK1 cell line</i> .....	122
4.4.2. <i>Cell culture and treatment</i> .....	122
4.4.3. <i>Immunofluorescence staining, image acquisition, and image analysis</i> .....	123
4.4.4. <i>Phase-contrast live-cell imaging</i> .....	124
4.4.5. <i>Chromosome photoactivation and imaging</i> .....	125
<b>Chapter 5. Conclusions and future directions</b> .....	<b>140</b>
<b>References</b> .....	<b>143</b>

## List of Figures

Figure 1.1. Overview of mitosis .....	24
Figure 1.2. Structure of centrosome and microtubule .....	26
Figure 1.3. Metaphase human chromosome Structure of metaphase human chromosome .....	27
Figure 1.4. KT structure .....	28
Figure 1.5. Chromosome segregation produced by different KT–MT attachments.....	29
Figure 1.6. Spindle assembly checkpoint (SAC) and completion of mitosis .....	30
Figure 1.7. Structures that mediate cytokinesis .....	31
Figure 1.8. Pathways to the generation of aneuploidy .....	32
Figure 1.9. Cells with persistently activated SAC.....	33
Figure 2.1. Middle and peripheral sister KT pairs at the metaphase plate display significant differences in dynamics .....	74
Figure 2.2. Middle and peripheral KT pairs display similar inter- and intra-KT distances .....	75
Figure 2.3. Similar amounts of KT motors (CENP-E and dynein) accumulate at middle and peripheral KTs .....	76
Figure 2.4. FB model description .....	78
Figure 2.5. A model based on dynamic viscoelastic KT–MT bonds reproduces the dynamic behavior of middle sister KT pairs .....	80
Figure 2.6. A nonlinear distribution of PEFs can suppress the oscillations of peripheral sister. KT pairs .....	83
Figure 2.7. Inter-KT hyperstretching caused by reduced kMT detachment rates can be rescued by simultaneous reduction of MT poleward flux .....	84
Figure 3.1. Merotelic KT attachment changes the oscillation pattern of the normally attached sister.....	104
Figure 3.2. Microinjection of anti-Kif2a antibodies results in reduced MT poleward flux and induces high rates of anaphase lagging chromosomes .....	106
Figure 3.3. Quantification of MT dynamics by FDAP in buffer- vs. anti-Kif2a-injected cells. ....	108
Figure 3.4. Anaphase KT dynamics .....	109
Figure 3.5. Rates of KT poleward movement are reduced in anaphase cells with a merotelically attached LC.....	110
Figure 3.6. KT poleward movement in buffer vs. anti-Kif2a-injected HEC1-GFP PtK1 cells.....	111
Figure 4.1. MNed PtK1 cells progress through the cell cycle and maintain integrity of MN envelope.....	129
Figure 4.2. High rates of chromosome segregation errors in MNed cells.....	131
Figure 4.3. MN photoactivation shows that the mnChr is responsible for the segregation errors observed in MNed cells .....	133
Figure 4.4. Delayed chromosome condensation of mnChrs.....	135
Figure 4.5. Cytokinesis failure in MNed cells.....	137

## List of Tables

Table 1.1. Motor Proteins in Spindle Assembly.....	34
Table 1.2. Molecular components of the spindle assembly checkpoint (SAC).....	35
Table 2.1. Model assumptions.....	86
Table 2.2. Model test for suppression of KT oscillations.....	87

## Abbreviation list

KT/KTs = Kinetochore/Kinetochores

kMTs = kinetochore microtubules

LC/LCs = Lagging chromosome/Lagging chromosomes

MN/MNi = Micronucleus/Micronuclei

MT/MTs = Microtubule/Microtubules

ND = Chromosome nondisjunction

NOC = Nocodazole

STLC = S-trityl-L-cysteine

FB = Force-balance

P = Poleward

AP = away-from-the-pole

mnChr(s) = Micronuclear chromosome(s)

MNed = Micronucleated

CIN = Chromosomal instability

# Chapter 1. Literature Review

## 1.1. Overview

Correct chromosome segregation during cell division is one of the mechanisms responsible for maintaining genome stability. Accurate chromosome segregation relies on both the interplay of numerous biochemical pathways that control cell division and on the interplay of mechanics and dynamics of mitotic apparatus components, which produce the forces necessary to achieve correct segregation and prevent chromosome segregation errors. Erroneous chromosome segregation leads to gain or loss of chromosomes, which will yield cells with aberrant chromosome number (aneuploid cells)(Cimini and Degrossi, 2005; Cimini et al., 2002; Cimini et al., 2001). This will affect the function and viability of offspring cells (Storchova and Kuffer, 2008; Weaver et al., 2007; Williams et al., 2008), and hence the development and survival of an organism (Sumner, 2003).

Aneuploidy, arising in either germ cells or somatic cells, can cause disease in humans. Chromosome mis-segregation in meiosis results in the production of aneuploid gametes, which will give rise to zygotes with abnormal chromosome number. Most aneuploid zygotes do not survive and result in miscarriage (Sumner, 2003). Even in those few cases in which aneuploidy is not lethal (e.g., monosomy X or trisomy 21), severe mental and physical problems are observed (Munne and Cohen, 1998). Aneuploidy can also arise in post-zygotic mitotic divisions, leading to mosaic embryos. Interestingly, mosaicism is more frequently observed than complete aneuploidy in early human embryos (Munne, 2006;

Munne and Cohen, 1998), and it is generally associated with serious birth defects. A severe post-birth human disease, named mosaic variegated aneuploidy (MVA), is a syndrome characterized by mosaic aneuploidy, predominantly trisomies and monosomies involving multiple chromosomes and tissues. This syndrome is associated with high risk of cancer (12 of 35 reported MVA cases) (Hanks et al., 2004; Hanks et al., 2006), demonstrating that aneuploidy can have deleterious effects on organism survival.

Spontaneous chromosome mis-segregation is also observed in healthy humans, as well as in other mammals. Every second about 10 million cell divisions occur in a human adult (Weinberg, 2006). About  $10^{16}$  cells are generated from cell division in an average human lifespan. This enormous number of cell divisions puts our body at high risk of having chromosome mis-segregation, even if the frequency of mis-segregation is low. In normal human brain, which contains about one trillion cells, 4% cells are constitutively aneuploid for chromosome 21 (Rehen et al., 2005). Chromosome 17 also shows high rates of aneuploidy in normal human brain (Mosch et al., 2007). Correspondingly, approximately 33% of mouse neuroblasts are identified as aneuploid, with 98% of them being hypoploid (missing chromosomes). In these neuroblasts, lack of individual chromosomes ranges between 1.6% and 8.4%, while chromosome gain (hyperploidy) is always less than 2% (Rehen et al., 2001). Another type of primary cells whose karyotype has been extensively studied is peripheral blood lymphocytes. Spontaneous aneuploidy in uncultured and cultured human lymphocytes ranges between 0.03% and about 10% for a single chromosome (Catalan et al., 2000; Cimini, 2008; Minissi et al., 1999). How such high rates of aneuploidy occur and whether the consequent gene dosage unbalances harm the organism is still unclear.

Notably, high rates of chromosome mis-segregation and aneuploidy are consistently observed in human cancers (Cimini, 2008; Weaver and Cleveland, 2006), and numerous studies indicated a potential role of aneuploidy in cancer development. Indeed, studies in animal models have shown that aneuploidy-inducing mutations (e.g., BUB1B, MAD2, CENP-E haploinsufficiency) correlated with high rates of cancer (Hanks et al., 2004; Michel et al., 2001; Weaver et al., 2007). However, other observations indicate that in some contexts aneuploidy can suppress tumor growth (Weaver et al., 2007; Williams et al., 2008). Although further effort is needed to clarify the complex effect of aneuploidy, many observations support (and somewhat extend) the hypothesis, proposed by Theodor Boveri in 1902 (Boveri, 1914; Boveri, 2008), that aneuploidy drives tumor progression (Holland and Cleveland, 2009). Uncovering the mechanisms of chromosome mis-segregation will provide important information for cancer prognosis and will help identify promising targets for anticancer therapy (Holland and Cleveland, 2009; Rajagopalan and Lengauer, 2004).

Given the role of accurate chromosome segregation in preventing aneuploidy and disease, understanding the cellular mechanisms controlling chromosome segregation is of utmost importance. The work described in the first part of this dissertation (Chapters 2-3) focuses on understanding how the mechanics and dynamics of the mitotic apparatus regulate chromosome movement and correction of KT mis-attachments. Because the mitotic apparatus is constituted by many components, which interact in complex ways to produce the forces necessary to move chromosomes, we combined experimental and computational approaches to address our specific questions from a system-level perspective. Despite the existence of multiple pathways responsible for ensuring accurate chromosome segregation, errors can occur in mitosis. A common chromosome segregation error observed in both

normal and cancer cells is the anaphase lagging chromosome (LC) (Cimini et al., 2001; Thompson and Compton, 2008), which is a chromosome persists at or near the metaphase plate while all the other chromosomes segregate to the spindle poles in anaphase. The final part of this dissertation (Chapter 4) investigates the behavior of these LCs at the next mitosis.

## **1.2. Mitotic chromosome segregation**

Cells reproduce through a series of ordered events named cell cycle. Chromosomes are duplicated in S phase and distributed to two daughter cells during M phase. Between M and S phase and S and the subsequent M phase there are two gap (or growth) phases: G1 and G2 (Figure 1.1). The M phase of the cell cycle includes two major events: nuclear division (mitosis) and cytoplasmic division (cytokinesis) (Morgan, 2007). Mitosis is further divided into five stages: prophase, prometaphase, metaphase, anaphase, and telophase.

At prophase, replicated chromatin condenses into visible individual chromosomes in the intact nucleus. In the cytoplasm, duplicated centrosomes start moving apart. At prometaphase, the nuclear envelope (NE) breaks down, giving the chromosomes the chance to interact with microtubules (MTs) growing from the separated centrosomes. At metaphase, chromosomes align at the spindle equator to form what is known as the metaphase plate, and exhibit oscillatory movements. At anaphase, cohesion between sister chromatids is destroyed. The sister chromatids (now named chromosomes) are separated to two opposite poles of the spindle. At telophase, the chromosomes arrive at the spindle poles

and decondense. New NE assemblies around the chromosomes to pack the two sets of chromosomes into two new daughter nuclei. The assembly of contractile ring initiates during anaphase or telophase. During cytokinesis, the contractile ring pinches the cell between the two new nuclei and the cytoplasm divides into two individual daughter cells (El-Alfy et al., 1994; Roos, 1973a; Roos, 1976; Roos, 1973b).

### **1.3. The mitotic apparatus**

#### **1.3.1. The mitotic spindle**

Chromosome segregation is carried out by a bipolar array of MTs named the mitotic spindle. MTs and associated proteins generate the forces that move the chromosomes during mitosis and ensure that they are correctly distributed to the two daughter cells.

In mitotic vertebrate cells, MTs radiate from two MT Organizing Centers (MTOCs), the centrosomes (Rieder et al., 2001). Each centrosome consists of a pair of centrioles surrounded by pericentriolar material, including  $\gamma$ -tubulin ring complexes ( $\gamma$ -TuRCs) (Figure 1.2A). Using  $\gamma$ -TuRCs as templates, MT nucleation begins. The basic building blocks of MTs,  $\alpha/\beta$ -tubulin dimers, add onto  $\gamma$ -TuRCs templates head-to-tail to build 13 protofilaments that align side by side to form the wall of a hollow cylinder, the MT (Figure 1.2B). The head-to-tail orientation of tubulin dimers confers structural (and functional) polarity to MTs, whose plus ends always point away from the centrosomes (Figure 1.2B). Individual MTs undergo alternating phases of elongation and rapid shortening in a process named dynamic instability (Mitchison and Kirschner, 1984; Walker et al., 1988).

Many MT functions rely on their association with motor proteins (Sharp et al., 2000; Walker and Sheetz, 1993), which therefore represent important components of the mitotic spindle. MT-associated motor proteins can walk along MTs using the energy derived from ATP hydrolysis. MT-associated motor proteins fall into two major groups: dynein, which moves toward the MT minus end, and kinesin, most of which walks toward the plus end. Based on their functions in mitosis, the motors important for mitotic spindle assembly can be sorted into three groups, as described in Table 1.1.

Beside MTs and MT associated proteins, a structural scaffold, which may tether spindle-assembly factors (SAFs) and support spindle assembly and force generation, was proposed in 1969 (McIntosh et al., 1969) and later named spindle matrix. Although the function or even the existence of the spindle matrix is still debated, recent studies have identified some candidate components of such a scaffold, namely Skeletor, Chromator, Megator and EAST (Qi et al., 2005; Qi et al., 2004; Rath et al., 2004; Walker et al., 2000). In addition, Lamin B was identified as a component of a membranous spindle matrix, Fin1p (and Ase1p) was found in the midzone matrix, and NuMA in the pericentriolar matrix (Gatlin et al., 2010; Kristen M Johansen, 2007; Tsai et al., 2006; Zheng and Tsai, 2006).

### **1.3.2. Mitotic chromosomes**

Upon mitotic entry, each chromosome is composed of two sister chromatids, which undergo coordinated condensation. Compared with interphase chromosomes, mitotic chromosomes condense about ten-fold in mammalian cells, and two-fold in yeast (Koshland and Strunnikov, 1996). Due to chromosome condensation, chromosomes become visible as rod-

like structures (about 0.7  $\mu\text{m}$  thick) in prometaphase-metaphase mammalian cells (El-Alfy et al., 1994). Condensation not only eliminates the tangle between sister chromatids and nonhomologous chromatids, but also limits the space occupied by each chromatid, thus preventing any part of a long chromatid thread from being trapped in the cleavage furrow (Koshland and Strunnikov, 1996). Mitotic chromosome condensation is achieved thanks to the action of specialized chromosome-associated proteins named condensins (Hirano et al., 1997). Interestingly, the condensed chromosome structure is required for both correct spindle assembly and accurate chromosome segregation (Wignall et al., 2003). Indeed, chromosome condensation defect mutants (e.g., condensin mutants) frequently exhibit lagging chromosomes (LC) and chromatin bridges in anaphase, which result in chromosome segregation failure (Hirota et al., 2004).

The two sister chromatids are held together by cohesin and cohesin-associated proteins (chromosome cohesion) until the onset of chromosome segregation (Nasmyth and Haering, 2009; Onn et al., 2008). Cohesin complexes are loaded onto the chromatin in telophase in vertebrate cells, and in G1 phase in yeast (D'Ambrosio et al., 2008; Lengronne et al., 2004; Xiong and Gerton, 2010), and cohesion between sister chromatids is established during DNA replication (Lengronne et al., 2006; Skibbens, 2009). At the onset of chromosome segregation in anaphase, a protease, separase, cleaves cohesin complex subunits, thus triggering sister chromatid separation (Xiong and Gerton, 2010).

Mammalian chromosomes are associated with a large number of proteins, many of which constitute the Chromosome Periphery, a distinct surface protein layer found along the chromosome arms, except for the nucleolus organizer regions and the KT-

occupied centromeric region (Figure 1.3). Although the function for many of chromosome-associated proteins is still unclear, at least 102 of them have been identified in human cells (Takata et al., 2007). Of these, more than 80 are localized at the centromere-KT region (Cheeseman and Desai, 2008).

### 1.3.3. Centromere and KT

The centromere, which appears as a constriction in the metaphase chromosome, is the region of chromosomal DNA that directs KT assembly. The KT is a large protein complex that assembles on the centromere and is the major site of chromosome/spindle interaction (Figure 1.4). Up to 20-25 MTs attach to a vertebrate KT (McEwen et al., 1997) (Figure 1.4B), whereas a budding yeast KT binds only one MT (Peterson and Ris, 1976). By electron microscopy (EM), KTs in lower plants and most animals have a trilaminar plate morphology, with about 15-60 nm-thick dense inner and outer KT plates and a 20-30 nm electron lucent middle KT gap layer (Figure 1.4A) (Santaguida and Musacchio, 2009; Sumner, 2003). A ~100-200 nm fibrous corona extends outward from the outer KT plate, while the inner KT plate sits on the inner centromere/chromatin region (Figure 1.4A,C).

The KT assembles at the centromeric region of the chromosome (Figure 1.4C), which contains a cluster of nucleosomes assembled with CENP-A, a histone H3 variant. CENP-A nucleosomes recruit the constitutive centromere-associated network (CCAN) to form the inner KT (Cheeseman and Desai, 2008; Foltz et al., 2006; Palmer et al., 1991; Wan et al., 2009). The outer KT, which assembles at prophase and disassembles at the end of mitosis, provides the attachment sites for kMTs. The core of each attachment site is composed of three complexes: hKnl1/Blinkin complex, Mis12 complex, and Ndc80 complex

(Cheeseman et al., 2006), which together constitute the KMN network. The outermost layer of KT proteins constitutes what appears as the fibrous corona by EM. This layer includes proteins with very different functions, including spindle assembly checkpoint signaling (e.g., Mad1, Mad2, Bub1, Bub3, Cdc20, dynein, RZZ complex), motor proteins (e.g., CENP-E, dynein), and MT dynamic regulators (e.g., CLASP, EB1, CLiP170) (Figure 1.4 C).

## **1.4. The dynamics of mitosis**

### **1.4.1. Mitotic spindle assembly mechanisms**

Distribution of the two sister chromatids to the two daughter cells relies on forces that move the chromosomes apart upon sister chromatid separation. One major source of force production is the pulling occurring at the sites of KT-MT interactions. The direction of this force is toward the spindle pole to which the KT is connected. To move in opposite directions and to be deposited into different daughter cells, the two sister KTs need to be linked via MTs to opposite spindle poles of the mitotic spindle.

Mitotic spindle assembly can occur through three possible mechanisms already noted by Schrader in 1944 (Schrader, 1944): (1) MTs from the spindle poles “search-and capture” the KTs; (2) KTs drive MT “self-assembly” into a spindle; and (3) Cooperation between the above two mechanisms (Rieder, 2005). In the firmly established “search-and-capture” model (Kirschner M, 1986), MTs from the spindle poles frequently switch between shrinkage and growth to search KTs. During this dynamic “searching”, MTs from the spindle poles encounter KTs and capture them (Hayden et al., 1990; Tanaka and Desai,

2008). The MT becomes attached end-on to the KT, thus becoming a kMT (Rieder and Alexander, 1990). As more and more kMTs connect the KT to the same spindle pole, they form a bundle, named KT fiber (k-fiber) (McEwen et al., 1997). The attachment of the sister KT to a k-fiber from the opposite pole completes the formation of correct KT-MT attachment in the search-and capture model. The self-assembly of the mitotic spindle is typical of acentrosomal cells (Khodjakov et al., 2000; Wadsworth and Khodjakov, 2004). However, recent studies have shown that it can also occur in the presence of centrosomes in various organisms, including mammals (Khodjakov et al., 2000; Khodjakov et al., 2003; Maiato et al., 2004b). Cooperation of these two mechanisms may explain how k-fibers can form so quickly and so accurately (Mogilner et al., 2006; O'Connell and Khodjakov, 2007; Paul et al., 2009).

#### **1.4.2. KT-MT attachment and the spindle assembly checkpoint**

During this complex KT-MT attachment formation process, there are chances that incorrect attachments form. The correct attachment, named amphitelic attachment, requires that the two sister KTs attach to k-fiber from opposite spindle poles (Figure 1.5 A). Amphitelic attachment ensures that pulling forces applied to the two sister chromatids are in opposite directions. During the process of establishing amphitelic attachment, there is typically a short-lived attachment type, the monotelic attachment, in which only one of the sister KT is attached to MTs, whereas the other one is unoccupied (Figure 1.5 B) (Rieder and Salmon, 1998). Monotelic attachment typically converts to amphitelic attachment before anaphase onset. Two types of incorrect attachments that can occur during mitosis are: syntelic attachment, in which the sister KTs attach to two k-fiber from the same spindle pole (Figure

1.5 C); merotelic attachment, in which a single KT binds MTs from opposite spindle poles (Figure 1.5 D) (Cimini, 2008; Cimini and Degross, 2005; Salmon et al., 2005), while typically the sister is correctly attached to just one pole. Because chromosomes with monotelic or syntelic attachment are linked to only one of the spindle poles, they are called mono-oriented chromosomes. If those attachments persisted beyond anaphase onset, they would cause chromosome mis-segregation (Figure 1.5 B-C). However, monotelic attachments are usually transient (Rieder and Salmon, 1998) and syntelic attachments are rarely observed in metaphase cultured cells (Hauf et al., 2003). Existence of even a single monotelic chromosome makes the cell delay anaphase onset (Rieder et al., 1994). However, cells possessing merotelic KT attachment show no delay in anaphase onset (Cimini et al., 2004; Khodjakov et al., 1997). Merotelically attached chromatids can become anaphase LCs, which can cause chromosome mis-segregation and aneuploidy (Cimini et al., 2004; Cimini et al., 2001).

Because KT misattachments often occur in prometaphase, detection and correction of misattachments are needed. The mitotic protein kinase aurora B is thought to be responsible for both syntelic and merotelic correction (Cimini, 2007; Cimini et al., 2006; Ditchfield et al., 2003; Hauf et al., 2003; Knowlton et al., 2006). Aurora B can phosphorylate Hec1 in the Ndc80 complex (Cheeseman et al., 2006; DeLuca et al., 2006), this phosphorylation inhibits the MT-binding ability of the Ndc80 complex in vitro (Cheeseman et al., 2006), and inhibition of Ndc80 phosphorylation results in hyperstable merotelic attachments and chromosome mis-segregation (DeLuca et al., 2006). Interestingly, aurora B is enriched at the centromere of merotelically attached chromosomes (Knowlton et al., 2006), which is believed to favor detachment of MTs from merotelic KTs (Cimini, 2007). MCAK, another

substrate of Aurora B, was also found to regulate misattachment correction and MT dynamics at KT (Andrews et al., 2004; Kline-Smith et al., 2004; Lan et al., 2004; Ohi et al., 2004).

The spindle-assembly checkpoint (SAC) is the biochemical signaling pathway that prevents separation of sister chromatids until all the KTs have established attachment to MTs. The first group of core components of the SAC was identified in 1991 in budding yeast (Hoyt et al., 1991; Li and Murray, 1991). This included the MAD1-3 (*mitotic-arrest deficient*), BUB1, BUB3 (*budding uninhibited by benzimidazol*), and MPS1 (*monopolar spindle*) proteins (Hoyt et al., 1991; Li and Murray, 1991). Although these proteins remain the key components of the SAC, many other proteins are now known to be involved in SAC signaling (Table 2).

When a cell enters mitosis, the SAC signal is active (“on”). A “waiting” signal is generated at the unattached KTs (Rieder et al., 1995) (Figure 1.6) and leads to the formation of the mitotic checkpoint complex (MCC, containing MAD2, BUBR1/Mad3, BUB3) (Morrow et al., 2005), which negatively regulates CDC20, a cofactor of the APC (anaphase-promoting complex), thus inhibiting the E3 ubiquitin ligase activity of APC, and preventing progression into anaphase (Fang et al., 1998). When all the KTs have become attached to MTs, the SAC is satisfied (turned “off”) (Figure 1.6) and the MCC disassembles. This will release Cdc20, which will thus activate the APC and lead to the polyubiquitination of securin and cyclin B. The destruction of securin by the proteasome releases the protease separase, which cleaves the cohesin complex, thus leading to sister chromatid separation. The destruction of cyclin B inactivates CyclinB-CDK1 (Cyclin-dependent kinase-1) activity, which promotes mitotic exit (Peters, 2006).

### 1.4.3. Metaphase, chromosome oscillations, and microtubule dynamics

As chromosomes become attached to spindle MTs, they align at the spindle equator to form a structure called the metaphase plate. Although collectively the chromosomes maintain a relatively stable position at the metaphase plate, in many different cell types, metaphase chromosomes are not static. Instead, metaphase chromosomes oscillate back and forth about the spindle equator, a phenomenon named directional instability (Skibbens et al., 1993). Despite being very common, directional instability is not universal. Indeed, some cell types, including most animal tissue culture cells, fission and budding yeast, display chromosome oscillations about the metaphase plate (Funabiki et al., 1993; Magidson et al., 2011; Pearson et al., 2001; Salic et al., 2004; Skibbens et al., 1993), whereas in other systems, such as *Xenopus* egg extracts, *Drosophila* embryos, *Drosophila* S2 cells, insect spermatocytes, oocytes, and higher plant cells, metaphase chromosomes do not undergo directional instability (Brust-Mascher and Scholey, 2002; de Lartigue et al., 2011; Desai et al., 1998; LaFountain et al., 2001; Maddox et al., 2003). Moreover, one interesting example is represented by PtK1 cells, in which oscillation behavior varies depending on location of the chromosome along the metaphase plate (Cameron et al., 2006; Cimini et al., 2004; Wan et al., 2012). This provides a good system to study the distribution of forces within an individual cell. Finally, even for individual chromosomes, the oscillation pattern can vary over time, switching between regular oscillations and irregular movements (Magidson et al., 2011). Because directional instability of KT motility is characterized by such high variability, a quantitative characterization of such behavior is the first step to understand the underlying mechanisms and how they contribute to the behavior of the overall system.

Chromosome oscillation has been dissected into three coupled oscillations (Wan et al., 2012). The most noticeable one is the oscillation of centromere location. This is easily visible when tracking a chromosome relative to the metaphase plate. The second oscillation, closely coupled to the first one, is the oscillation in length of each K-fiber. This is the result of switches between polymerization and depolymerization of MT plus ends (at the KT-MT interface). The third type of coupled oscillation is the distance between the two sister KTs on each chromosome. Changes in this distance result from the interplay between forces imparted by the spindle and forces generated as a result of the mechanical response of the centromere to chromosome oscillations (Dumont et al., 2012). The coupling of these different types of oscillations reflects the interplay between distribution of forces within the mitotic cell and mechanical properties of the mitotic apparatus.

Although the function of these chromosome oscillations is not clear, quantification and modeling of metaphase chromosome dynamics can provide a framework that will enable quantitative understanding of how spindle dynamics ensure establishment of KT attachment and correction of misattachments. Building such a quantitative model and using it to dissect the oscillatory behavior of normal and mis-attached chromosomes was the focus of the first part of this work and is described in Chapters 2 and 3.

#### **1.4.4. Anaphase chromosome segregation**

After the SAC is satisfied, anaphase begins with the separation of sister chromatids.

Anaphase chromosome segregation occurs thanks to two distinct mechanisms: anaphase A,

in which sister chromatids separate by being pulled to opposite poles of the spindle, and Anaphase B, in which the spindle poles themselves move apart further increasing the distance between the two sets of chromosomes (Brust-Mascher and Scholey, 2002) (Figure 1.6).

Two types of forces generated by MT dynamics are generally believed to play a key role in promoting chromosome separation and poleward chromosome movement in anaphase A (Maiato and Lince-Faria, 2010). The first is a KT generated poleward force: disassembly of MT plus-ends at the KT occurs without loss of KT-MT attachment; this is thought to produce force to pull the chromosomes poleward (Grishchuk et al., 2005; Inoue and Salmon, 1995; McIntosh et al., 2008). The second source of force is generated by MT poleward flux: disassembly of MT minus ends at the spindle poles pulls the kMTs themselves toward the pole (Forer, 1965; Mitchison, 1989). Other poleward-force-generation models have also been proposed and emphasize the role of KT motors, actin/myosin, spindle matrix, or coupled sliding between k-fibers and interpolar MTs (Figure 1.1) (Cheeseman and Desai, 2008; Maiato and Lince-Faria, 2010).

Spindle elongation in anaphase B may be driven by forces that are intrinsic to the spindle and/or outside the spindle. Intrinsic force in the spindle is the pushing force generated by the sliding of interpolar MTs (Figure 1.1), initially proposed by McIntosh and colleagues (McIntosh et al., 1969). Bipolar kinesins, such as KLP61F (*Drosophila*) or Eg5 (human) are thought to drive spindle elongation in anaphase B through this mechanism (Sharp et al., 2000). Force outside the spindle is generated by cortex-mediated pulling forces on astral MTs, first proposed by Boveri (Boveri, 1888). This hypothesis got support by microsurgery experiments using a microneedle or

microbeam. Aster MT destruction slowed down or halted spindle elongation, while cutting the spindle midzone (the region between the two sets of chromosomes) accelerated this movement in vertebrate cells (Aist et al., 1993; Kronebusch and Borisy, 1982). Cytoplasmic dynein located at the cell cortex interacts with astral MTs to provide pulling force, while the spindle midzone MTs work with kinesin 5 (Eg5) to slowdown spindle pole separation (Civelekoglu-Scholey and Scholey, 2007; Saunders et al., 2007; Sharp et al., 2000). The balance between these two mechanisms determines the rate of spindle elongation.

#### **1.4.5. Telophase: completion of mitosis**

Telophase is the last phase of nuclear division. The two major events in telophase are spindle disassembly and the formation of new NE.

The mitotic spindle disassembles after completion of chromosome segregation. The KTs are detached from MTs and the central spindle, an array of antiparallel MTs with a dense protein matrix at its center, emerges between the two sets of chromosomes. The central spindle, in combination with a centrosome-dependent pathway in some organisms and/or cell types, defines the position of the cleavage furrow (Dechant and Glotzer, 2003; Shuster and Burgess, 1999; Wheatley and Wang, 1996). Central spindle associated proteins, such as Aurora B, are required for stimulation of cleavage (Canman et al., 2003; Goto et al., 2003) (Described in section 5.4 Cytokinesis).

New NEs form around each set of decondensing chromosomes in telophase. Two different models have been proposed to explain how a NE is assembled around the newly segregated

chromosomes. The first “vesicle fusion model” is based on the evidence that in cell-free systems nuclei can form in a test tube by mixing a chromatin source, cytosol and fragmented membranes (Newport, 1987). The second model, the “reshaping ER model” (Anderson and Hetzer, 2008b), is based on the evidence that both *in vitro* and in intact cells preformed ER can rapidly reshape to coat the chromatin, thus forming new NE (Anderson and Hetzer, 2007; Anderson and Hetzer, 2008a; Anderson and Hetzer, 2008b; Anderson et al., 2009). Decondensed chromatin is required to interact with DNA-binding-NE-specific membrane proteins to initiate the NE formation process (Anderson and Hetzer, 2007; Hetzer, 2010; Ramadan et al., 2007). A chromosome (or fragment of chromosome) that failed to move together with the majority of chromosomes (i.e., a LC), may be enclosed by its own NE and give rise to a micronucleus (MN). Part of this work was aimed at understanding the fate of the LC after enclosure into a MN. Investigating the behavior of chromosomes enclosed in micronuclei (MNi) is very important for a better understanding of the long-term impact of chromosome segregation errors.

#### **1.4.6. Cytokinesis**

When the nuclear division is about to end, cytokinesis begins. Through cytokinesis the two newly formed nuclei and cytoplasmic components (e.g., organelles) are separated into two daughter cells. Cytokinesis is comprised of a series of sub-processes and substructures (Figure 1.7).

First, the cleavage site is determined by the spindle positioning at anaphase. At the cleavage site, the motor protein myosin II, a ring of actin filaments, and many other proteins attach to the plasma membrane to form a contractile ring. Myosin II produces the force to constrict

the contractile ring by sliding overlapping actin filaments, which results in the formation of the cleavage furrow in the plasma membrane (Pollard, 2010; Pollard and Wu, 2010). In early telophase, the cleavage furrow ingresses. MTs contact the cortex and rearrange to create a region, the midzone or the central spindle, consisting of bundled MTs (Eggert et al., 2006). The intercellular bridge, which is a MT-rich structure connecting the two daughter cells prior to abscission, forms in late telophase. At the center of the intercellular bridge is the midbody, composed of a disk (the stembody) with high protein density and MTs. When the intercellular bridge is resolved the cell is abscised into two daughter cells. Typically, abscission is delayed for the clearance of chromatin in the cleavage site in case of chromosome bridges.

## **1.5. Causes of chromosome mis-segregation**

Many pathways have been proposed to lead to aneuploidy (Rajagopalan and Lengauer, 2004) (Figure 1.8), although it is still unclear how aneuploidy originates in the human body. Some studies showed that aneuploidy may be a result of mutations in genes involved in the process of cell division. However, because mitosis is so complex and the cell may fail to perfectly regulate it, aneuploidy may also arise in “non-mutated” cells.

### **1.5.1. Spindle assembly checkpoint defects**

The spindle assembly checkpoint (SAC), also known as the mitotic checkpoint (described in 4.2 and Figure 1.6), prevents sister chromatid separation if chromosomes are not fully

attached to MTs. Even a single monotelic chromosome delays anaphase onset in normal mammalian cells (Rieder et al., 1994).

There are three ways in which SAC defects may lead to aneuploidy: (1) SAC inactivation; (2) Weakened SAC; (3) Persistent SAC activation.

Complete inactivation of the mitotic checkpoint causes massive chromosome mis-segregation and is lethal to both normal somatic cells and cancer cells (Kops et al., 2004; Lee et al., 2004). Similarly, germ line mutations of checkpoint components cause high frequency of aneuploidy, which is typically embryonic lethal, as shown in studies with Mad2 or Bub3 knockout mice (Dobles et al., 2000; Kalitsis et al., 2000). Moreover, reducing the levels of the checkpoint proteins BubR1 or Mad2 in human cancer cells provokes apoptosis within six divisions (Kops et al., 2004). So, inactivation of the SAC is unlikely to be a major mechanism of origin of long-lived aneuploid progeny, as it typically results cell death. This may explain why SAC signaling failure is rarely found in extensive studies of aneuploid human tumors (Schvartzman et al., 2010).

However, if the SAC signaling pathway is only weakened, cells may be able to align most of their chromosomes prior to anaphase onset and enter anaphase and separate the sister chromatids when only a small number (1-few) of KTs is still unattached, which may result in degrees of aneuploidy compatible with life. This idea is supported by numerous studies in mice with haploinsufficiency for individual SAC proteins showing increased rates of cancer at various anatomical sites (Babu et al., 2003; Dai et al., 2004; Michel et al., 2001; Weaver et al., 2007). Furthermore, weak BUBR1 mutations were identified in patients

with mosaic variegated aneuploidy (MVA) disorder, in which >25% somatic cells are aneuploid and with various karyotypes (Hanks et al., 2004).

Persistent activation of the SAC (e.g., in the absence of a spindle, Figure 1.9) prolongs mitosis in cultured animal cells, but the delay is often transient (Figure 1.9). Exit from mitosis without satisfying the SAC is termed checkpoint “adaptation”, “slippage”, or “leakage” (Rieder and Maiato, 2004), and yields a tetraploid cell, which may produce aneuploid cells in later generations.

### **1.5.2. Cohesion defects**

Cohesin complexes between sister chromatids need to be destroyed exactly at the time of anaphase onset. Premature or delayed separation of sister chromatids can both cause chromosome mis-segregation and mutations in cohesion related genes may promote aneuploidy. When searching for candidate genes that may lead to aneuploidy in colorectal cancers, 10 of 11 mutations identified were in genes that directly contribute to sister chromatid cohesion (Barber et al., 2008). Furthermore, overexpression of cohesion regulators (separase or securin) promotes aneuploidy (Yu et al., 2003; Zhang et al., 2008).

### **1.5.3. Merotelic KT attachment**

Merotelic KT attachment (a single KT bound to MTs from opposite spindle poles) is not detected by the SAC, so a cell with merotelic attachments can enter anaphase and segregate its chromosomes. The merotelically attached chromatid, however, will be pulled toward both poles, and in some cases it will lag behind at the spindle equator (anaphase LC) (Cimini et al., 2001). The chromosome lagging at the spindle equator has the potential to be

included into the same daughter cell as its former sister chromatid, which will result in the production of two aneuploid daughter cells. LCs occur in 1-2% of mitotic tissue culture cells (Cimini et al., 2001), are the most common chromosome segregation defect found in cancer cells (Ganem et al., 2009; Silkworth et al., 2009; Thompson and Compton, 2008), and are observed in 4.6% of mitotic neural progenitor cells in sections of mouse embryonic cerebral cortices (Yang et al., 2003). Upon mitotic exit, LCs are included in micronuclei (MNi) (Cimini et al., 2002), small nuclei separate from the main nucleus. Understanding the mitotic behavior of such micronuclear chromosomes at the following mitosis is the focus of Chapter 4.

#### **1.5.4. Multipolar mitotic spindles and centrosome abnormalities**

Cells with more than two centrosomes (supernumerary centrosomes) can assemble multipolar mitotic spindles, which can in turn lead to aneuploidy (Pihan and Doxsey, 1999; Zhou et al., 1998). Extra centrosomes are frequently observed in human cancer cells (Brinkley, 2001; Nigg, 2006) and can originate from centrosome amplification or from the same processes that generate tetraploid cells (e.g., cell fusion, cytokinesis failure, mitotic slippage, or endoreduplication) (Holland and Cleveland, 2009). Interestingly, immunofluorescent detection of uncultured cells in normal mouse cerebral cortex revealed that 3.2% of mitotic neural progenitor cells harbored supernumerary centrosomes (Yang et al., 2003). This means that non-mutated mammals may face the risk of having a multipolar spindle in live tissues.

Multipolar spindles may lead to multipolar division, which tends to produce “highly” aneuploid cells, which are often inviable (Ganem et al., 2009) (Figure 1.4 D). This prevents multiplication of the highly aneuploid cells. To avoid multipolar division, multiple centrosomes can cluster into two spindle poles, a phenomenon frequently observed in cancer cells (Brinkley, 2001; Ganem et al., 2009; Quintyne et al., 2005; Silkworth et al., 2009). The limitation of this clustering process is that it leaves behind high frequencies of merotelic attachments, which then lead to chromosome mis-segregation (Ganem et al., 2009; Silkworth et al., 2009) (Figure 1.4 D).

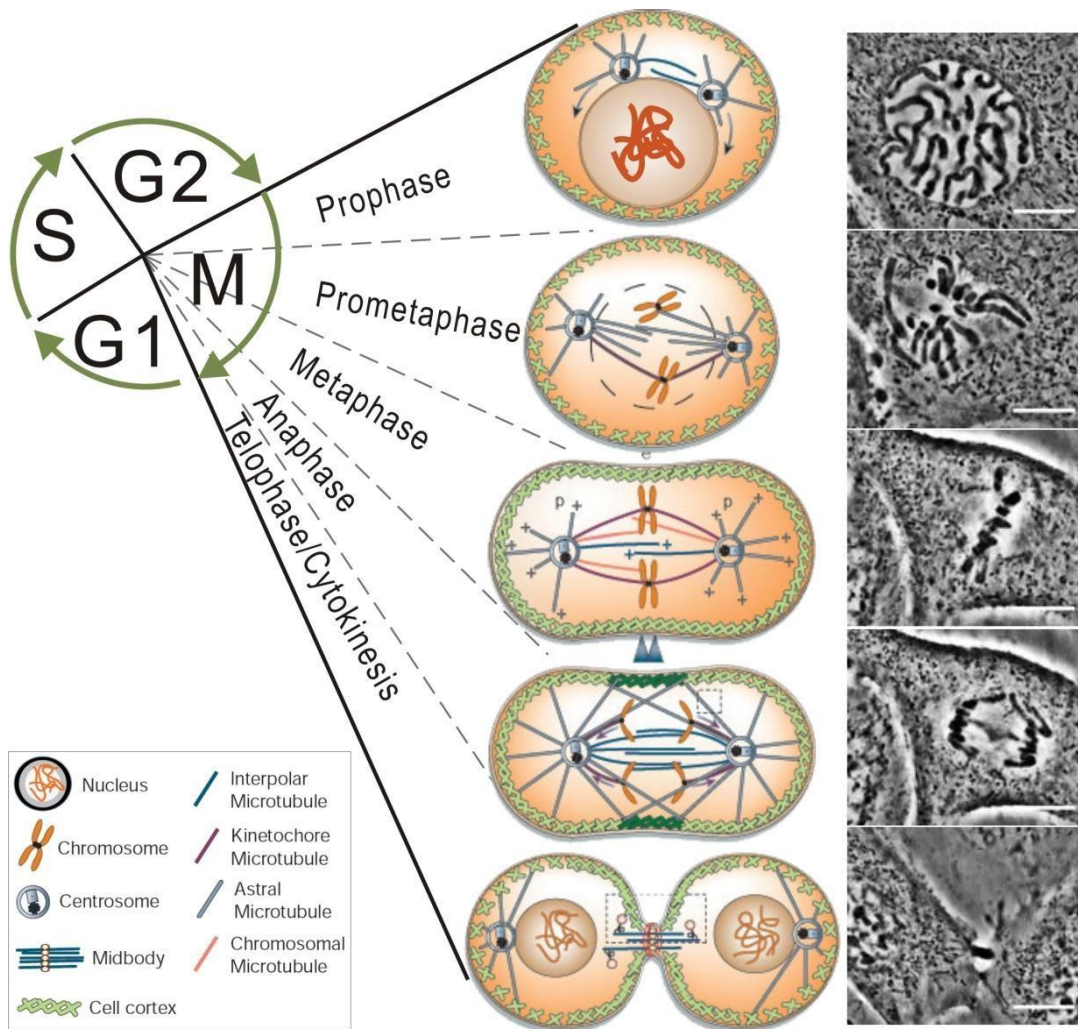
#### **1.5.5. Defective correction of KT-MT mis-attachments**

As described in section 5.3, merotelic KT attachment is a common cause of aneuploidy in normal and cancer cells. Merotelic KT attachments form spontaneously at relatively high rates in early prometaphase, but most of them are corrected prior to anaphase onset (Cimini et al., 2003).

As described in section 4.2, Aurora B-dependent phosphorylation of the Ndc80 complex directly controls the stability of KT-MT attachment and correction of erroneous attachments (Cimini et al., 2006; DeLuca et al., 2006). This results in turnover of kMTs, so that incorrectly attached MTs can detach from the KT and new MTs can bind (Cimini et al., 2006; DeLuca et al., 2006). Recent studies have shown that the dynamics of kMTs must be finely tuned to ensure that KT-MT attachments are stable enough for SAC silencing and mitotic progression, but unstable enough to ensure correction of mis-attachments (Bakhoun et al., 2009b). Key players in ensuring accurate control of MT dynamics are the kinesin-13 family proteins Kif2a, Kif2b, and MCAK (Kif2c). For instance, the MT depolymerases

MCAK and Kif2b temporally control kMT dynamics and their depletion result in increased rates of anaphase lagging chromosomes (Bakhoun et al., 2009b). Importantly, a number of cancer cell types, which display high rates of anaphase lagging chromosomes, also display altered kMT dynamics (Bakhoun et al., 2009a) and overexpression of the appropriate kinesin 13 can both re-establish normal kMT dynamics and reduce the number of anaphase lagging chromosomes (Bakhoun et al., 2009b). Finally, co-depletion of Kif2a and MCAK results in reduced MT poleward flux and increased rates of anaphase lagging chromosomes (Ganem et al., 2005), suggesting that poleward flux is important for correction of mis-attachments. However, it is not clear how, mechanistically, poleward flux contributes to correction of KT mis-attachments and it is unclear how different aspects of MT dynamics are coordinated to collectively contribute to correction of mis-attachments.

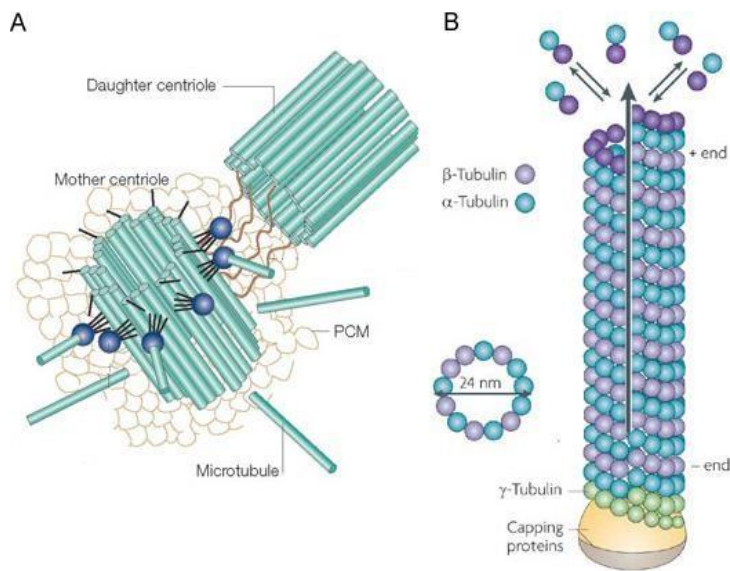
To address this question, we made use of a mathematical model developed in Chapter 2 and integrated experimental approaches and computational modeling and simulation to investigate how modifying certain aspects of MT dynamics affects correction of KT mis-attachments and accuracy of chromosome segregation. This work is described in Chapter 3.



**Figure 1.1. Overview of mitosis**

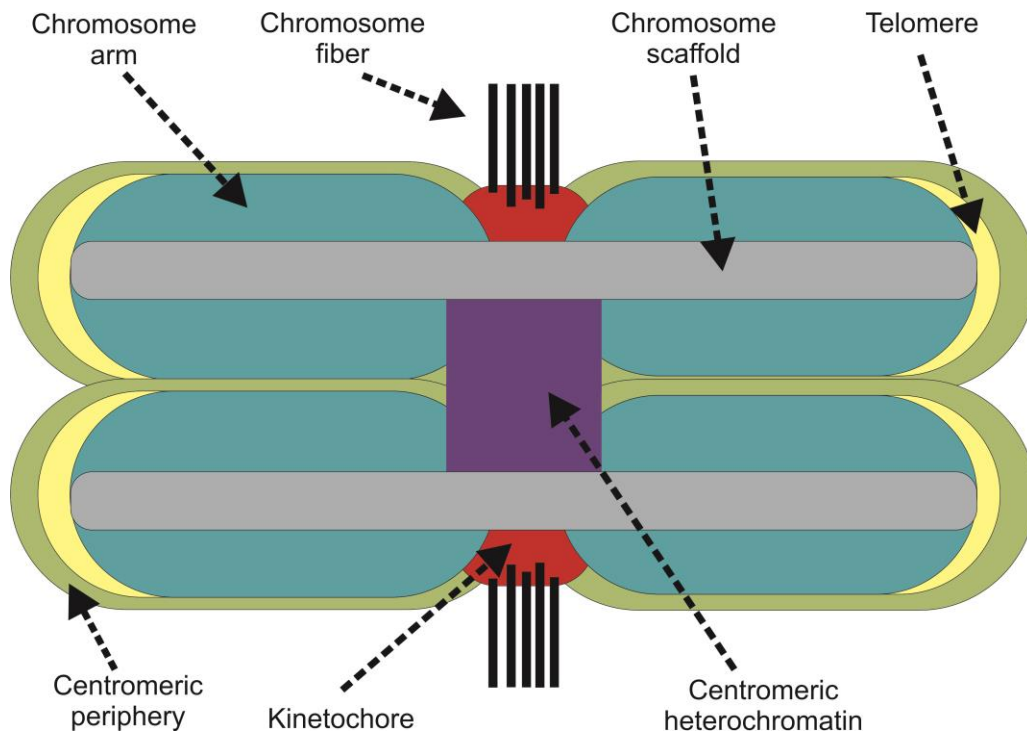
The M phase of the cell cycle is subdivided into several sequential phases. In prophase, chromosomes condense. Centrosomes migrate apart around the nucleus and spindle assembly begins. In prometaphase, the NE breaks down. Chromosomes attach to MTs and congress toward the spindle equator. In metaphase, sister chromatids are attached to opposite spindle poles. MTs are organized into four sets: astral MTs, which link spindle poles to the cell cortex; chromosomal MTs, which link chromosome arms to the poles; KT MTs (kMTs), which link the poles to KTs; and interpolar MTs (ipMTs), which link the two poles. In anaphase, the sister chromatids separate and move toward opposite poles (segregation). In telophase, the chromosomes decondense and the NE re-forms around the two groups of segregated chromosomes. The contractile ring forms and

begins to contract during anaphase. In telophase, the contractile ring further contracts (furrow ingression) developing a barrier between the daughter cells and constricting the spindle mid-zone (the array of ipMTs lying between separated chromatids) to form a structure called the midbody (the remnant of the mid-zone). During cell abscission, the furrow 'seals' completely separating the daughter cells. The cartoon is adapted from (Scholey et al., 2003) with permission from Nature Publishing Group. Phase contrast micrographs in live PtK1 cells in the right panel are samples of the corresponding phases in the cartoon.



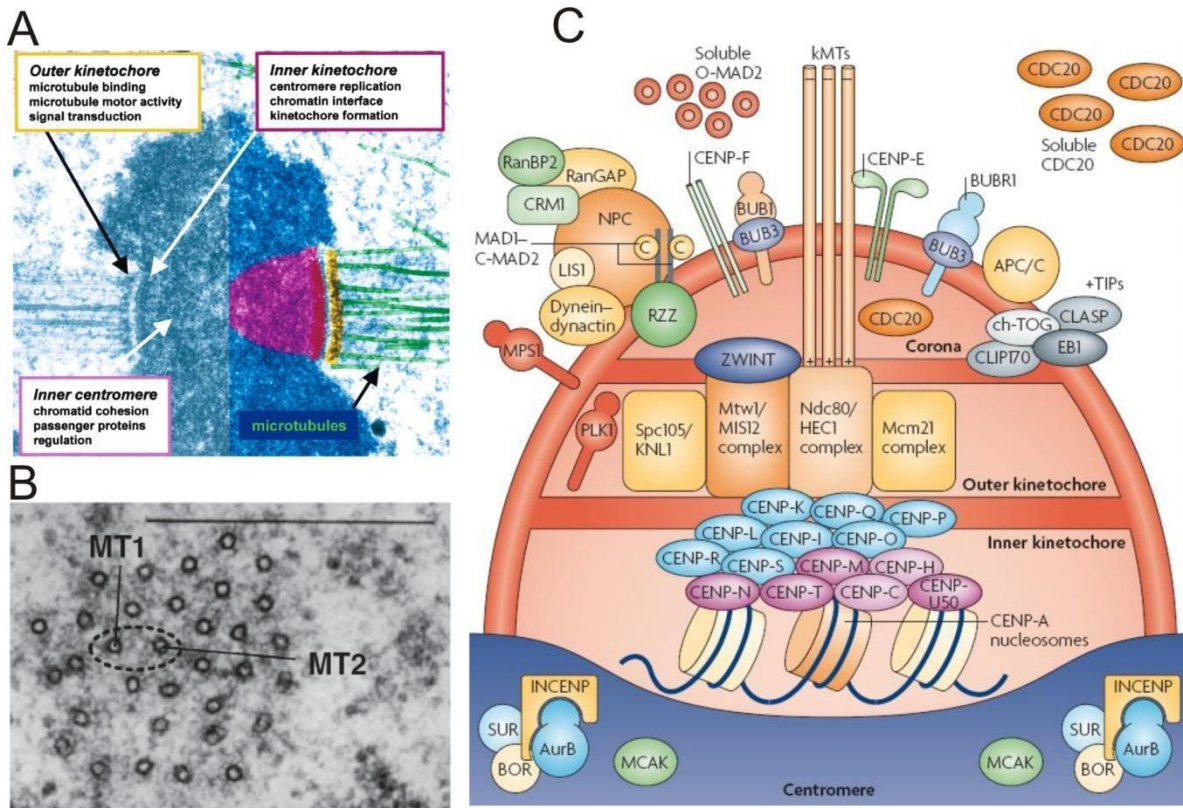
**Figure 1.2. Structure of centrosome and microtubule**

(A) A centrosome consists of two centrioles embedded in pericentriolar material (PCM). MTs nucleate on the template of  $\gamma$ tubulin ring complexes in the PCM. Figure adopted from (Sluder, 2005) with permission from Nature Publishing Group. (B)  $\alpha/\beta$ -tubulin dimers dynamically add to (or dissociate from) the plus end of a MT. Capping proteins regulate the stability of the MT minus end. The diameter of the 13 protofilament cylinder of a MT is 24nm. Figure adopted from (Conde and Caceres, 2009), 2009) with permission from Nature Publishing Group.



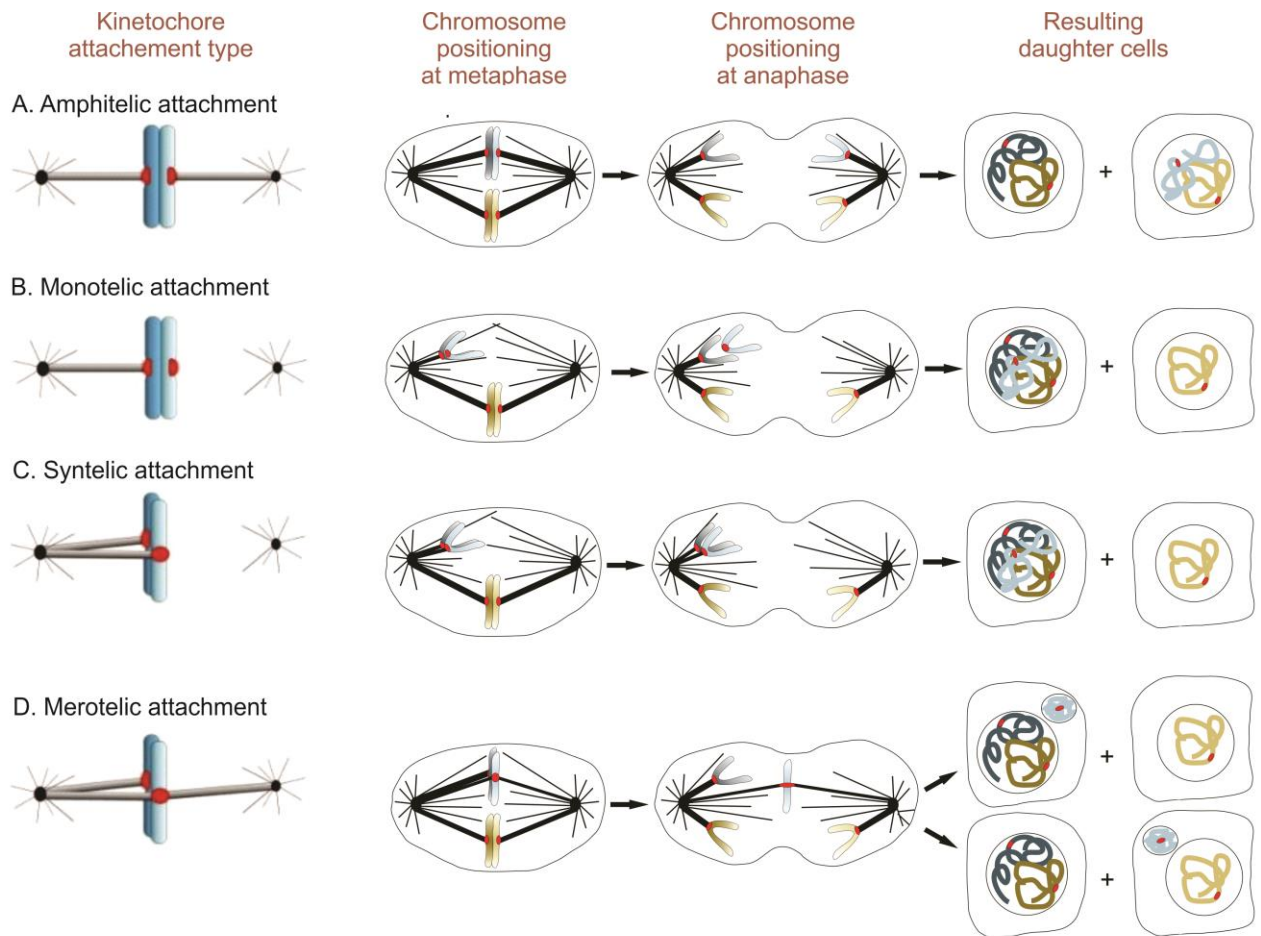
***Figure 1.3. Metaphase human chromosome Structure of metaphase human chromosome***

Illustration based on (Takata et al., 2007).



**Figure 1.4. KT structure**

(A) and (B) are electron micrographs. (A) Side view of a KT in the green algae *Oedogonium cardiacum* showing the typical trilaminar plate (Cleveland et al., 2003). (B) Transverse section through the k-fiber of a metaphase PtK1 cell, showing multiple MTs attached to the same KT. Bar=0.5  $\mu$ m (Santaguida and Musacchio, 2009) (with permission from John Wiley and Sons). (C) Diagrammatic representation of KT architecture and KT protein organization. Inner centromere region shown in blue (Musacchio and Salmon, 2007) (with permission from Nature Publishing Group).



**Figure 1.5. Chromosome segregation produced by different KT–MT attachments**

(A) Amphitelic attachment between KT's (red) and MT's (black or gray lines) leads to correct chromosome segregation. (B and C) Persistent monotelic or syntelic attachment in anaphase leads to chromosome mis-segregation and aneuploidy cell. (D) Persistent merotelic attachment can produce an anaphase lagging chromosome, which may be enclosed into a micronucleus in the daughter cell. Column 1 shows the different types of attachments. Columns 2-4 show the mitotic behavior of chromosomes with different types of attachments. From (Cimini, 2008) with permission from Elsevier.

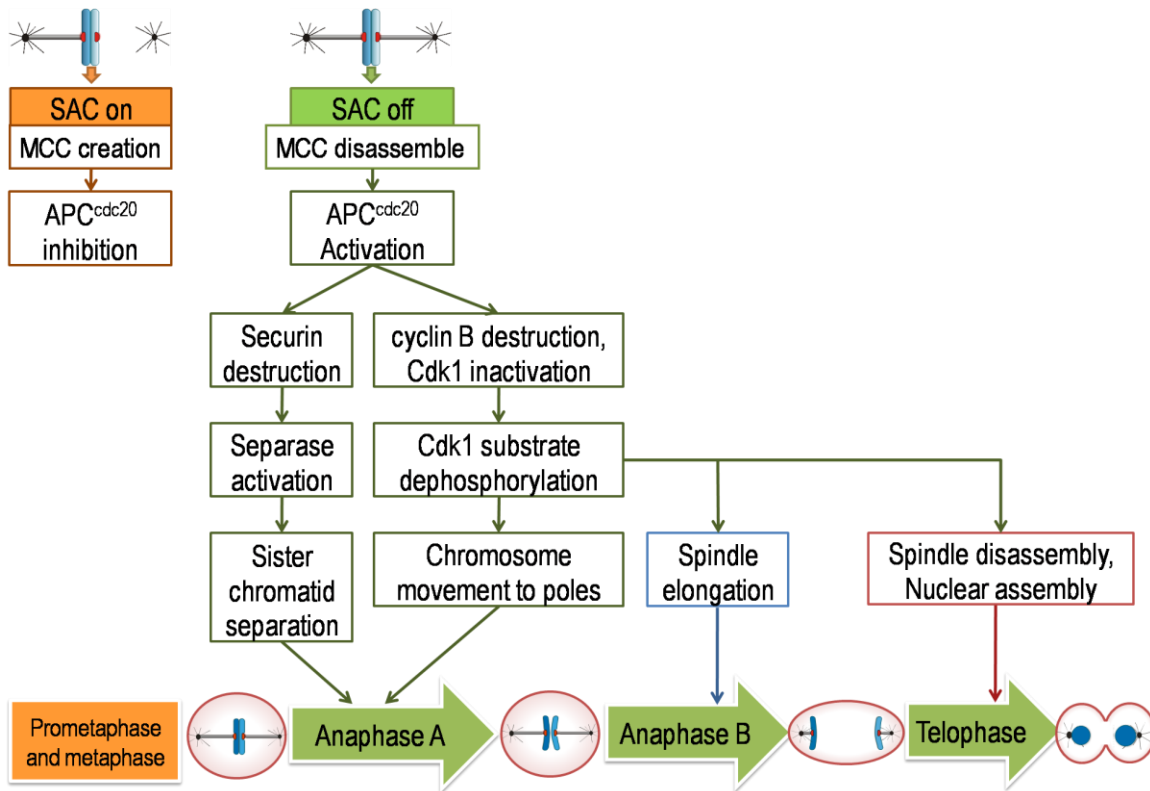


**Figure 1.6. Spindle assembly checkpoint (SAC) and completion of mitosis**

Before amphitelic KT attachments are formed, the SAC is on. MCC accumulates and binds CDC20. So, the E3 ubiquitin ligase activity of APC<sup>cdc20</sup> is inhibited. After all chromosomes are amphitelicly attached, the SAC is turned off. APC<sup>cdc20</sup> is activated and promotes chromatid separation and poleward movement. Downstream effects also include spindle elongation, spindle disassembly, nuclear assembly, and eventually the completion of mitosis. Figure based on (Musacchio and Salmon, 2007) and (Morgan, 2007).

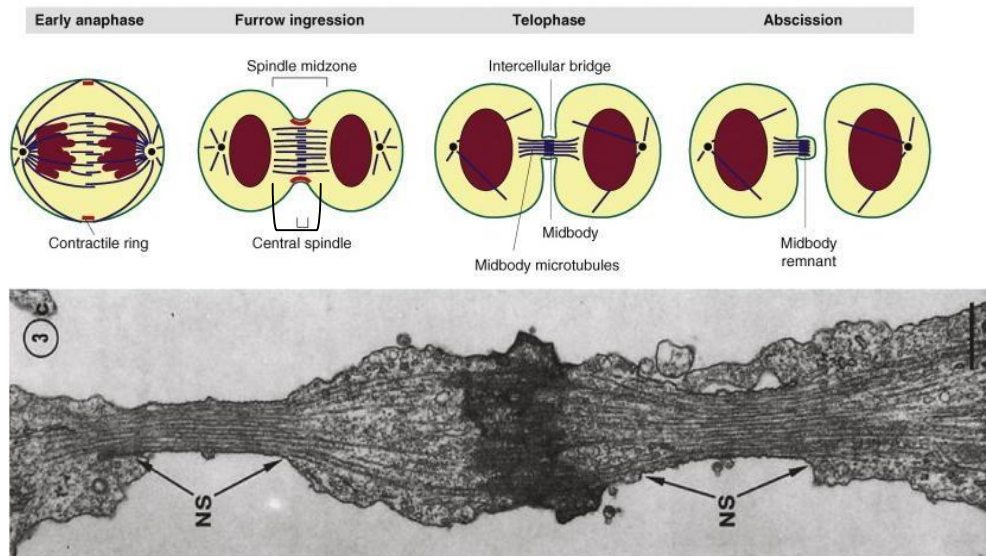


**Figure 1.7. Structures that mediate cytokinesis**

The top panel is a diagrammatic representation of the structures involved in the process of cytokinesis. MTs are in blue; contractile ring is in red; chromatin is in wine red; centrosomes are in black. The bottom panel is an electron micrograph of the late telophase intercellular bridge (Mullins and Biesele, 1977) originally published in *Journal of Cell Biology* doi: 10.1083/jcb.73.3.672. Lateral narrowed segments (NS) flank the midbody. Both upper and lower panel from (Steigemann and Gerlich, 2009) with permission from Elsevier.

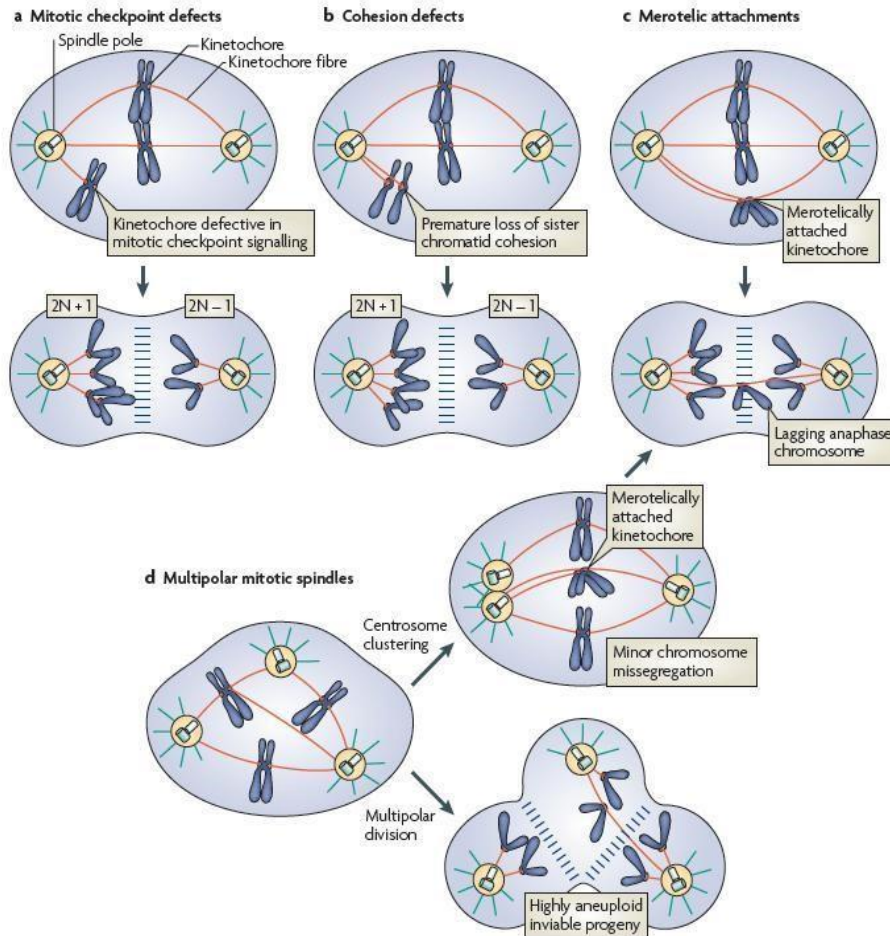


**Figure 1.8. Pathways to the generation of aneuploidy**

(a) A weak SAC allows the cell to enter anaphase before all chromosomes are bi-oriented. As a result, the two sister chromatids in a mono-oriented chromosome might be deposited into the same daughter cell. (b) Cohesion defects may lead to segregation of the two sisters to the same pole. (c) An anaphase lagging chromosome due to merotelic attachment may end up in the same daughter cell as its sister chromatid. (d) Transient spindle multipolarity may result in merotelic attachments, which may then result in anaphase lagging chromosomes and aneuploidy (as described in c), whereas multipolar chromosome segregation usually leads to a high degree of aneuploidy that is incompatible with life. From (Holland and Cleveland, 2009) with permission from Nature Publishing Group.

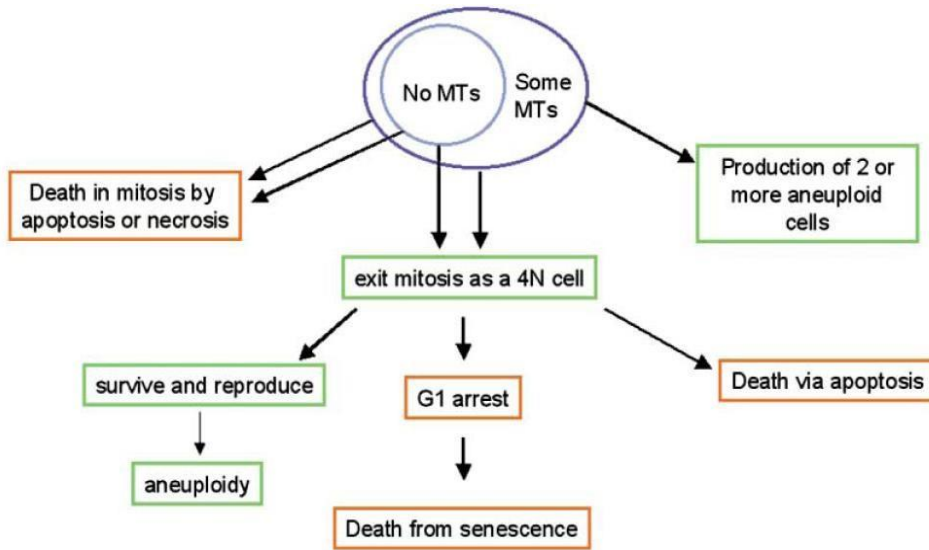


**Figure 1.9. Cells with persistently activated SAC**

The potential fates of a cell that cannot satisfy the SAC in the presence or absence of MTs (Rieder and Maiato, 2004) (With permission from Elsevier).

**Table 1.1. Motor Proteins in Spindle Assembly**

Motor-based mechanisms of spindle assembly	Motor family	Molecular motors in human	Molecular motors in other organisms	Proposed role
Spindle bipolarity	Kinesin-3 (+)	-	Klp38B (fly)	Connects spindle MTs to chromosome arms; promotes spindle stability
	Kinesin-4 (+)	-	Xklp1 (frog), Klp3A (fly)	
	Kinesin-5 (+)	Eg5	Eg5 (frog) Klp61F (fly)	Crosslinks MTs and slides antiparallel MTs outward
			Kif2a, Kif2b	Klp10A (fly), Kif2a (frog, mouse)
Spindle pole formation	Kinesin-13 (i)			Depolymerizes MTs at spindle poles
	Kinesin-14 (-)	HSET	Ncd (fly), XCTK2 (frog), CHO2 (hamster)	Slides MTs poleward; exerts antagonizing force against Kinesin-5
				Slides MTs poleward; generates cortical pulling force
Chromosome positioning	Dynein (-)	Dynein	Dynein (fly, frog, mouse)	Promotes KT-MT attachment
	Kinesin-4 (+)	-	Klp3A (fly), Xklp1 (frog)	Attaches chromosome arms to spindle and slides toward center
	Kinesin-10 (+)	Kid	Nod (fly)	
	Kinesin-7 (+)	CENP-E	CENP-E (mouse), CENP-meta (fly)	Slides unattached KTs along a k-fiber toward spindle center
	Kinesin-8 (+, i)	Kif18A	Klp67A (fly)	Dampens KT oscillations
	Kinesin-13 (i)	MCAK	Klp59C (fly), MCAK (frog)	Depolymerizes KT MTs

(+) Plus end-directed (-) Minus end-directed (i) Internal motor domain; Based on (Loughlin et al., 2008) with permission from Elsevier.

**Table 1.2. Molecular components of the spindle assembly checkpoint (SAC)**

Vertebrates	<i>S. cerevisiae</i>	<i>S. pombe</i>	Interactions and functions
Core checkpoint proteins			
Mad1	Mad1	Mad1	Binds constitutively to Mad2 and recruits it to the kinetochore; also localizes Mad2 to the nuclear periphery (NP) in interphase, function at the NP is unknown; binds to Bub1 and Bub3 upon checkpoint activation in budding yeast.
Mad2	Mad2	Mad2	Binds to Mad1 and Cdc20; exists in two conformations ('closed' C-Mad2 on binding Mad1 or Cdc20, or 'open' O-Mad2 when unbound); interacts with Cdc20 and BubR1/Mad3 to form the MCC, which inhibits the APC; excess Mad2 inhibits the APC/C in many experimental systems.
BubR1	Mad3	Mad3	Binds to Bub3; interacts with Mad2 and Cdc20 to form the MCC; C-terminal kinase domain of BubR1 is activated by CENP-E; yeast Mad3, the functional equivalent of BubR1, lacks the kinase domain.
Bub1	Bub1	Bub1	Protein kinase; binds to Bub3; requirement for recruiting other checkpoint proteins differs depending on system; kinase activity is not required for checkpoint arrest.
Bub3	Bub3	Bub3	Binds to Bub1 and the MCC components; required for Bub1 and BubR1 localization to the kinetochore.
Mps1	Mps1	mph1	Protein kinase; phosphorylated Mad1 in vitro; excess activates the checkpoint; required for recruitment of Mad1, Mad2 and CENP-E to the kinetochore.
Other proteins required for checkpoint function			
Aurora B	lpl1	ark1	Protein kinase; chromosomal passenger protein; binds INCENP and survivin; in mammals and budding yeast (lpl1) required for checkpoint response to lack of tension but not attachment; required for attachment response in fission yeast (Ark1).
RZZ complex	-	-	Complex of Rod, ZW10 and Zwilch, in higher eukaryotes only recruits dynein and Mad1/Mad2 to the kinetochore.
CENP-E	-	Spo15	Kinesin family member; binds to BubR1; stimulates BubR1 kinase activity; required for capture and stabilization of MTs at the kinetochore; only found in higher eukaryotes.
p31 comet (MAD2L1BP)	-	-	Binds specifically to the 'closed' conformation of Mad2; excess disrupts checkpoint signaling; involved in switching off the checkpoint; no yeast orthologues
-	Cdc55	-	Regulatory B subunit of PP2A; regulates Swe1 degradation
Cdc20	Cdc20	Slp1	Binds to Mad2, BubR1(Mad3), Emi1, APC, and APC substrates; activates APC; ubiquitinated by APC-Cdh1; phosphorylated by Cdk1 in mammals
-	Bub2	cdc16	Negatively regulates Tem1 and the mitotic exit network in <i>S. cerevisiae</i>
Dynein/ dynactin	Dynein/ dynactin	Dynein/ dynactin	Minus-end-directed motor that transports Mad2 and BubR1 away from the kinetochore; thought to be required for switching off the checkpoint; dynactin complex recruits 'cargo' to dynein

\*Based on (May and Hardwick, 2006; Yu, 2002) (with permission from Company of Biologists Ltd. and Elsevier respectively) and the Homologene Database of NCBI.

## Chapter 2. Dynamic bonds and polar ejection force distribution explain kinetochore oscillations in PtK1 cells

Gul Civelekoglu-Scholey<sup>1</sup>✉\*, Bin He<sup>2</sup>✉, Muyao Shen<sup>2</sup>, Xiaohu Wan<sup>3</sup>, Emanuele Roscioli<sup>2</sup>, Brent Bowden<sup>2</sup>, and Daniela Cimini<sup>2</sup>\*

<sup>1</sup> Department of Molecular and Cellular Biology, University of California, Davis, CA 95616 – USA

<sup>2</sup> Department of Biological Sciences, Virginia Tech, Blacksburg, VA, 24061 – USA

<sup>3</sup> Department of Biology, University of North Carolina, Chapel Hill, NC 27599 – USA

✉These authors contributed equally

\*Corresponding authors

J. Cell Biol., 2013 May 13; 201 (4): 577-593.

### Author contributions

Conceived and designed the experiments: GCS, BH, and DC. Performed experiments and collected experimental data: BH, MS, XW, ER, BB, and DC. Analyzed the data: BH, MS, and XW. Developed the computational/mathematical model: GCS. Performed computer simulations and analyzed simulation data: GCS. Contributed reagents/materials/analysis tools: GCS, XW, and DC. Prepared the manuscript: GCS, BH, and DC.

## **2.1. Abstract**

Duplicated mitotic chromosomes aligned at the metaphase plate maintain dynamic attachments to spindle microtubules via their kinetochores, and multiple motor and non-motor proteins cooperate to regulate their behavior. Depending on the system, sister chromatids may display either of two distinct behaviors, namely (i) the presence or (ii) the absence of oscillations about the metaphase plate. Significantly, in PtK1 cells, in which chromosome behavior appears dependent on the position along the metaphase plate, both types of behavior are observed within the same spindle, but how and why these distinct behaviors are manifested is unclear. Here, we developed a new quantitative model to describe metaphase chromosome dynamics via kinetochore-microtubule interactions mediated by non-motor viscoelastic linkages. Our model reproduces all the key features of metaphase sister kinetochore dynamics in PtK1 cells and suggests that differences in the distribution of polar ejection forces at the periphery and in the middle of PtK1 cell spindles underlie the observed dichotomy of chromosome behavior.

## **2.2. Introduction**

One of the key steps in ensuring equal partitioning of the genome during mitosis is the alignment of mitotic chromosomes at the cell/spindle equator to form the so-called metaphase plate.

Chromosome congression to the metaphase plate is favored by chromosome-MT interactions, and key players for these interactions include a number of molecular motors (e.g., CENP-E at KT's and chromokinesins along chromosome arms), structural KT components (e.g., Ndc-80 complex), and MT dynamics [reviewed in (Maiato et al., 2004a; McIntosh et al., 2002)]. Once achieved, alignment at the metaphase plate must be maintained until the onset of anaphase, as anaphase in the presence of unaligned chromosomes would inevitably result in the formation of aneuploid daughter

cells [reviewed in (Cimini, 2008)]. Like chromosome congression to the metaphase plate, maintenance of alignment is believed to depend primarily on KT-associated motors (e.g., dynein, CENP-E), chromosome-associated motors (chromokinesins), biophysical properties of the KT-MT interface (e.g., compliance of Ndc-80 molecules), and regulators of MT dynamics (e.g., kinesin 13 and Aurora B kinase). Alignment at the spindle equator can be maintained when the forces that act on the chromosomes achieve a balance (Gardner and Odde, 2006; Vladimirov et al., 2011). However, despite maintenance of overall alignment at the metaphase plate, chromosomes are not necessarily static and the plus ends of KT-bound MTs (kMTs), and thus KT-MT attachments, remain dynamic during metaphase. In some cell types, including most animal tissue culture cells, fission and budding yeast, sister KT pairs at the metaphase plate oscillate back and forth (Funabiki et al., 1993; Magidson et al., 2011; Pearson et al., 2001; Salic et al., 2004; Skibbens et al., 1993), and the chromatin between sister KTs is stretched to levels significantly above rest length (Jaqaman et al., 2010; Maddox et al., 2002; Stumpff et al., 2011; Wan et al., 2012). In other systems, such as *Xenopus* egg extracts, *Drosophila* embryos, *Drosophila* S2 cells, insect spermatocytes, oocytes, and higher plant cells, chromosomes do not exhibit oscillations (Brust-Mascher and Scholey, 2002; de Lartigue et al., 2011; Desai et al., 1998; LaFountain et al., 2001; Maddox et al., 2002; Maddox et al., 2003), although their centromeres are under tension, as indicated by the stretching between the two sister KTs. Finally, one interesting example is represented by PtK1 cells, whose chromosomes have been reported to exhibit different behaviors depending on the position along the metaphase plate. Sister KT pairs positioned at the edges/periphery of the metaphase plate (as defined by the long axis of the metaphase plate) or farthest away from the spindle long axis (see Figure 2.1A) do not oscillate, whereas chromosomes in the middle of the metaphase plate or closer to the spindle long axis (Figure 2.1A), exhibit regular oscillations back and forth about the metaphase plate (Cameron et al., 2006; Cimini et al., 2004; Wan et al., 2012).

Pioneering quantitative studies have analyzed how various components of the force-balance network may affect chromosome congression and maintenance of alignment at the metaphase plate [reviewed in (Vladimirou et al., 2011)], and the dynamics of chromosome oscillation at the metaphase plate have been carefully characterized in various experimental systems (Magidson et al., 2011; Pearson et al., 2001; Skibbens et al., 1993). However, an investigation of the mechanism(s) responsible for differences in chromosome behavior within the same, unperturbed mitotic spindle is still lacking. Thus, we have used experimental data available for PtK1 cells to examine the dichotomy of chromosome oscillation at the metaphase plate in a quantitative framework. We have then validated this novel quantitative model by experimentally testing its predictions, thus attaining a detailed understanding of how the KT-MT interface modulates metaphase chromosome dynamics.

## **2.3. Results**

### **2.3.1. Dynamics of metaphase chromosomes in PtK1 cells: oscillating and steady KT pairs.**

In PtK1 cells, KT pairs located in the middle and the periphery of the metaphase plate (Figure 2.1A) exhibit different dynamics. While middle KT pairs undergo directional instability [oscillations between the poles (Skibbens et al., 1993) Figure 1B], the peripheral KT pairs (the two outermost KT pairs, one on each side of the metaphase plate) remain stably positioned near the spindle equator, and do not oscillate (Figure 2.1C). This is evidenced by the large standard deviations for the distances between middle KTs and spindle poles (Figure 2.1D, blue) as opposed to much smaller standard deviations for the distances between peripheral KTs and spindle poles (Figure 2.1D, red). The characteristic regular oscillations displayed by middle KTs produced characteristic kinetic profiles of poleward (P) and away-from-the-pole (AP) movements (Figure 2.1E-F), as well as characteristic P and AP velocity profiles (Figure 2.1E-F, insets), consistently with previously

reported data (Wan et al., 2012). Such profiles could not be obtained for peripheral KT pairs, as they only exhibited small ( $<1 \mu\text{m}$  in amplitude) erratic movements (Figure 2.1C-D). Despite the differences in oscillations, the intra-KT distances for middle KT pairs did not differ from those observed for peripheral KT pairs (t-test,  $P=0.73$ ), whereas the inter-KT distances only displayed slight differences (t-test,  $P=0.05$ ; Figure 2.2).

### **2.3.2. Force-Balance model for metaphase chromosome dynamics in PtK1 cells.**

To investigate the mechanism underlying chromosome alignment and dynamics in PtK1 cells, we modified the Force-Balance (FB) model initially developed to describe chromosome dynamics in the *Drosophila* embryo (Civelekoglu-Scholey et al., 2006), and adapted it to PtK1 cell metaphase chromosome dynamics by appropriately changing the model parameters (e.g., number of MT attachment sites at the KT, MT dynamic instability parameters, velocity of poleward sliding motors), including a force-dependent detachment behavior of the KT (dynein and Cenp-E) and sliding motors, and assuming that the cohesin bonds between sister chromatids have viscoelastic properties (Figure S2.1A-C, Materials and Methods). In this model, the sliding motors on the kMTs generate poleward directed pulling/sliding forces (according to their force-velocity relationship), and it is simply assumed that the kMT minus ends at the spindle poles are depolymerized at the rate the kMTs slide into the poles. Thus, because in the model the sliding rate is equivalent to the kMT poleward flux rate, “sliding” and “flux” will be used interchangeably hereafter. The revised model accounted for many of the quantified aspects of the PtK1 chromosome dynamics, including the number of kMTs, the slow flux rates and MT dynamics, and their oscillation around the metaphase plate (Figure S2.1D-E), but did not reproduce the inter-KT oscillations: i.e., oscillations in the distance between a pair of sister-KTs. Indeed, it has been recently reported that during metaphase, while sister KTs oscillate between the spindle poles with period  $\tau$  (where  $\tau$  is the duration of a full

cycle, or the time it takes for a P-moving KT to return to the same position in a P-moving state), the distance between sister KTs oscillates with a period equal to half of that, i.e.  $\tau/2$  (Wan et al., 2012). We then tried to identify the possible mechanism(s) that could account for the observed differences in behavior between middle and peripheral chromosomes by varying the model parameters [e.g., number of motors per KT, polar ejection forces (PEFs), cohesin force]. The model predicts that, with the same MT dynamic parameters and MT flux rates, different behavior of the middle and peripheral KT pairs (oscillatory vs. steady) can be produced only if (i) there are higher PEFs at the spindle periphery compared to the middle of the spindle, or (ii) there are imbalances in the numbers of motors (dynein or CENP-E) at the peripheral vs. middle KTs. Because in Ptk1 cells the largest chromosomes are always positioned at the periphery of the metaphase plate (Torosantucci et al., 2009), it is reasonable to think that the larger surface area of MT-chromosome interaction may result in higher PEFs. However, when we introduced higher peripheral PEFs, the model also predicted a reduction of the inter-KT stretch, which was inconsistent with the experimental data. Lower numbers of CENP-E or higher numbers of dynein at the peripheral KTs did not suppress oscillations and resulted in increased inter-KT distances, whereas higher numbers of CENP-E or lower numbers of dynein at the peripheral KTs suppressed oscillations, but also induced a reduction in inter-KT stretching, inconsistent with the experimental data. Moreover, quantification of KT-associated CENP-E and dynein did not reveal any difference between peripheral and middle KT pairs (Figure 2.3). Thus, differences in the number of KT-associated motors could not explain the dichotomy of behavior between the middle and peripheral sister KT pairs, suggesting that, unlike in the fast *Drosophila* syncytial embryo mitosis (Bader and Vaughan, 2010), the KT motors CENP-E and dynein do not play a major role in regulating metaphase chromosome dynamics in Ptk1 cells.

### **2.3.3. New mathematical model: KT attachment to MTs through dynamic non-motor, viscoelastic bonds.**

Recent *in vivo* and *in vitro* studies have suggested a key role of non-motor linkages between MTs and KTs in yeast and tissue culture cells (Akiyoshi et al., 2010; Asbury et al., 2011; Joglekar and DeLuca, 2009; McIntosh et al., 2008; Powers et al., 2009). Based on these studies and the observation that MT-attached KTs undergo intra-KT deformations (Dumont et al., 2012; Maresca and Salmon, 2009; Uchida et al., 2009), we revised our FB model for chromosome motility to explore if dynamic non-motor, viscoelastic bonds between MTs and KTs could account for the observed behavior of metaphase chromosomes in PtK1 cells. It is important to specify that the assumption that both the KT-MT bonds and the cohesin bonds have viscoelastic, instead of simply elastic, properties is essential to produce smooth rather than jerky KT movements, and ensures that the KT oscillations as well as the changes in intra-KT distances are smooth and similar to the dynamic behavior observed experimentally. Based on these assumptions, we considered viscoelastic dynamic linkages between the dynamic MT plus ends and the KTs, in the absence of MT-based motors (Figure 2.4A-C). Within this minimal FB approach, we wished (i) to address if dynamic viscoelastic attachments of the sister KTs to multiple and dynamic MT plus ends provide a robust attachment of metaphase sister KTs to MTs undergoing poleward flux; (ii) to quantitatively address if force-sensitive stochastic attachment/detachment of viscoelastic linkages coupled to MT poleward sliding/flux is sufficient to account for the experimentally observed chromosome behavior; (iii) to identify which components, or properties of the components in the FB model (by inference, the molecules in the spindle) are at the core of the observed metaphase chromosome oscillations; and (iv) to investigate which geometric property of, or inhomogeneity in the

spindle/chromosomes could govern the dichotomy in the behavior of metaphase sister KT pairs within the PtK1 spindle.

Our new FB model describes the dynamics of sister KT pairs, which interact, via viscoelastic linkages, with multiple MTs that undergo dynamic instability at their plus ends and slide poleward and depolymerize at their minus ends. It is worth noting that the viscoelastic linkages in our model could depend on the viscoelastic properties of any or all of the components of the KNL1–Mis12 complex–Ndc80 complex (KMN) network (Cheeseman and Desai, 2008) at the outer KT.

However, because the Ndc80 complex has been shown to be the KMN subcomplex that directly binds MTs (Cheeseman et al., 2006; DeLuca et al., 2006), we will refer to the Ndc80 complex as the key element in the KT-MT viscoelastic linkages of our model. In the model, the velocities of the sister KTs, and the poleward flux/sliding velocities of the kMTs are dependent on the sum of the poleward and anti-poleward forces exerted on them by the cohesin links between the sister KTs, the bound Ndc80 complexes, the force exerted on the kMTs by the poleward flux motors/depolymerases ‘reeling in’ or ‘sliding’ the MTs poleward, and the viscous drag on the KTs and the MTs (Figure 2.4). In the absence of forces generated by poleward-directed motors at the KT, the sole poleward force generators/transducers at the KT are the bound and stretched Ndc80 complexes. At a given time, different Ndc80 complexes anchored to the same kMT may exert forces of different magnitude, reflecting their current stretch/compression as a result of their uncoordinated stochastic attachment/detachment events. In the model, we assume that the binding rates of the Ndc80 complex to polymerizing or depolymerizing MTs are the same, but the detachment rates from polymerizing or depolymerizing MTs differ. Namely, we assume that the detachment of the Ndc80 complexes from depolymerizing MTs occurs in a biphasic, force-sensitive manner (it is high at low force, decreases at moderate force, then increases again under high force), while the detachment rate from polymerizing MT tips increases linearly with force (see Materials

and Methods, Figure 2.4D, S2, and Table I). In this minimal model, we do not account for additional poleward pulling forces which may stem from the power-stroke/curling out of depolymerizing protofilaments (Asbury et al., 2011; Grishchuk et al., 2005) to which the Ndc80 complexes may be attached. We do not account for polymerization ratcheting forces at the inner-KT plate either, and simply assume that MT polymerization at the plus end stalls at a critical distance from the inner-KT plate. The specific assumptions of the model are summarized in Table 2.1. The model was initially constructed with a minimal set of assumptions (Table 2.1 A), and the assumption set was gradually augmented (Table 2.1 B-C), until the model reproduced the experimentally observed behavior of metaphase sister KT pairs. Based on the core equations in Figure 2.4D, a large set of coupled FB-model equations (typically 52-102 equations, ranging from 25-50 kMT for each of the two sister KTs) was constructed. These equations were then solved numerically using a custom-made MATLAB script in an iterative process (see Materials and Methods for details).

#### **2.3.4. Model results: robust attachment of KTs to spindle MTs, and oscillations of middle sister KT pairs.**

The minimal model described above faithfully reproduces the metaphase oscillations of sister KTs (in amplitude, and period) and the inter-KT distance observed in PtK1 cells (Figure 2.5A-C), including the recently documented period doubling in inter-KT distance for oscillating KT pairs [(Dumont et al., 2012; Wan et al., 2012); Figure 2.5A, green trace]. The model also accounts well for a number of experimental observations, including inter- and intra-KT distance distributions (Figures 5C and D, respectively) for the oscillating sister KT pairs, the average number and the evolution of the number of bound kMTs [Figure 2.5E; (VandenBeldt et al., 2006)], and MT

poleward flux rates (Cameron et al., 2006). In addition, the time evolution of the numbers of attached MTs and that of the bound Ndc80 complexes corresponding to the P- and AP-moving sister KTs (Figure 2.5E-F) provide insight into the KT change in direction from P to AP movement during oscillations, illustrating that it is the number of bound Ndc80 complexes and not the number of MTs that determines the switch. Furthermore, the differences in the mean and maximal intra-KT stretch (i.e., the distance between the inner KT and the average position of the MT-bound Ndc80 complexes, and the distance between the inner KT and the farthest attached Ndc80-complex, respectively) for the P- and AP-moving sister KT (Figure 2.4C), show that the maximal intra-KT stretch matches the recently documented data for PtK2 cells where the AP-moving sister was found to exhibit higher intra-KT stretch (Figure 2.5G-H). Finally, the model can reproduce the experimentally observed P and AP kinetics [compare Figures 5I-J and 1E-F; (Wan et al., 2012)]. Both the model and the experimental data also show that the AP-moving KT reaches its maximum speed earlier than the P-moving KT [Figures 5I-J and 1E-F, insets; (Wan et al., 2012)]. In fact, these differences in acquisition of the maximal speed during P and AP movement are responsible for the observed period doubling in the inter-KT distance [(Dumont et al., 2012; Wan et al., 2012); Figure 2.5A]. Our model suggests that this is due to the biphasic kinetics of the Ndc80 bonds attached to depolymerizing MTs, resulting in a slower turnover of the kMT-bonds of the P-moving sister (under moderate tension), hindering the increase in P velocity until a critical tension level is reached. The proposed biphasic dissociation kinetics of Ndc80 complexes is not a general property of molecular motors and may underlie how different organisms employ and rely on motor or non-motor proteins for chromosome alignment and dynamics.

The positive feedback, which results in sister KT oscillations about the metaphase plate, and the phase difference between the oscillatory behavior of the sister KTs causing the period-doubling of the inter-KT distance oscillations can be understood as follows. At the spindle equator, the sister

KTs initially have no advantage over one another in terms of forces, and their Ndc80 complex-MT bonds turnover with similar dynamics as they attach to MTs, stretch and detach. However, when a KT stochastically acquires attachment to a higher ratio of depolymerizing/polymerizing MTs compared with its sister KT, and begins moving poleward slowly, it gains an advantage in ‘bond-stability’ for its depolymerizing kMTs. This is due to the biphasic force-sensitivity of the detachment kinetics: at moderate tension, the Ndc80 bonds with depolymerizing MTs are stabilized ( $k_{\text{off}}$  is low), while those with low or high tension turnover rapidly. Furthermore, the P-movement enhances the catastrophe frequency of polymerizing kMT plus ends, thus increasing the ratio of depolymerizing/polymerizing MTs further, and at the same time increasing the P-movement rate of the KT, which relieves the tension on the Ndc80-complexes, allowing them to turn over for effective motility. When the sister KT begins its P-movement, its sister KT may also initially take (smaller) poleward steps, but it quickly stalls, then begins AP-movement due to increasing cohesin forces. As the AP-moving sister gains speed due to increasing cohesin pulling forces, the Ndc80-bound depolymerizing MTs either lose their attachment due to high tension (the biphasic force-dependence) or switch to polymerization due to increased rescue frequency, enhancing the AP sister’s disadvantage in the ratio of depolymerizing/polymerizing kMTs. As the P-moving KT approaches its pole, the PEFs slow down its movement, elevating the Ndc80 tension again, and either causing the Ndc80 complexes to detach from depolymerizing MTs or leading to a rescue event of the kMT plus ends, shifting the advantage to the sister KT.

A highly attractive feature of this minimal model is the robustness of the KT-MT attachments to changes in the model parameters. For example, changing (within a reasonable range, see Table S1) the number of MT attachment sites per KT, the number of Ndc80 complexes per MT, or the MT plus end dynamic rates, does not compromise faithful attachment of the KT to spindle MTs, and the qualitative aspects of chromosome dynamics are not affected. However, to reproduce certain

specific aspects of chromosome dynamics observed experimentally, such as the period of inter- and intra-KT oscillations and the kMT number and poleward flux rates, fine-tuning of the parameters is required.

### **2.3.5. Model results: identification of parameters that suppress oscillations of the peripheral KT pairs.**

Next, we tested the model to identify changes in the parameter(s) that could account for the observed behavior of the peripheral sister KT pairs (Cameron et al., 2006; Cimini et al., 2004; Wan et al., 2012), characterized by small ( $<1 \mu\text{m}$  in amplitude) erratic movements and lack of oscillations. We tested a number of conditions, including differences in number of kMTs per KT, PEFs, and MT sliding forces due to the geometry of the spindle (in these fairly flat mitotic PtK1 cells, the average angle between the k-fiber and the peripheral KTs is 35 degrees, in contrast with an average angle of 90 degrees for the middle KTs), differences in the catastrophe rate for the MT plus ends bound to the peripheral KTs (peripheral KTs have longer kMTs due to the geometry of the spindle and their position), and some combinations of the above possibilities (some shown in Table II). We found that only a non-linear distribution of the PEFs characterized by a sharp increase at short distance from the spindle equator (see Material and Methods, Figure 2.6A), led to the suppression of oscillations and at the same time produced inter- and intra-KT distances that matched the experimental data (Table II, Figure 2.6B-E; see also Figure 2.6F-G for evolution of the number of MTs and Ndc80 complexes). Indeed, simply decreasing the magnitude of the PEFs while maintaining a linear increase around the metaphase plate was not sufficient, as under these conditions oscillations were suppressed [as in (Stumpff et al., 2012)], but the inter-KT distances were significantly higher than those observed experimentally. Thus, we propose that the

distribution of PEFs differs in the middle and the periphery of the spindle in PtK1 cells, and this governs the observed dichotomy in behavior of middle and peripheral KT pairs. Specifically, our model suggests that while PEFs increase linearly around the spindle equator for middle KTs, they increase sharply for the peripheral KTs (Figure 2.6A). This finding is consistent with laser ablation studies in which reduced PEFs resulted in increased amplitude of oscillations (Ke et al., 2009).

### **2.3.6. Model predictions and experimental tests.**

Our model makes a number of testable predictions (i-iv below), some of which are supported by recently published work and some others that have been experimentally tested here.

(i) As the sister KTs begin their excursion, the fraction of kMTs in

depolymerization/polymerization state for the P-moving chromosome initially increases, then

decreases, while that of the AP-moving sister initially diminishes rapidly, then remains constant

(low) until turnaround.

(ii) Both the average and the maximal intra-KT distance oscillate. Specifically, the maximal intra-

KT stretch of the AP-moving sister KT is, on average, larger than that of the P-moving

chromosome, and it oscillates with a period roughly twice that of the sister KT oscillations about the

metaphase plate (see Figure 2.5G-H). Recent work by Dumont and colleagues in PtK cells showed

that indeed the intra-KT stretch for P- and AP-moving KTs is different [intra-KT distance for P-

moving KT smaller than for AP-moving KT (Dumont et al., 2012)], providing support to our model results.

(iii) When the detachment rate of the Ndc80 complex from MTs is inhibited, the sister KTs become

hyperstretched [(DeLuca et al., 2006); Figure 2.7A, C] solely due to the poleward sliding/flux of

kMTs bound to the sister KTs. Therefore, co-inhibition of poleward flux will reduce the inter-KT

stretch (Figure 2.7C-D), but maintain fully attached (thick k-fibers) sister KTs. To test this prediction, we performed microinjection experiments with antibodies to the N-terminus of Hec1 [as in (DeLuca et al., 2006)] and/or Kif2a (kindly provided by Dr. Duane Compton, Dartmouth Medical School), which is believed to be the major depolymerase at the spindle poles responsible for MT poleward flux (Ganem and Compton, 2006; Ganem et al., 2005). Indeed, pilot experiments showed that injection of Kif2a antibodies in PtK1 cells significantly reduced poleward flux of kMTs (Bennett, He, and Cimini, unpublished). Such reduction in MT poleward flux produced a decrease in the inter-KT distance compared to uninjected cells (Figures 7E-F, I-J, M-N), as predicted by our model (Figure 2.7A-B). Injection of Hec1 antibodies, on the other hand, induced a significant increase in inter-KT stretching (Figures 7G, K, O compared to 7E, I, M), supporting our model prediction (Figure 2.7C, A) and confirming previous observations (DeLuca et al., 2006).

Importantly, when we co-injected Hec1 and Kif2a antibodies, we observed a significant reduction of inter-KT stretching (Figure 2.7H, L, P) as compared to injection of Hec1 antibody alone (Figure 2.7G, K, O), once again supporting our model predictions (Figure 2.7C-D).

(iv) Forces generated by poleward flux motors on spindle MTs coupled to dynamics of MT plus ends at the KT are sufficient to generate the experimentally observed inter- and intra-KT stretching. Indeed, simulations in which the poleward flux was reduced, produced a reduction in inter-KT stretch (Figure 2.7B) compared to controls (Figure 2.7A). This prediction was supported by our experimental observation of reduced inter-KT stretch in cells microinjected with Kif2a antibodies (Figures 7F, J, N compared to 7E, I, M).

## 2.4. Discussion

The data presented here highlight how differences in the distribution of PEFs can affect metaphase chromosome oscillations, and suggest that biphasic, force-dependent detachment kinetics of Ndc80 complexes can drive the inter-KT distance oscillations observed in metaphase for oscillating sister KT pairs. Instead, the length- and polymerization rate-dependent catastrophe frequency, and the tension-dependent rescue frequency of MT plus ends play more subtle roles, by coordinating the dynamics of the plus ends of MTs attached to sister KTs to achieve efficient motility, and, together with the viscoelasticity of cohesin and Ndc80 complexes, contribute to smooth-out the otherwise jerky chromosome movements.

### *2.4.1. What causes the inhomogeneity in the distribution of PEFs within the PtK1 cells metaphase spindle?*

We found that a difference in the distribution of the PEFs at the periphery vs. the middle of the spindle can explain the differences in oscillations between peripheral and middle KT pairs in PtK1 cells. The predicted difference between the PEFs exerted on middle vs. peripheral KTs can be explained by a number of specific features of PtK1 mitotic cells: (i) the chromosomes aligned at the periphery of the metaphase plate always correspond to the two chromosomes 1 (Torosantucci et al., 2009), which are large acrocentric chromosomes, with a very long q arm (Torosantucci et al., 2009). Such large arm size results in high baseline PEF magnitude for peripheral KTs (see Materials and Methods for further details). (ii) Chromosomes at the periphery are fully exposed to non-KT MTs, whereas middle chromosomes are partly shielded due to the crowding in the middle of the metaphase plate, where each chromosome is surrounded by other chromosomes. (iii) Because the KT-to-pole distance is greater for peripheral KTs, the length-dependent catastrophe frequency of

MT plus ends (Varga et al., 2009) gives rise to a sharp drop in PEFs in close proximity of the spindle equator. Thus, the peripheral chromosome arms are exposed to low PEFs within a narrow region right around the spindle equator, but are exposed to sharply increasing PEFs as soon as they move away from the equator (see Figure 2.4A).

One could argue that other forces arising from the great “crowding” within the mitotic spindle may affect the dynamics of metaphase chromosome behavior. For instance, forces exerted by chromosome arms bumping into one another, inability of MTs to interact with all chromosomes in the same manner, and elastic MT forces exerted on the chromosomes are additional (stochastic) factors that are not considered in our model. However, the experimentally observed regularity of the middle sister KT oscillations suggests that the sum of these forces are of negligible magnitude compared with the forces that drive KT movements. In fact, the ‘crowded’ organization of the spindle would also cause chromosome arms to shield their neighboring chromosomes from spindle MTs, particularly in the context of the middle KTs. We suggest that this would contribute significantly to the proposed differences in the PEFs for the middle and peripheral sister KTs, yielding a sharp increase of the PEFs around the spindle equator for the peripheral sister KTs, with no neighbors, and a linear increase in PEFs around the spindle equator for the middle sister KTs, with many neighbors. Thus, the averaged sum of forces due to ‘crowding’ is implicitly included in our current model via the PEF profiles for the middle and the peripheral sister KTs (Figure 2.6A).

#### ***2.4.2. Comparison with previous models***

The model developed and presented here is closely related to the model developed by Joglekar and Hunt for PtK1 chromosome dynamics (Joglekar and Hunt, 2002), where the authors investigated the Hill-sleeve model (Hill, 1985) in a FB approach. Our model differs from theirs in the following

ways: first, the Joglekar and Hunt model (2002) did not consider poleward flux of kMTs. Next, in the Joglekar-Hunt model the attachment sites of KT to each MT are arranged in series in form of a ‘sleeve’, with multiple sleeves per KT, arranged in parallel. The sleeves are linked to the KT through springs (elastic bonds). In this way, the poleward movement of a sleeve with respect to its MT requires the detachment and re-binding of all bonds, setting a large energy barrier for the movement at high sleeve insertion depths. This mechanism effectively prevents the poleward movement of a sleeve (and hence its KT) when the MT is in polymerization state, which leads to deeper insertion of the MT into the sleeve, while favoring the poleward movement of a sleeve (and hence its KT) when the MT is in depolymerization state, which reduces the insertion depth. Thus, in the Joglekar-Hunt model, the primary factor driving P and AP KT movement is MT dynamics. In contrast, individual KT-MT bonds (Ndc80 complexes) are independent from one another in our model, and while the primary factor driving the P movement is poleward flux by pulling on the MT-bound Ndc80 complexes, the depolymerization rate of kMT plus ends is governed by the dynamics of the bonds, which in turn are regulated by tension forces. Like Joglekar and Hunt, we assume that the bonds have a high affinity for the MT, but in our model, these bonds detach in a force-sensitive manner, with different kinetics, from polymerizing and depolymerizing MT tips, and independently from one another. Specifically, we assume that when a bond is under moderate levels of tension, detachment is favored from a polymerizing MT tip, and suppressed from a depolymerizing MT tip (prolonging the bond half-life on depolymerizing MTs), but at high levels of tension, detachment is also favored from a depolymerizing MT tip (Akiyoshi et al., 2010). Consequently, in contrast with what is observed in the Joglekar-Hunt model, in our model bonds with a polymerizing MT are generally ‘weak’, and those with a depolymerizing MT are generally ‘strong’. In addition, we assume that the tension exerted on a MT tip by the KT-MT bonds is sufficient to alter MT plus end dynamics to account for the slip-clutch mechanism proposed by others (Maddox et al., 2003).

Other FB models have also been developed to account for the metaphase chromosome behavior in *Drosophila*, or fission yeast (Civelekoglu-Scholey et al., 2006; Courtheoux et al., 2009; Gay et al., 2012). The FB model developed by Courtheoux and colleagues (Courtheoux et al., 2009) addresses the correction of merotelic attachments in fission yeast during anaphase and does not account for amphitelic KT pairs. This model is derived from a previous model (Civelekoglu-Scholey et al., 2006) with additional and significant simplifying assumptions. Similarly to the model by Courtheoux et al. (2009), another quantitative model recently developed by the Tournier group to account for the dynamics of amphitelic KT pairs in fission yeast (Gay et al., 2012), relies upon a macroscopic approach. There too, all KT components are represented by a homogeneous viscoelastic ‘unit’ that can attach/detach from MTs, and neither individual MTs’ plus-end positions and dynamics, nor the reciprocal effect of the KT and the MT plus end dynamics on the attachment to/detachment from the KT are considered. Furthermore, since individual MTs are not accounted for, a MT is assumed to instantly switch to polymerization or depolymerization and to follow the direction of the KT upon attachment. Therefore, the questions that form the basis of our study, namely (i) how are the growth/shrinkage state and rate of different MTs attached to each KT coordinated?, and (ii) how is the movement of the sister KTs coordinated to give rise to the observed movements of sister KT pairs?, are not and cannot be addressed in the framework proposed by Gay et al.

The framework of the FB model developed for the fast mitosis of the *Drosophila* embryo (Civelekoglu-Scholey et al., 2006) forms the basis of the model presented here. This primary model, which relied on a major role of the two antagonistic KT motors dynein and CENP-E, and the two members of the kinesin-10 family MT depolymerases located at the KTs and at the spindle poles, can be adapted to account for many aspects of the metaphase chromosome dynamics in PtK1 cells, specifically by incorporating force-sensitive detachment rates for the KT motors dynein and CENP-

E. However, the experimental test of this model's predictions on the observed dichotomy in the behavior of middle and peripheral KT's in PtK1 cells fails to validate the model and its central assumption that motors drive metaphase chromosome dynamics in PtK1 cells. In addition, with this model, we could not identify a set of parameters that could account for the observed period doubling of inter-KT stretch (Wan et al., 2012). This suggests that the KT motors dynein and CENP-E may be functioning as a back-up (error correction) or fine-tuning mechanism for the KT-MT attachment enabled by non-motor linkages that drive the metaphase chromosome dynamics in PtK1 cells, and underscores how even highly conserved molecular mechanisms may be differentially deployed in different organisms.

#### *2.4.3. The importance of understanding kinetochore dynamics*

The model developed in this study incorporates important emerging features of the eukaryotic KT and recapitulates the complex dynamic behavior of metaphase chromosomes in PtK1 cells. As such, this model can be extended to account for chromosome behavior in other cell types by altering specific parameters and adding forces resulting from plus and/or minus end directed motors at the KT to the core model equations. Moreover, this model can be used to investigate the behavior and dynamics of mis-attached KT's. Finally, the work presented here sets the quantitative framework to investigate the role of various mechanisms, such as the gradient of centromeric Aurora B, the dynamics of Ndc80 attachment and detachment, the MT plus end dynamics, and the MT poleward sliding forces, proposed to contribute to correction of KT mis-attachments (Cimini et al., 2006; DeLuca et al., 2006; Ganem et al., 2005). Indeed, whereas chromosome oscillations are not absolutely required for the execution of mitosis, as several cell types that do not display chromosome oscillations can successfully segregate their chromosomes, the dynamics of oscillation

or lack thereof inform us on the dynamics of KT-MT interactions, which play a key role in the correction of KT mis-attachments. Thus, the model developed here will be invaluable in helping us understand the correction mechanisms of KT mis-attachment that are essential to prevent chromosome mis-segregation and aneuploidy.

## **2.5. Materials and Methods**

### ***2.5.1. Experimental methods.***

#### **2.5.1.1. Generation of HEC1-GFP PtK1 cell line.**

PtK1 cell line stably expressing the human HEC1 gene fused in frame with the EGFP was produced through the transduction of retroviral particles according to the instructions for high-titer retrovirus production provided by Clontech. The EGFP-N1 plasmid carrying the HEC1 gene was a kind gift from Dr. Jennifer DeLuca (Colorado State University, Fort Collins, CO). Briefly, the HEC1-EGFP gene was initially subcloned into the XhoI and NotI sites of the pLNCX2 retroviral vector (Clontech Laboratories, Inc.) that harbors the Y packaging sequence. In order to produce high efficiency retroviral particles, we transfected the packaging GP2-293 cells (Clontech Laboratories, Inc.), carrying the viral *gag* and *pol* genes, with the pLNCX2-HEC1-EGFP plasmid together with the VSV-G vector (Clontech Laboratories, Inc.) that provided the viral envelope gene (*env*). The resulting retroviral particles were used to infect PtK1 cells that were subsequently placed under selection in Geneticin-containing media to obtain the final HEC1-GFP PtK1 cell line used in this study.

### **2.5.1.2. Cell culture.**

PtK1 and HEC1-GFP PtK1 cells were grown in HAM's F-12 media (Invitrogen) supplemented with 5% Sodium Pyruvate (Invitrogen), 1% antibiotic-antimycotic (Invitrogen), and 10% fetal bovine serum (Invitrogen), and maintained at 37°C in a humidified CO<sub>2</sub> incubator. For experiments, cells were grown on sterilized acid-washed coverslips inside 35 mm Petri dishes for 48 hours before fixation/observation.

### **2.5.1.3. Immunostaining.**

For Hec1/ACA/ $\gamma$ -tubulin staining, cells were prefixed in freshly prepared 4% formaldehyde for 5 seconds before a 5-minute lysis in 0.5% Triton X-100 in PHEM buffer (60mM Pipes, 25mM HEPES, 10mM EGTA, 2mM MgSO<sub>4</sub>, pH 7.0] and 20-minute fixation in 4% formaldehyde. For CENP-E and dynein staining, cells were briefly rinsed in Phosphate Buffered Saline (PBS), fixed in freshly prepared 4% formaldehyde for 20 min, and then permeabilized with 0.1% Triton X-100 in PHEM buffer for 10min. A one-hour block in 10% BGS (boiled goat serum) at room temperature was followed by overnight incubation with primary antibodies diluted in 5% BGS in PHEM buffer at 4°C. Cells were then washed four times in PBS with 0.1% Tween 20 (PBST), incubated with secondary antibodies for 45 min, washed in PBST, stained with DAPI, and mounted on microscope slides with an anti-fading solution containing 90% glycerol, 10% Tris buffer, and 0.5–1% n-propyl galate. Primary antibodies were diluted as follows: human-ACA (anti-centromere antigen; Antibodies Inc.), 1:100; mouse anti-Hec1 (Abcam), 1:500; rabbit anti-tubulin (Abcam), 1:200; rabbit anti-CENP-E (a generous gift of Dr. Tim Yen, Fox Chase Cancer Center, Philadelphia, PA), 1:200; mouse anti-dynein-IC (Sigma-Aldrich Corp.), 1:100. Secondary antibodies were diluted as

follows: Red-X-goat anti-human (Jackson ImmunoResearch Laboratories Inc.), 1:100; Cy5 goat anti-rabbit (Invitrogen), 1:100; Alexa-488 goat anti-mouse (Invitrogen), 1:200.

#### **2.5.1.4. Microinjection.**

Kif2a antibodies were purified by IgG affinity purification (Nab Spin Kit, Thermo Scientific) from rabbit anti-Kif2a total serum (generous gift of Dr. Duane Compton, Dartmouth Medical School). For microinjection, both Kif2a and Hec1 9G3 (Abcam) antibodies were dialyzed and concentrated into HEK buffer (20 mM HEPES, 100 mM KCl, and 1 mM DTT, pH 7.7) to a final concentration of 1.45 mg/ml. Cells were injected with HEK buffer alone (controls), Kif2a or Hec1 9G3 antibody solution diluted 1:1 in HEK buffer (Kif2a alone or Hec1 alone), or a 1:1 mixture of Kif2a and Hec1 9G3 antibodies (Kif2a + Hec1 antibody co-injection). For microinjection, coverslips with HEC1-GFP PtK1 cells were mounted into modified Rose chambers (Rieder and Hard, 1990) without the top coverslip and incubated at 37°C with Phenol Red-free L-15 media (Gibco) complemented with 4.5 g/l glucose and covered with mineral oil to prevent evaporation. A volume corresponding to about 5% of the cell volume was injected into late prometaphase/early metaphase cells using a Narishige micromanipulator (NT-88-V3, Narishige) and a Harvard Apparatus microinjection system (PLI-100A, Harvard Apparatus).

#### **2.5.1.5. Microscopy and image acquisition.**

For inter- and intra-KT stretching analysis, immunostained cells were imaged with a swept field confocal unit (Prairie Technologies) attached to a Nikon Eclipse TE2000-U microscope (Nikon Instruments Inc.). For CENP-E and dynein fluorescence intensity quantification, immunostained cells were imaged with a Nikon Eclipse Ti inverted microscope (Nikon Instruments Inc.) with Lumen 200PRO fluorescence illumination system (Prior Scientific). This latter set up was also used

for live-cell imaging of microinjected cells. Both microscopes were equipped with motorized stages (Prior Scientific) and on both microscopes images were obtained with an HQ2 CCD camera (Photometrics), using a 100X/1.4NA Plan-Apochromatic phase-contrast objective lens. Digital images were acquired using the NIS Elements software (Nikon Instruments Inc.). For fixed cells, Z-series stacks were obtained at 0.6- $\mu\text{m}$  steps. A data set obtained during a previous study (Cimini et al., 2004) was used for initial characterization of chromosome dynamics (Figure 2.1B-F). For the microinjection experiments described in Figure 2.7, imaging began shortly after injection. Near-simultaneous phase contrast and single focal plane epifluorescence images were acquired every 20 seconds for at least 11 minutes.

#### **2.5.1.6. Image analysis.**

For each cell, measurements were taken on four pairs of sister KTs. Two pairs closest to the spindle long axis were chosen as representative of the middle KT pairs (see Figure 2.1A), whereas the two outermost pairs of sister KTs (one on each side of the spindle axis, at the periphery of the metaphase plate) represented the peripheral KT pairs (see Figure 2.1A). To measure the inter- and intra-kinetochore distances, fluorescence intensity profiles for the ACA and Hec1 signals were generated automatically by the NIS Elements software (Nikon Instruments Inc.). The inter-KT distance was measured as the distance between the two centroids of the X-rhodamine labeled ACA within a sister KT pair (Figure 2.2B). The intra-KT distance was measured as the distance between the centroids of the X-Rhodamine labeled ACA and the Alexa-488 labeled Hec1 fluorescent signals within a single KT (Figure 2.2C). Kinetochore fluorescence intensity of various antigens was measured with ImageJ using a method adapted from Hoffman et al. (Hoffman et al., 2001). Two circles with diameter of 1.12 $\mu\text{m}$  and 1.47 $\mu\text{m}$  (with area  $A_{\text{inner}}$  and  $A_{\text{outer}}$ ) were centered over each KT on an appropriate focal plane, and the integrated intensity was measured for each circle and as  $F_{\text{inner}}$  and

$F_{\text{outer}}$ . The mean background fluorescence ( $F_{\text{meanbg}}$ ) was represented by the mean fluorescence in the ring area between the two circles:  $F_{\text{meanbg}} = (F_{\text{outer}} - F_{\text{inner}}) / (A_{\text{outer}} - A_{\text{inner}})$ . The total fluorescence intensity of the protein is:  $F = (F_{\text{inner}} / A_{\text{inner}} - F_{\text{meanbg}}) * A_{\text{inner}}$ . The total fluorescence intensity for the motor protein of interest was represented as a fraction of the ACA fluorescence intensity at the same KT.

#### **2.5.1.7. Kinetochore tracking.**

Two middle and two peripheral KT pairs (see Figure 2.1A) were tracked for each time-lapse movie. Alexa 488-anti-CENP-F signals (Figure 2.1B-F) were tracked automatically using a previously developed MatLab (Math-Works, Natick, MA) program (Wan et al., 2012). HEC1-GFP signals were tracked manually aided by the same MatLab program (Wan et al., 2012). KT position was defined as the Alexa 488/GFP signal centroid based on a 2-D Gaussian fitting method (Wan et al., 2012).

#### **2.5.2. Modeling methods.**

In all descriptions below, the sister chromatids' behavior is described along the pole-pole axis of the spindle, in one dimension. The positions of the kinetochores and the microtubules' plus and minus ends correspond to distances from the spindle equator, located at the origin ( $x = 0$ ), and the positions of the left and right spindle poles are  $x = -6.5$  and  $x = 6.5$   $\mu\text{m}$ , respectively, mimicking the metaphase steady state spindle length of  $\sim 13$   $\mu\text{m}$  in PtK1 cells. All forces and velocities associated with the right and left KTs and kMTs are assumed to be positive in the poleward direction (towards the right pole for the KT tethered to the right pole, and towards the left pole for the KT tethered to the left pole). The time-dependent position of the right and left sister KTs ( $X_{KT}^R$  and  $X_{KT}^L$ ), the right

and left-KT attached  $i^{\text{th}}$  kMT's plus end ( $x_{kMT,i}^R$  and  $x_{kMT,i}^L$ ), and the pole proximal end of the right and left sister KT's  $i^{\text{th}}$  kMT's  $k^{\text{th}}$  Ndc80 complex ( $x_{Ndc80}^{R,i,k}$  and  $x_{Ndc80}^{L,i,k}$ ) are all measured with respect to the spindle equator (Figure 2.4A-C). The time-dependent velocities of the right and left sister KTs, and the poleward sliding/flux velocity of the  $i^{\text{th}}$  kMT attached to the right and left sister KT are:  $v_{chr}^R$ ,  $v_{chr}^L$ ,  $v_{kMT,i}^R$  and  $v_{kMT,i}^L$ , respectively (Figure 2.4C).

In our models, we make the following simplifying assumptions:

- (i) The motility events examined here are exclusively driven by an intrinsic balance of forces generated in the spindle;
- (ii) Throughout metaphase, spindle length (pole-pole distance) is maintained by a balance of antagonistic forces generated at anti-parallel overlapping interpolar MTs and by astral MTs, and in this model, as in previous considerations of KT positioning (Civelekoglu-Scholey et al., 2006; Joglekar and Hunt, 2002), we do not address how changes in spindle pole positions can/may affect KT positions and vice-versa;
- (iii) All motor protein/non-motor linkage (Ndc80 complex)-generated forces at the KTs or on the MTs are additive. For motor proteins, the total force depends linearly on the total number of attached/active force generators (i.e. motors share the load equally). For non-motor linkages (Ndc80 complexes) the force exerted on the MT and the KT by each molecule is proportional to its tension/compression. We assume that all motor enzymes considered have linear force-velocity relationships, and the attachment/detachment kinetics of each motor in response to applied force is considered explicitly in a Monte-Carlo approach in the current models (Coppin et al., 1997; Svoboda and Block, 1994; Valentine et al., 2006);
- (iv) Active MT depolymerases (kinesin-13) located at the spindle poles depolymerize the kMT minus ends at the same rate at which MTs slide into the poles through the action of sliding motors,

and additional poleward pulling forces which may result from the depolymerization activity of depolymerases are assumed to be of negligible magnitude and ignored.

### 2.5.2.1. Model Framework.

Both models consist of a large set of coupled FB equations describing the poleward and anti-poleward forces exerted on the left and right sister KTs, and on each kMT attached to the left and right sister KT (Figure 2.4A, D). The forces accounted for in the models are:

- (a) For each sister KT: (i) cohesin generated forces (AP directed); (ii) sum of forces generated by attached and active KT-motors (or Ndc80 complexes) at the KT (P or AP directed); (iii) PEFs (AP or P directed); (iv) polymerization ratcheting forces generated by kMT plus ends which impinge on the inner KT plate (AP directed); and (v) viscous drag forces on the chromosome (P or AP directed).
- (b) For each kMT attached to a KT: (i) sum of poleward sliding-motor generated forces (P directed); (ii) sum of the kMT, attached and active KT-motor (or kMT attached Ndc80 complex) generated forces (AP or P directed); (iii) polymerization ratcheting forces generated by the kMT plus end when it impinges on the inner KT plate (P directed). We neglect the viscous drag forces on the kMT (Howard, 2001).
- (c) MTs not attached to the KT but within the k-fiber are assumed to flux poleward by sliding and depolymerization at the average sliding rate of the kMTs of the k-fiber.

Since the velocities of the KTs and the kMTs (i.e., the time-derivatives of their position  $\frac{dX_{KT}^R}{dt} = v_{chr}^R$ ,

$\frac{dX_{KT}^L}{dt} = v_{chr}^L$ ,  $\frac{dX_{kMT}^{R,i}}{dt} = v_{sliding}^{R,i}$  and  $\frac{dX_{kMT}^{L,i}}{dt} = v_{sliding}^{L,i}$ ), are determined by the forces acting on them at any

given time, the solution to the large set of coupled ODEs formed as described above yields the dynamics of the sister KTs and the kMTs over time. In this system of ODEs, the two equations for

the sister KTs are coupled through the cohesin forces proportional to  $(X_{KT}^R - X_{KT}^L)$ , while the equations for the left and right sister KTs' kMTs are coupled to one another and to the equations on the sister KTs via the forces exerted on their respective KT.

### 2.5.2.2. Sliding motor/Dynein/CenpE Force-Velocity Relationship and Force-Dependent Detachment Rates.

In both models considered here, similarly to (Civelekoglu-Scholey et al., 2006), we assume that the motor proteins (dynein, CENP-E and sliding motors, as it applies) have a linear force-velocity

relationship (Valentine et al., 2006), described by  $F(v) = F_{stall} (1 - \frac{v}{V_{sliding}^{max}})$ , where  $v$  is the time-

dependent velocity of the motor on its MT track. In addition, we assume that the motors detach

from the MTs in a force-dependent manner, described by  $k_{off}^{motor}(f) = k_{off}^{motor}(0) \exp(-\frac{f}{F_{det}^{motor}})$ , where

$k_{off}^{motor}(0)$  and  $F_{det}^{motor}$  are the detachment rate in the absence of load, and the force at which the detachment rate increases e-fold, respectively.

### 2.5.2.3. MT Plus and Minus End Dynamics.

As in (Civelekoglu-Scholey et al., 2006), we assume that the plus ends of kMTs undergo dynamic instability (DI), while the minus ends are depolymerized by the combined action of poleward sliding and depolymerization (Mitchison and Kirschner, 1984; Mitchison, 1989; Rogers et al., 2004). The DI of the MT plus ends is characterized by four parameters:  $v_g$ ,  $v_s$ ,  $f_{cat}$  and  $f_{res}$  (Verde et al., 1992).

We assume that the MTs' growth (polymerization) and shrinkage (depolymerization) rates are hindered by a factor  $k_{vg}$  and  $k_{vs}$  when the MT tip penetrates into the outer KT. The 'boundary/edge' position of the outer KT is defined differently in the motor-protein and non-motor linkage based models considered here. In the motor protein-based model, where dynein and CENP-E are

considered, the ‘edge’ of the KT is set at 0.2  $\mu\text{m}$  in the poleward direction (intra-KT distance) from the position of the inner KT-plate, and this intra-KT distance is constant over time. In the viscoelastic linkage-based model, where Ndc80 complexes provide the sole link between the KT and the MTs, the position of the outer KT ‘edge’ for each sister KT is defined as the current position of their most stretched Ndc80 complex’ attachment site to the kMT (Figure 2.4C). Among the DI rates, the catastrophe and rescue frequencies of the plus ends of MTs that are not attached to the KTs are defined by  $f_{cat}^0$  and  $f_{res}^0$ , respectively. For kMTs, however, these frequencies are assumed to be regulated differently in the two models considered here, and are explained below in each case.

#### **2.5.2.4. Polar ejection forces.**

Recent studies identified the distribution of the PEFs in PtK1 cells (Ke et al., 2009). Based on these studies, we assume a constant PEF from the spindle pole to a pre-defined point,  $x_d$ , within the half spindle, and a linearly decreasing function within the interval  $[-x_d, x_d]$ , as shown in Figure 2.6A (black line). Thus, the distribution of the PEFs in the models below, differs from our and others’ previous consideration (Civelekoglu-Scholey et al., 2006; Joglekar and Hunt, 2002).

#### **2.5.2.5. Numerical Solution Method and Algorithm.**

Here we outline the general methods of solution of the system of ODEs (typically composed of 52-102 equations) for both models, and further model specific details are described separately below. The large set of coupled ODEs obtained by writing the force-balance equations on the sister KTs and their kMTs are solved with a forward Euler algorithm as described in (Civelekoglu-Scholey et al., 2006) using custom-made MATLAB scripts. In the script, the initial conditions are as follows: sister KTs are positioned around the equator ( $x=0$ ), at rest length ( $d_0^{coh}$ ) away from one another.

The MT plus ends are randomly positioned near the KTs (using the built-in uniform pseudo-random

number generator in MATLAB, *rand*), all MT minus ends are positioned at the spindle poles. The polymerization/ depolymerization state of the MT plus ends are selected randomly (*rand*), and all motor proteins (sliding, CENP-E and dynein, as it applies) and non-motor linkages (Ndc80 complexes, as it applies) are initially ‘free’, not attached to MTs. In the new model, at  $t=t_0$ , all Ndc80 complexes (viscoelastic bonds) are at rest, with their pole-proximal end located at rest length ( $d_0^{Ndc}$ ) distance away from their KT. Thus, the system is at rest, no kMT or motor protein/Ndc80 complex is attached, hence all forces are equal to zero except for the PEFs (equal in magnitude, opposite in direction) at the current positions of the sister KTs.

Starting from these initial conditions (which differ slightly from one another at each realization due to the pseudo-random number generator used for the MT plus ends), at each time step  $t_n$  ( $t_{n+1} = t_n + \Delta t$ ) in the algorithm, we begin by executing the attachment/detachment event of each motor protein (and/or each Ndc80 complex) by computing the probability of its attachment/detachment kinetic under the current load. To this end, first, the attachment/detachment rates ( $k_{on}$  or  $k_{off}$ ) of the motor proteins/Ndc80 complexes are computed. If a kinetic rate is force-dependent, for example, for  $k = k_{off}(f)$ , the current rate is determined using the current force on the protein, via

$$k_{off}(f) = k_{off}^0 \exp\left(\frac{f}{F_{det}}\right), \text{ where } k_{off}^0 \text{ and } F_{det} \text{ are the detachment rate at zero load and the force at which}$$

detachment rate decreases e-fold, respectively (Figure S2.1A). Then, for each motor, the probability of detachment/attachment is computed using  $P = 1 - \exp(-k)$ , where  $k$  represents the appropriate kinetic rate. Next, a pseudo-random number,  $r$ , is selected for each motor using the MATLAB function *rand*. If  $r < P$ , the event (attachment/detachment) is realized, and the current state of the motor protein/Ndc80 complex is updated to ‘attached’ from ‘free’, or vice-versa. If  $r \geq P$  the state of the motor protein/Ndc80 complex is left unchanged. Once the attachment/ detachment events are

executed, the set of FB equations (algebraic) are solved using the updated number of attached motor proteins/Ndc80 complexes at the current time step, yielding the velocities of and forces exerted on the kMTs, motors and sister KTs. Next, the stochastic switch rate of each MT plus end is computed similarly to the attachment/detachment of motor protein/Ndc80 complex as described above. We assume that  $P = 1 - \exp(-f_{cat})$  [or  $P = 1 - \exp(-f_{res})$ ] is the probability of catastrophe (or rescue) of a MT plus end, and this probability is compared with a random number,  $r$ , as described above to execute the switch between growth and shrinkage state of each MT plus end. Finally, once the states of all MT plus ends are determined, the position of each sister KT is updated using its newly computed velocity  $v_{chr}$ , as  $X_{KT}^R(t_{n+1}) = X_{KT}^R(t_n) + v_{chr}^R \Delta t$ , whereas each MT plus end is moved poleward using its newly computed sliding rate  $v_{sliding}$ , and its newly computed polymerization/depolymerization state  $v_{poly/depoly}^{R,i}(t)$ , as  $X_{kMT}^{R,i}(t_{n+1}) = X_{kMT}^{R,i}(t_n) + v_{sliding}^{R,i} \Delta t + v_{poly/depoly}^{R,i}$ . Also, the force on each motor protein/Ndc80 complex is updated with the newly computed force, to be used for the stochastic kinetic computation in the next time step. The time step is incremented, and the sequence of events are repeated typically for thousands of time steps, equivalent to several hours in real time, to ensure stable behavior.

#### **2.5.2.6. Force Balance Model Adapted from the Model for Drosophila Embryo: Rescue and Catastrophe Frequency of kMT plus ends.**

In this model, the kMT plus end DI is the same as in (Civelekoglu-Scholey et al., 2006). Namely, we assume that depolymerases (kinesin-13) located at the KT alter the rescue frequency of kMTs in a tension-dependent manner. We assume that the depolymerase effectively acts on the plus ends of the MTs when tension is low, and its action is diminished with tension. The tension on the kMT is,  $F_{tension} = (\alpha F_{cohesin} + \beta F_{PE} + \gamma F_{KT}) / M$ , (see Figure 2.4A for forces), where  $M$  is the current number of attached MTs to the KT in consideration (left or right), and  $\alpha$ ,  $\beta$  and  $\gamma$  are non-

dimensionalization factors (units of  $\text{pN}^{-1}$ ). Then tension dependence of rescue frequency is defined

by:  $f_{res}(F_{tension}) = f_{res}^0 \exp(-\frac{F_{tension}}{F_{res}})$ , where  $f_{res}^0$  and  $F_{res}$  are the tension-free rescue frequency and

the tension force at which the effect of the KT-associated depolymerase decreases by e-fold,

respectively (Sprague et al., 2003). When the MT plus end contacts and begins impinging on the

KT plate, we assume that it stops growing (adding tubulin subunits to its plus end) and its

catastrophe frequency is increased by a factor of  $\varphi$  (i.e.  $f_{cat}^{impinge} = \frac{f_{cat}}{\varphi}$ ), and its rescue frequency

returns to low tension state  $f_{res}^0$ , regardless of the current tension on the KT, while it continues to

impinge on the KT plate.

#### **2.5.2.7. Force Balance Model for PtK1 cell chromosome dynamics: viscoelastic KT-MT linkages in the absence of KT-motors.**

The framework of this model is identical to the model above. However, the molecules responsible for forces on the KT and the kMT and their biophysical properties differ. Specifically, here we assume that force resulting from the opposing action of active CENP-E and dynein motors at the KT is of negligible magnitude during metaphase and we do not account for these forces. Instead, we assume that the non-motor viscoelastic linkages (Ndc80 complexes) provide the attachment of the sister KTs to spindle MTs, and the stretching/compression of these Ndc80 complexes resulting from the relative movement of a KT and the kMT each complex is attached to, exerts a force on the KT and the kMT (Figure S2.2A). The forces exerted on the KTs (and the kMTs) by attached viscoelastic Ndc80 complexes are described by an elastic spring constant  $\kappa_{Ndc80}$ , and a viscous friction coefficient  $\varepsilon_{Ndc80}$  (Figure 2.4C and Table S1). We assume that when a kMT plus end reaches a critical distance from the KT-plate, polymerization is hindered, and hence in this model we

neglect polymerization ratcheting forces which may result from kMT plus ends impinging on the KT-plate (i.e.  $F_{poly}=0$ ). Therefore, the equations for the KTs and the kMTs in (Civelekoglu-Scholey et al., 2006), are further revised by eliminating the motor generated forces and replacing them by the Ndc80 complex generated forces, and further by eliminating the polymerization ratcheting forces ( $F_{poly}=0$ , Figure 2.4D).

### 2.5.2.8. Force-dependent binding/detachment kinetics of Ndc80 complex.

In the model, we assume that the Ndc80 complexes exhibit the same attachment rates to, but different force-sensitive detachment rates from polymerizing and depolymerizing MT ends. The pseudo first order attachment rate  $k_{on}^{Ndc80}$  ( $s^{-1}$ ), is assumed to be independent of load, but the detachment rate  $k_{off}^{Ndc80}$  is assumed to be force dependent, and further assumed to be different for polymerizing and depolymerizing MTs in its functional form. The detachment rate of Ndc80 complex from polymerizing MTs is assumed to increase exponentially with force, and is defined by

$$k_{off,poly}^{Ndc80}(f) = k_{off,poly}^{Ndc80}(0) \exp\left(\frac{f}{F_{poly}^{Ndc}}\right),$$

where  $k_{off,poly}^{Ndc80}(0)$  is the detachment rate in the absence of load,

and  $F_{poly}^{Ndc}$  is the critical load force at which the rate increases e-fold (Figure S2.2B). The force-dependence of the detachment rate of Ndc80 complex from depolymerizing MTs, on the other hand, is assumed to have a biphasic shape: it initially decreases in response to force, then increases under

larger forces. In the model, it is described by  $k_{off,depoly}^{Ndc80}(f) = k_{off,depoly}^{Ndc80}(0) \exp\left(\frac{f}{F_{depoly}^{Ndc}}\right) \exp\left(\frac{f - F_{switch}}{F_{depoly}^{Ndc}}\right)$ ,

where  $k_{off,depoly}^{Ndc80}(0)$  is the detachment rate in the absence of load,  $F_{depoly}^{Ndc}$  is the critical load force at which the rate decreases e-fold, and  $F_{switch}$  is the load force typical of the turnaround in detachment rate (Figure S2.2C). This type of biphasic (catch-bond) behavior is typical of adhesion molecules

(Dembo et al., 1988; Evans, 2001), but not a characteristic property of MT-based motors, including kinesins and dynein (Coppin et al., 1997; Toba et al., 2006; Valentine et al., 2006).

### 2.5.2.9. MT plus and minus end dynamics.

We assume that MT plus end polymerization/growth rate is limited by the position of the KT and MTs cannot grow into or past the inner KT. We also assume that a KT-attached MT (a kMT) cannot depolymerize past the position of an attached Ndc80 complex, i.e. a tubulin dimer to which an Ndc80 complex is attached, cannot be dissociated from the lattice. Consequently, the depolymerization/shrinkage rate of each kMT is limited by the position of the attachment point of its Ndc80 complex closest to its KT. We assume that the rescue frequency of MT plus ends

depends on tension force,  $F$ , on the kMT, increasing with tension  $f_{res}(F) = f_{res}^0 \exp\left(\frac{F}{F_{res}}\right)$ , where

$f_{res}^0$  and  $F_{res}$  are the rescue rate in the absence of load, and the tension force at which rescue

frequency increases e-fold, respectively. The catastrophe frequency of a MT plus end is assumed to be dependent on its growth velocity, and on its length (effect of kinesin-8 motors, for example), increasing with decreasing growth rate and increasing length (Janson et al., 2003; Varga et al., 2006). For a MT of length  $l$ , growing at rate  $v$ , the catastrophe frequency is therefore defined by

$f_{cat}(l, v) = f_{cat}^0 \left(\frac{l}{L_{av}}\right) \exp\left(\frac{V_{free} - v}{V_g}\right)$ , where  $f_{cat}^0$  is the catastrophe frequency for ‘free’ growth rate

$(V_{free} = \frac{v_g}{k_{vg}})$ ,  $V_g$  is the critical growth rate at which the catastrophe frequency decreases e-fold,  $L_{av}$  is

the average MT length in the spindle and  $f_{cat}^0$  represents its catastrophe rate. For the plus ends of

the unattached MTs,  $V_{free} = v_g$  and the catastrophe frequency depends only on length

$$f_{cat}(l) = f_{cat}^0 \left( \frac{l}{L_{av}} \right).$$

#### 2.5.2.10. Polar ejection forces.

The PEF function is as described above. For the solutions shown in Figure 2.5, the linearly decreasing PEF function shown in black in Figure 2.6A was used, and for the solutions shown in Figure 2.6B-G the non-linear PEF function shown in red in Figure 2.6A was used. We propose that the PEF functions differ between the middle KT's and the peripheral KT's in two ways. First, PEFs have different baseline values (higher for the peripheral chromosomes) at positions proximal to the poles (Figure 2.6A). This difference in the baseline value is based on a simple and conservative approximation of the number of MTs nucleated at the pole that can potentially reach the chromosome arms as follows: assuming that the surface area of the chromosome arm can be approximated by an ellipse, with major axis length  $a_{middle}$  and  $a_{peripheral}$ , and same minor axis, the surface area of the peripheral and middle chromosome would obey,  $S_{peripheral} = (a_{middle} / a_{peripheral})^2 S_{middle}$ . We conservatively assume that  $a_{peripheral} = 3 a_{middle}$ . Further assuming that MT nucleation occurs only at the centrosomes equally in all directions, since the probability of MTs to encounter a chromosome arm is proportional to the surface area of the chromosome arm, this gives rise to the likelihood that a MT is  $3^2 = 9$  times more likely to reach the arm of a peripheral chromosome at a distance proximal to the pole, where the length-dependent catastrophe rate of the MTs have little effect on MT plus ends' distribution (see below), setting the baseline higher for the peripheral chromosomes. We propose that this is an underestimate, since there is also the additional 'crowding' effect for the middle sister KT's, where they become shielded by neighboring chromosomes (as discussed in the results). Second, the PEFs increase linearly around the equator

for the middle KT and non-linearly for the peripheral KTs (Figure 2.6A). For the middle chromosomes, it has been experimentally shown that PEFs increase in a sub-linear fashion around the equator (Ke et al., 2009), and for simplicity, here we assume a linear distribution. A length-dependent catastrophe frequency of MT plus ends would give rise to a highly non-linear distribution of MT plus ends at long distances,  $x$ , away from the poles, which is well described by

$$f_{PEF}(x) = \exp(-x \ln(x)) \text{ (Yadav and Mukherji, 2011).}$$

However, the experimental findings do not support such a non-linear increase in PEFs for excursion distances displayed by middle sister KTs, roughly ranging from  $R/2$  to  $3R/2$ , where  $R$  is the half spindle length (Ke et al., 2009), suggesting that the PEFs remain within the linear regime at this distance range. Nevertheless, due to the geometry of the spindle in these flat cells, the length of a MT impinging on the middle of a peripheral chromosome's arm (3 times the size of one in the middle of the spindle), is on average twice as long as one in the middle of the spindle (differs  $\sim$  by a factor of  $\left(\cos\left(\frac{\pi}{3}\right)\right)^{-1}$ ), at the same distance,  $x$ , away from the metaphase plate. Thus, here we propose that for the peripheral chromosomes' arms the PEF function enters the non-linear regime, reflecting a length-dependent catastrophe rate of the MT plus ends.

## ***2.6. Supplemental material.***

Supplemental material includes three figures (Figures S2.1-S2.3), one table (Table S2.1). Figure S2.1 illustrates the features of the model with motor-dependent KT-MT interactions and the behavior of sister KTs within such model. Figure S2.2 illustrates the forces exerted by Ndc80 complexes on a KT and its kMTs and the Ndc80 dissociation kinetics in the model based on non-motor, visco-elastic bonds. Figure S2.3 reports the model data for the distribution of the standard

deviations of the distances from the pole for middle and peripheral KTs. Table S2.1 is a comprehensive list of the parameters used in our mathematical model. Supplemental material can be found online at [http:](http://)

## **Acknowledgements**

We would like to thank all the members of the Cimini lab for useful discussion and helpful comments. We are also grateful to Tim Yen (Fox Chase Cancer Center, Philadelphia, PA) for providing the CENP-E antibody, Jennifer DeLuca (Colorado State University, Fort Collins, CO) for providing the HEC1-EGFP-N1 plasmid, and Duane Compton (Dartmouth Medical School, Hanover, NH) for providing the rabbit anti-Kif2a total serum. We finally thank Alex Mogilner, Ted Salmon, and Jianhua Xing for critical reading of the manuscript, and Rob Gunter for technical assistance. MS was a recipient of an ICTAS scholarship. This work was supported by NSF grant MCB-0842551 to DC and GCS. Additional funding was provided by HFSP grant RGY0069/2010 to DC.

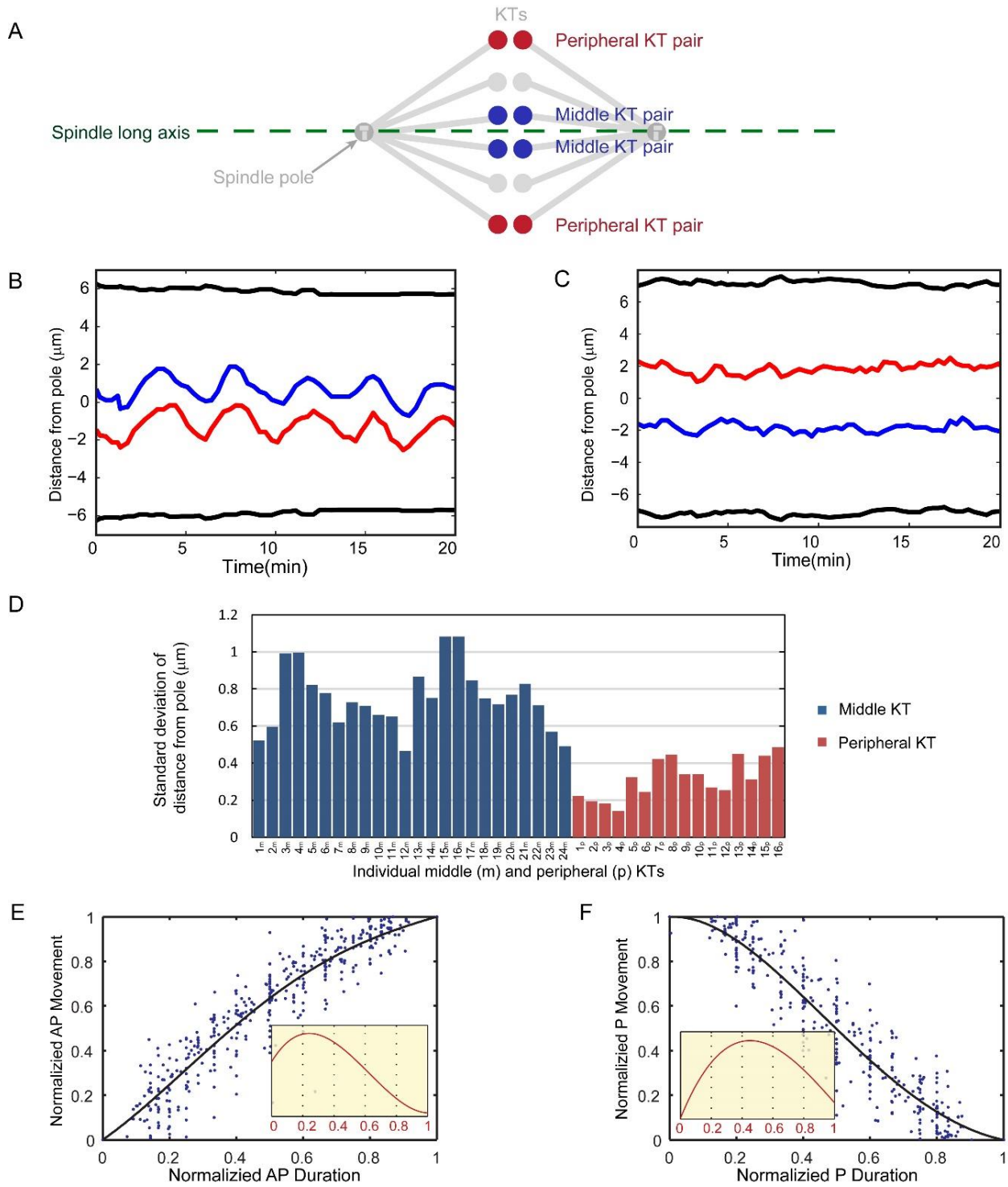


***Figure 2.1. Middle and peripheral sister KT pairs at the metaphase plate display significant differences in dynamics***

(A) Diagram illustrating how middle and peripheral KT pairs were defined with respect to the metaphase plate and the spindle long axis. In each cell analyzed, quantifications/measurements were performed for the two peripheral KT pairs (one on each side) and for two middle KT pairs, as illustrated in the diagram. (B and C) Representative examples of dynamics of middle (B) and peripheral (C) sister KT pairs in live metaphase PtK1 cells. (D) Distribution of the standard deviations of the distances from the pole for middle (blue) and peripheral (red) KTs. (E and F) Kinetic profiles of normalized P (F) and AP (E) movement for oscillating (middle) KTs. The solid lines through the kinetic data in E and F were obtained by fourth-degree polynomial fitting. The insets in E and F represent the normalized AP and P velocity kinetics obtained from the derivatives of the polynomial curves of AP and P movement, respectively. The data presented in this figure were obtained by analyzing 24 middle KT pairs and 16 peripheral KT pairs.

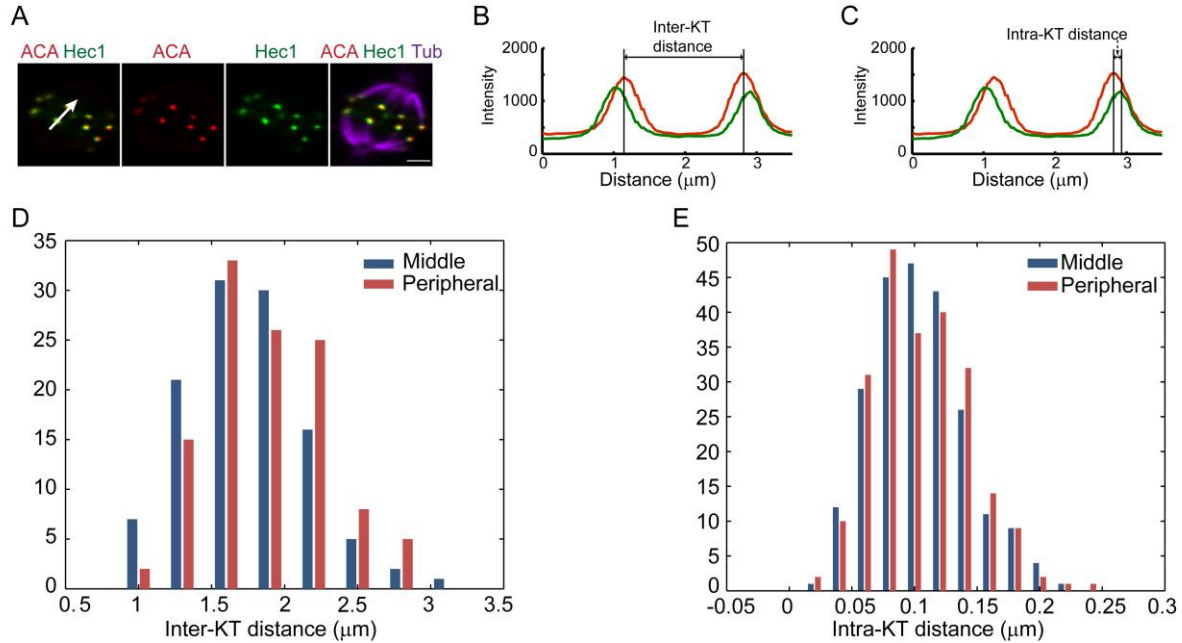


**Figure 2.2. Middle and peripheral KT pairs display similar inter- and intra-KT distances**

(A) Example of a metaphase PtK1 cell immunostained for  $\alpha$ -tubulin (purple), ACA (red), and Hec1 (green). The white arrow in A indicates the position and direction of the line scan for the fluorescence intensity profiles displayed in B and C. Bar, 5  $\mu\text{m}$ . (B and C) Fluorescence intensity profiles obtained from a line scan along the arrow traced in A. The inter- and intra-KT distances were obtained by measuring the distance between the ACA peaks (B) and the Hec1 and ACA peak (C), respectively. This method was used to measure the inter- and intra-KT distances in two pairs of middle sister KTs and two pairs of peripheral sister KTs in each of 57 cells. The data obtained from these measurements are reported in D and E. (D) Distribution of inter-KT distances in metaphase PtK1 cells ( $1.90 \pm 0.44 \mu\text{m}$  and  $2.01 \pm 0.40 \mu\text{m}$  for middle and peripheral sister KTs;  $n = 57$  cells). (E) Distribution of intra-KT distances in metaphase PtK1 cells ( $0.11 \pm 0.04 \mu\text{m}$  for both middle and peripheral sister KTs;  $n = 57$  cells).

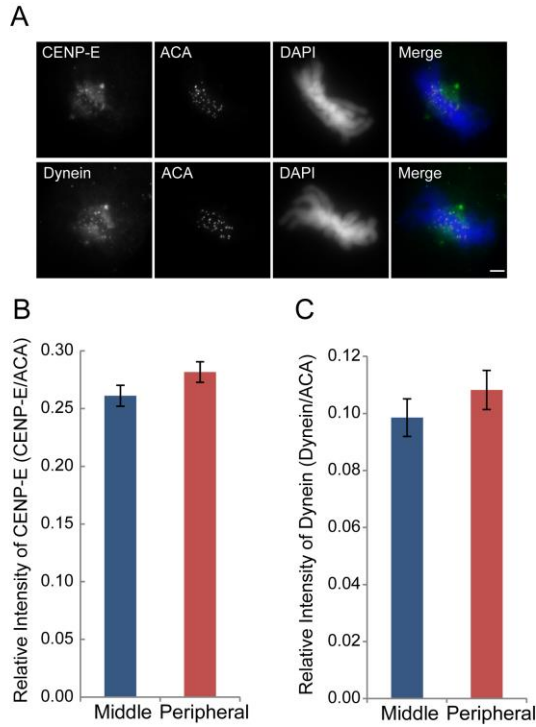
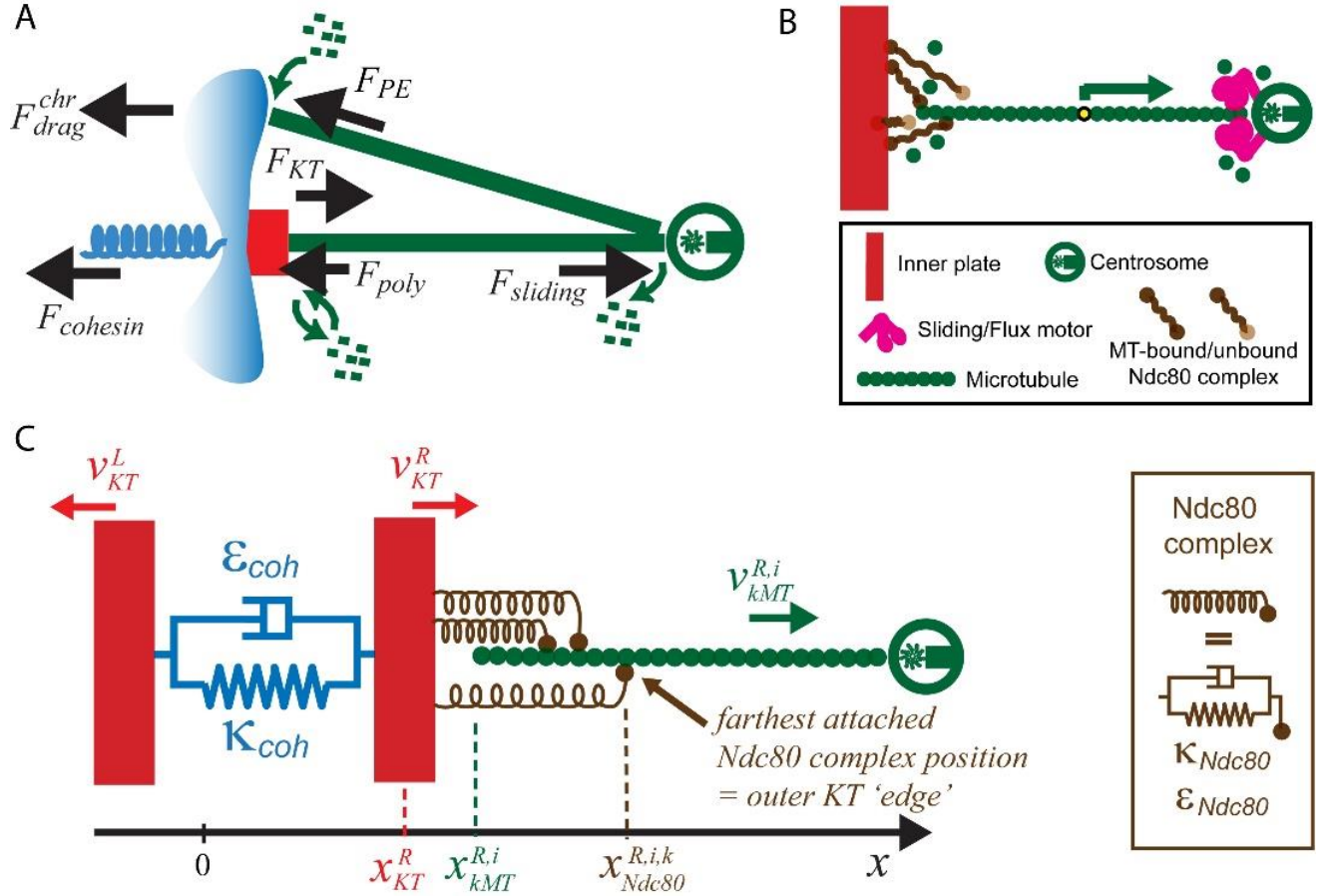


**Figure 2.3. Similar amounts of KT motors (CENP-E and dynein) accumulate at middle and peripheral KTs**

(A) Examples of metaphase PtK1 cells immunostained for CENP-E (top, first column) or dynein (bottom, first column) and ACA (second column). The chromosomes were stained with DAPI. In the merged images, DAPI is shown in blue, ACA in red, and the motors in green. Bar, 5  $\mu\text{m}$ . (B and C) Quantification of CENP-E (B) and dynein (C) at the KTs of middle versus peripheral KTs ( $n = 46$  cells) Error bars indicate mean  $\pm$  SEM.



**D**

**Model Equations:**

**Force-Balance equation for the (right) chromatid:**

$$F_{drag}^{chr} = F_{KT} - F_{poly} - F_{PE} - F_{cohesin}, \text{ where}$$

$$F_{drag}^{chr} = \mu_{chr} v_{chr}^R \text{ is the drag force on the chromatid; } F_{KT} = \sum_{\#kMT}^i \left( \sum_{\#Ndc80}^k F_{Ndc80}^{i,k} \right),$$

$F_{Ndc80}^{i,k} = \kappa_{Ndc80} \left( (x_{KT}^R - x_{Ndc80}^{R,i,k}) - d_0^{Ndc80} \right) - \epsilon_{Ndc80} (v_{chr}^R - v_{kMT}^{R,i})$  describe the forces exerted on the chromatid by the viscoelastic Ndc80 complexes attached to the (right) KT;  $F_{poly}$  is the polymerization ratcheting forces;  $F_{PE}$  is the PEFs; and  $F_{cohesin} = \kappa_{coh} \left( (x_{KT}^R - x_{KT}^L) - d_0^{coh} \right) - \epsilon_{coh} (v_{chr}^L + v_{chr}^R)$ , is the force exerted on the chromatid by the viscoelastic cohesin bonds between the sister chromosomes.

**Force-Balance on the  $i^{\text{th}}$  kMT attached to the (right) chromatid:**

$$0 \approx F_{drag}^{MT,i} = F_{sliding}^i - \sum_k^{\#Ndc80} F_{Ndc80}^{i,k}, \text{ where } F_{sliding}^i = N_{sliding}^i F_{sliding}^{stall} \left( 1 - \frac{v_{sliding}^{R,i}}{V_{sliding}^{max}} \right) \text{ is}$$

the force exerted on the  $i^{\text{th}}$  kMT, by  $N$  sliding motors.

***Figure 2.4. FB model description***

(A) Forces exerted on a (right) sister KT and a single kMT (note, each KT binds a bundle of kMTs, or k-fiber). (B) Close-up of the KT–MT interface and the viscoelastic Ndc80 complexes. (C) Mechanical properties of cohesin and Ndc80 complexes and positions of the kMT plus end, the KTs, and the Ndc80 bonds along the pole–pole axis. (D) Model equations.

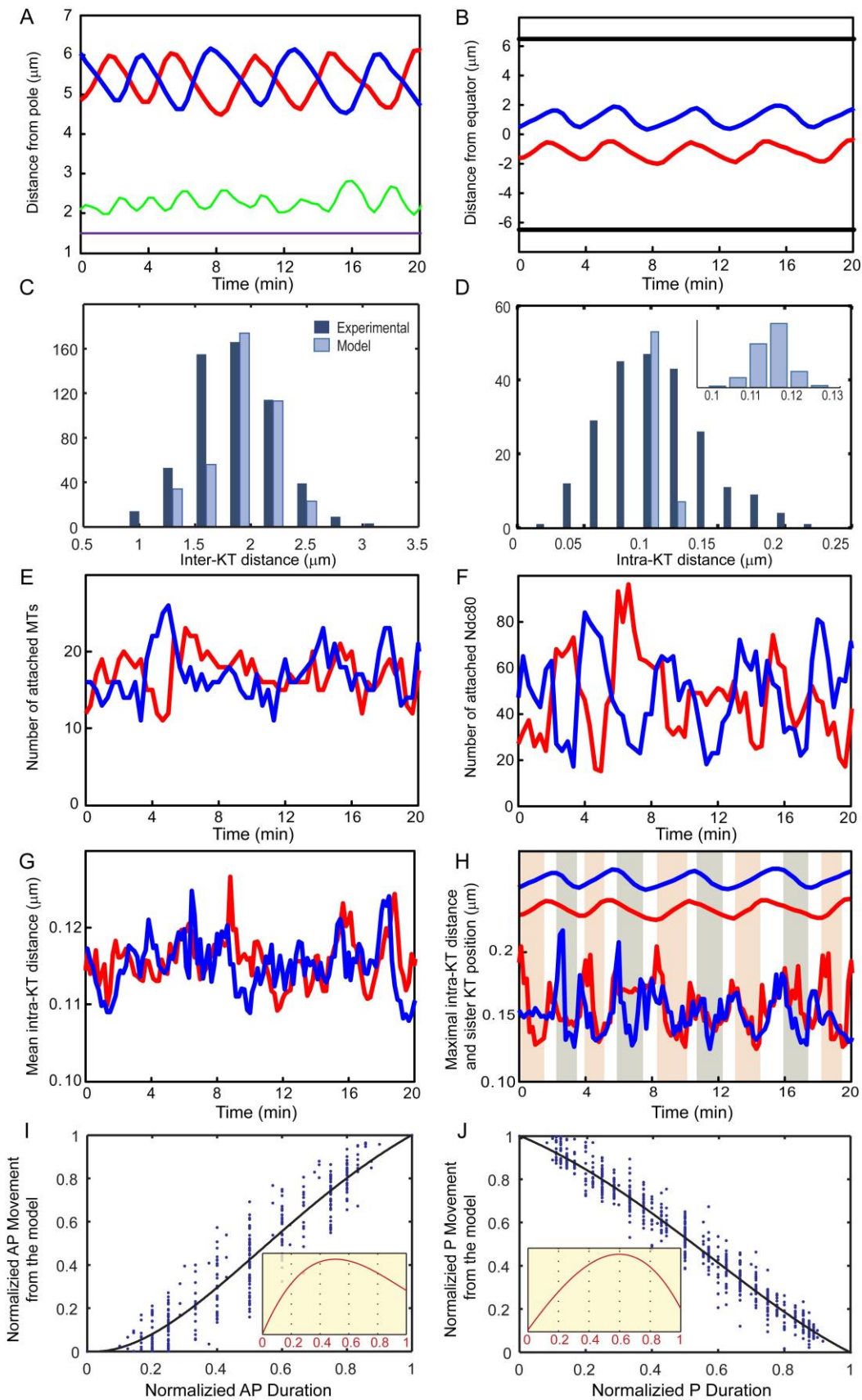


**Figure 2.5. A model based on dynamic viscoelastic KT–MT bonds reproduces the dynamic behavior of middle sister KT pairs**

(A) KT–pole (left KT, red; right KT, blue) and inter-KT (green) distances, and cohesin rest length (purple) over time. The periods of sister KT and inter-KT oscillations (by fast Fourier transform) are 280 s and ~5 min and 150 s and ~2.5 min, respectively (compare with Fig. 2.1 B). (B) Position of sister KTs (left KT in red, right KT in blue) and spindle poles (black) over time (the spindle equator is set to zero). (C and D) Inter- (C) and intra-KT (D) distances produced by the model ( $2.31 \pm 0.24 \mu\text{m}$  [ $n = 400$ ] and  $0.12 \pm 0.01 \mu\text{m}$  [ $n = 60$ ], respectively) shown side-by-side with the distance observed experimentally in live (inter-KT distances;  $n = 558$ ) or fixed (intra-KT distances;  $n = 228$ ) cells. Experimental data are shown in dark blue and model data are shown in light blue. The inset in D shows a close-up of the distribution of the data produced by the model. (E–H) Time evolution of the total number of attached MTs ( $17 \pm 4$  and 44% in depolymerization state; E), attached Ndc80 complexes ( $49 \pm 19$ ; F), and mean (G) and maximal (H) intra-KT distance of the left (red) and right (blue) sister KTs. In H, the maximum intra-KT distances and the corresponding sister KT positions for the left (red) and right (blue) sister KTs are shown over time. The gray and pink shaded areas mark the AP movement of the sister attached to the right and left pole, respectively. The AP-moving sister generally displays a higher intra-KT distance. (I and J) Kinetic profiles of normalized P (J) and AP (I) movement for oscillating KTs. The solid lines through the kinetic data in I and J were obtained by fourth-degree polynomial fitting. The insets in I and J represent the normalized AP and P velocity kinetics obtained from the derivatives of the polynomial curves of AP and P movement, respectively. Note, the slight differences between the model and the experimental results (I and J vs. Fig. 2.1, E and F, insets) can be explained by the fact that the time of the P-AP switch can be tracked with high precision in the model, but not in the experiments. This would account for the

delay in the normalized time for reaching maximal velocity for both the AP- and P-moving sister  
KTs in the model results.

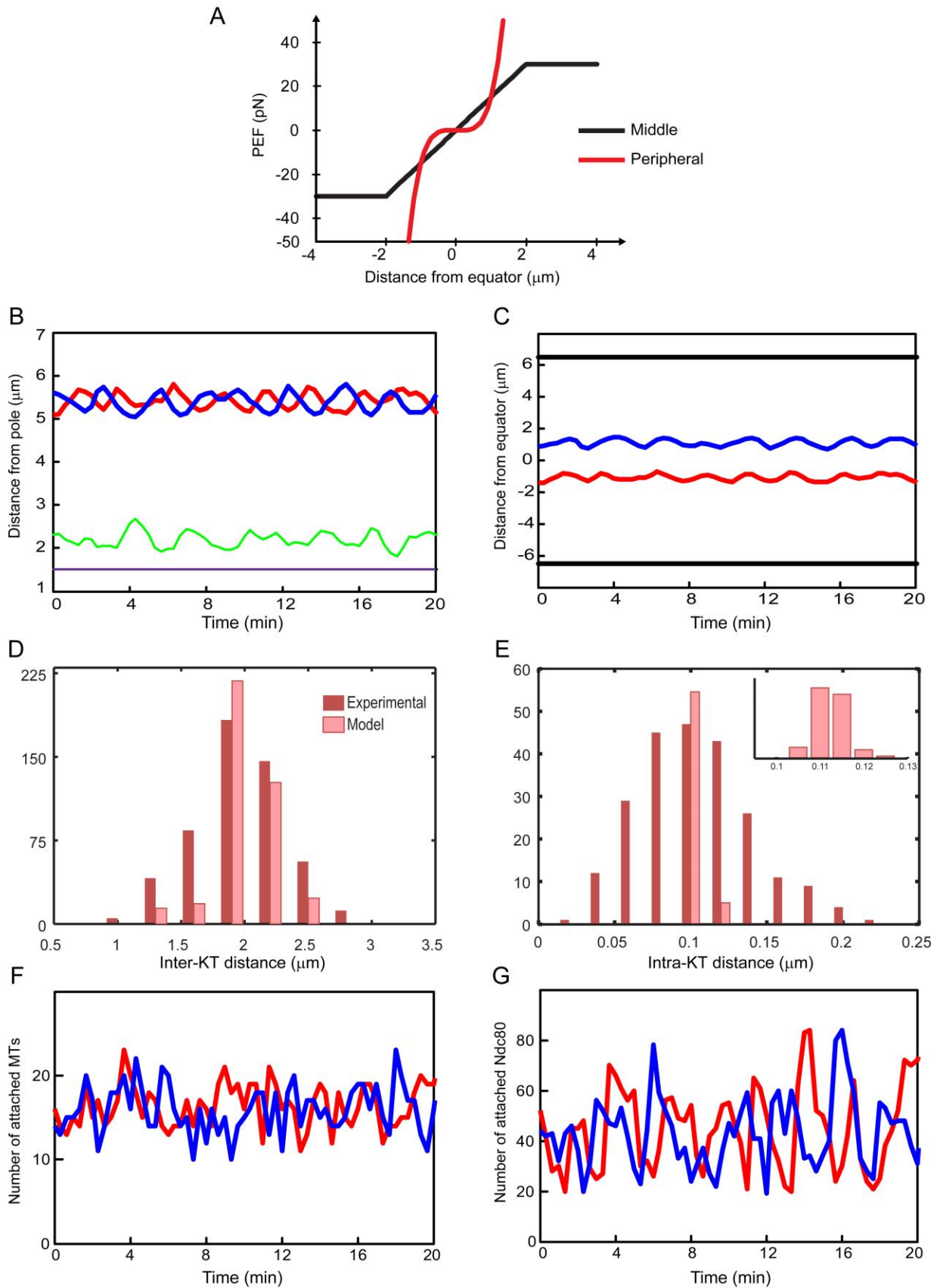


***Figure 2.6. A nonlinear distribution of PEFs can suppress the oscillations of peripheral sister KT pairs***

(A) Distribution of PEFs in the spindle: for KT pairs in the middle of the spindle, the PEFs initially decrease linearly away from the equator then stay constant toward the poles (black line). In contrast, for KT pairs at the periphery of the spindle, the PEFs are very low near the equator, then increase sharply (nonlinear) to high levels (red line). See Materials and methods for additional quantitative details. (B) KT–pole (left KT, red; right KT, blue) and inter-KT distance (green), and cohesin rest length (purple) over time. Note the erratic dynamic behavior. (C) Position of sister KTs (left KT in red, right KT in blue) and spindle poles (black) over time, compare with Fig. 2.1 B. (D and E) Inter-KT (D) and intra-KT (E) distances produced by the model ( $2.22 \pm 0.16 \mu\text{m}$  [ $n = 400$ ] and  $0.12 \pm 0.01 \mu\text{m}$  [ $n = 60$ ], respectively) shown side-by-side with the distances observed experimentally in live (inter-KT distances,  $n = 530$ ) or fixed (intra-KT distances,  $n = 228$ ) cells. Experimental data are shown in dark red and model data are shown in light red. The inset in E shows a close-up of the distribution of the data produced by the model. (F and G) Time evolution of the total number of attached MTs ( $16 \pm 3$  and 42% in depolymerization state; F) and the total number of attached Ndc80 complexes ( $44 \pm 16$ ; G) for the left (red) and right (blue) sister KTs.

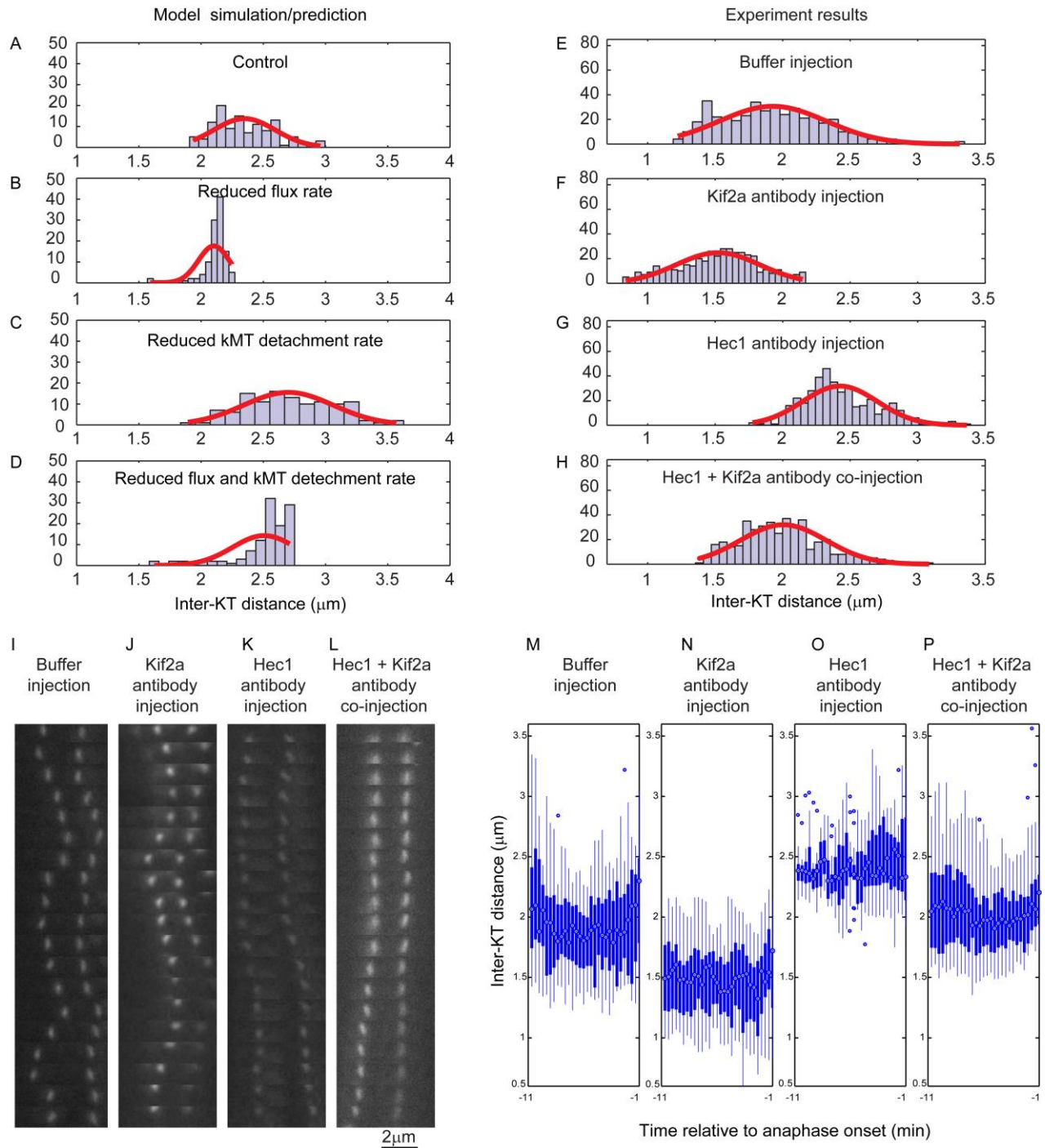


**Figure 2.7. Inter-KT hyperstretching caused by reduced kMT detachment rates can be rescued by simultaneous reduction of MT poleward flux**

(A–D) Model simulation results of the distribution of inter-KT distances under different conditions ( $n = 4$  KT pairs in all cases). (E–H) Experimentally determined distribution of the inter-KT distances under different conditions. Reduction of MT poleward flux was achieved by

microinjection of anti-Kif2a antibodies (F,  $n = 12$  KT pairs); reduction of kMT detachment rate was achieved by microinjection of anti-Hec1 antibodies (G,  $n = 7$  KT pairs); simultaneous reduction of MT poleward flux and kMT detachment rate was achieved by coinjection of the two antibodies (H,  $n = 12$  KT pairs); HEK buffer injection (E,  $n = 8$  KT pairs) was used as a control. (I–L) Time series of 19 frames (acquired at 20-s intervals) displaying individual KT pairs from videos of HEC1-GFP PtK1 cells microinjected as indicated in the figure labels. The last frame in each series represents anaphase onset. (M–P) Box plots of inter-KT distances in cells microinjected as indicated in the figure labels. Each dot in the graphs represents the median value of inter-KT distances obtained for different KT pairs ( $n = 8, 12, 7,$  and  $12$  KT pairs for M, N, O, and P, respectively) from 4–7 cells at the same time point; the boxes represent the 25th–75th percentile range; the whiskers extend to the most extreme data points not considered outliers. All the graphs display data for a 10-min interval preceding anaphase (up to 1 min before anaphase onset).

**Table 2.1. Model assumptions**

---

**A. Core assumptions**

- KTs attach to MTs through dynamic, viscoelastic, non-motor linkages (Ndc80 complexes).
  - When bound to a MT, each extended/compressed Ndc80 complex exerts a force (e.g., poleward/anti-poleward) on its KT, and reciprocally to the MT to which it is bound.
  - Ndc80 complexes bind to and detach from MTs independently from one another.
  - Cohesin bonds between sister KTs behave as viscoelastic material.
  - Both KT-bound and free MT plus-ends undergo dynamic instability.
  - A polymerizing MT plus end stalls when it reaches the inner KT.
  - MT-minus ends slide polewards by sliding/flux motors and depolymerize at the rate the MTs are slid into the poles.
- 

**B. Added assumptions**

- Ndc80 complexes have different detachment kinetics for polymerizing/depolymerizing (GTP/GDP-tubulin) tips of MTs.
  - Ndc80 complexes behave as tension sensors (force-dependent kinetics).
  - MT plus end *catastrophe rate is length dependent*.
  - KT-bound MT plus-end catastrophe rate is growth rate-dependent (increases with decreasing growth rate).
  - KT-bound MT plus-end rescue rate is regulated by tension forces exerted on it by the Ndc80 complexes (increased rescue under high tension).
- 

**C. Assumptions vital for model's robustness**

- A MT plus end cannot depolymerize past an Ndc80 complex attachment position.
  - Detachment of Ndc80 complex from polymerizing and depolymerizing MTs differs, both in the absence and the presence of tension force.
  - Ndc80 complex binds 'weakly' to polymerizing and, in a biphasic way, 'strongly' to depolymerizing MTs under moderate force.
-

**Table 2.2. Model test for suppression of KT oscillations**

<b>Tested Condition</b>	<b>Suppression of KT Oscillations</b>	<b>Additional Observed Changes</b>
higher kMT # per KT	NO	increased inter-KT distance and oscillation amplitude
angular projection of sliding force (45°)	NO	increased inter-KT distance
higher chromosome viscous drag coefficient	NO	decreased oscillation amplitude and period
higher/lower $f_{cat}$	NO/NO	increased/decreased oscillation amplitude and period
higher/lower PEF (linear)	YES	significantly reduced/increased inter-KT distance
sharply increasing PEF (non-linear)	YES	None

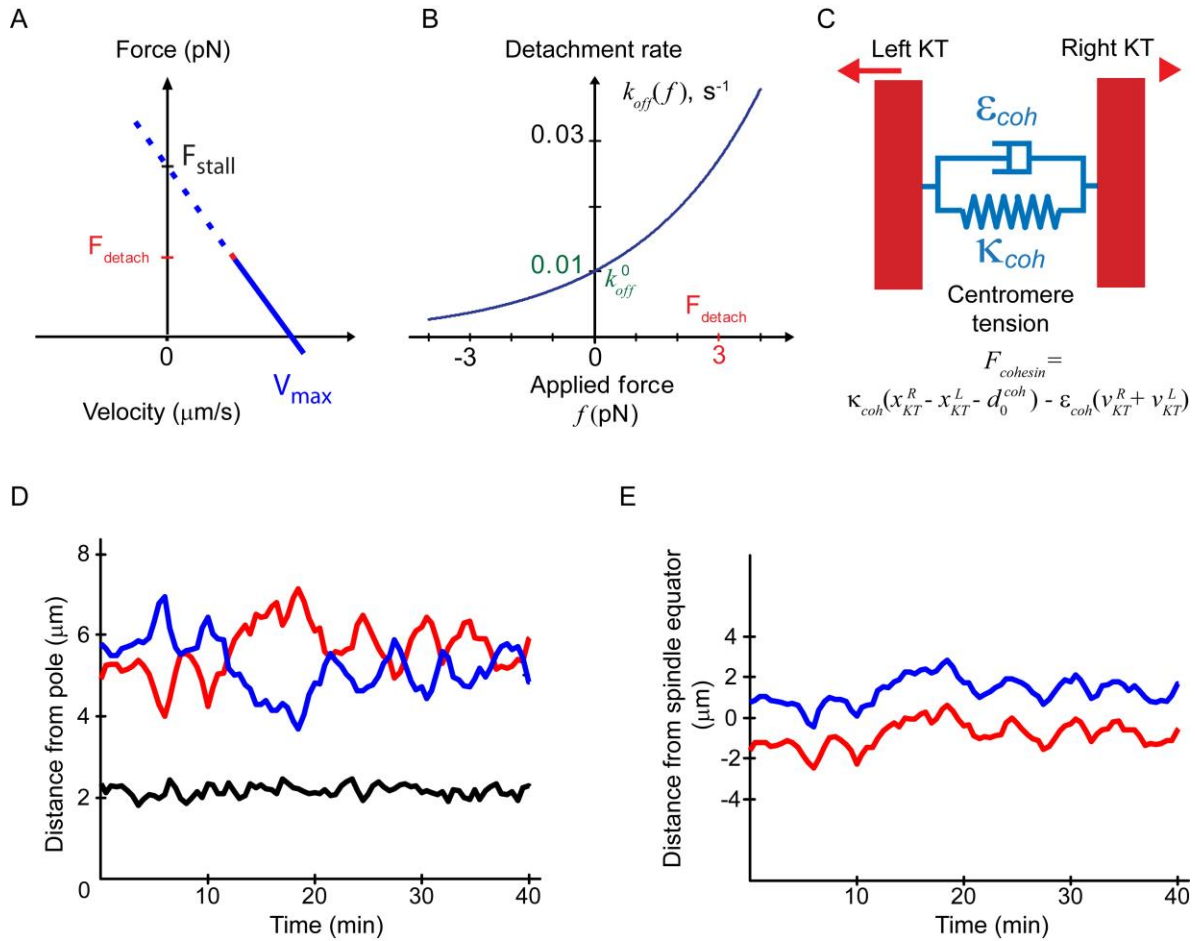


**Figure S2.1.** Biophysical properties of motors, non-motor proteins and behavior of sister KTs in the model with motor-dependent KT-MT interactions. (A) Typical form of the motor protein force-velocity relationship. (B) Force-sensitive dissociation rate of motors and non-motor proteins. (C) Description of the tension force exerted on the KTs by viscoelastic cohesin bonds. (D) Distance of a pair of middle sister KTs (left KT in red, right KT in blue) from the spindle pole and inter-KT distance (black) over time. (E) Distance of sister KTs (same pair shown in D) from spindle equator, over time.

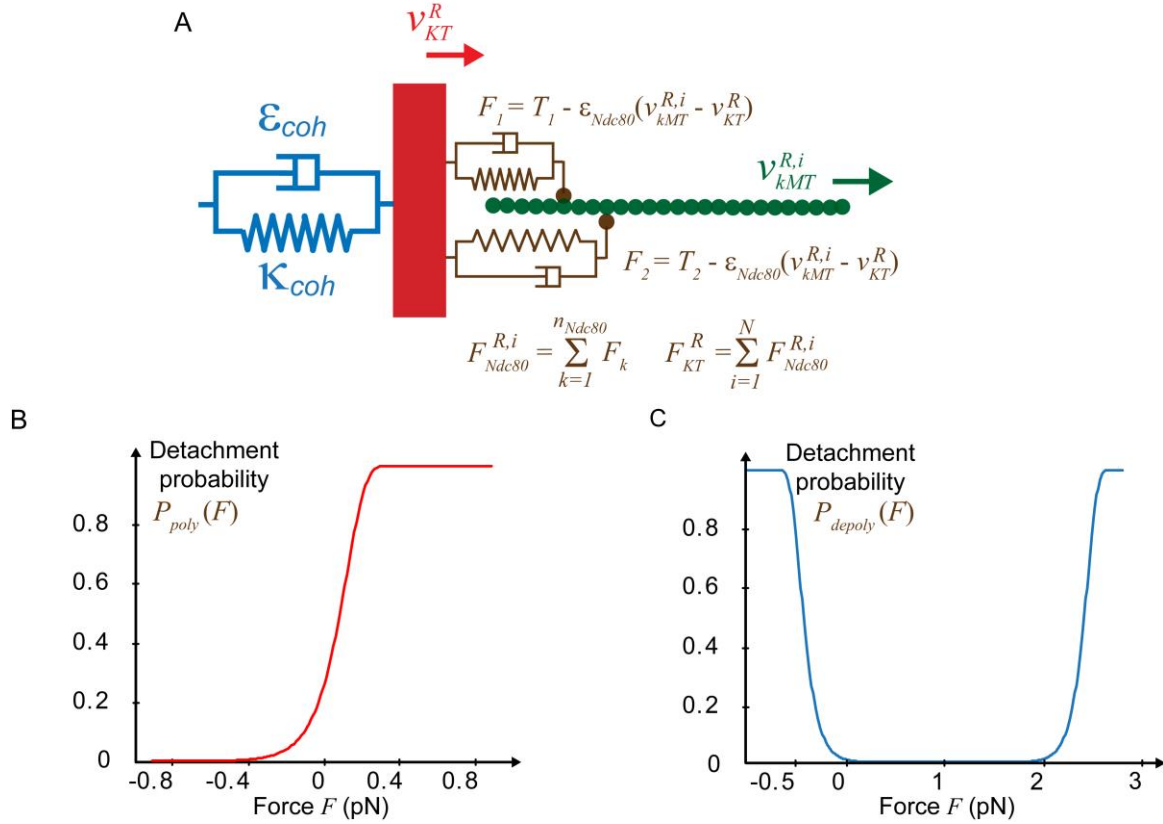


**Figure S2.2.** Tension forces exerted on the KT and the kMTs by MT bound Ndc80 complexes and force-sensitive dissociation kinetics of the Ndc80 complex. (A) Total tension force exerted by multiple bound Ndc80 complexes (brown mechanical elements) on the KT (red bar) and the kMT (green rod). Only a single right KT attached MT is depicted for simplicity. The cohesin between the sister KTs is shown (blue mechanical element), but the left KT is not depicted. (B) Ndc80 complex dissociation rate from polymerizing MTs increases with increased load. (C) Ndc80 complex dissociation rate from depolymerizing MTs is biphasic: it initially decreases with increasing load (near zero), then increases with further increased load.

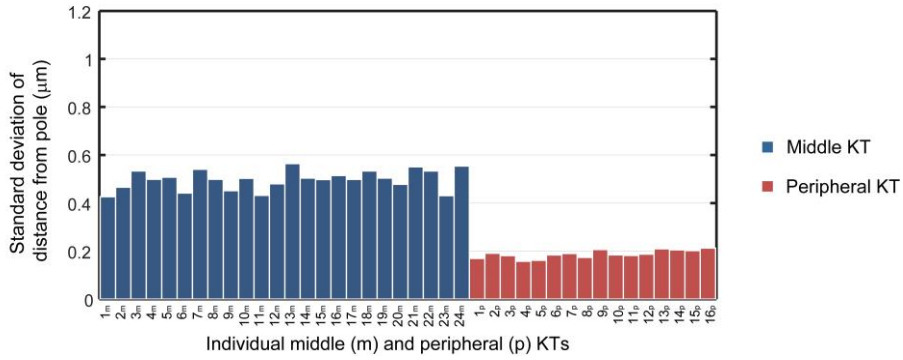


**Figure S2.3.** *Distribution of the standard deviations of the distances from the pole for middle (blue) and peripheral (red) KTs produced by the model.* Note, both the actual values and the variability of the standard deviations are smaller compared to the experimental data (Figure 1D) due to the higher accuracy of the simulation data. However, the mean inter-KT distances (Figure 5C) do not differ between experimental and modeling data.

## **Chapter 3. Metaphase and anaphase chromosome dynamics in cells with normal versus merotelic KT attachment and role of MT poleward flux in correction of merotelic attachment**

Bin He<sup>1</sup>, Emanuele Roscioli<sup>1</sup>, Alex Winemiller<sup>1</sup>, Heather Bomberger<sup>1</sup>, Gul Civelekoglu-Scholey<sup>2\*</sup>, and Daniela Cimini<sup>1\*</sup>

<sup>1</sup> Department of Biological Sciences and Virginia Bioinformatics Institute, Virginia Tech, Blacksburg, VA, 24061 – USA

<sup>2</sup> Department of Molecular and Cellular Biology, University of California, Davis, CA 95616 – USA

\*Corresponding authors

Manuscript in preparation

### **Author contributions**

Conceived and designed the experiments: BH, ER, GCS, and DC. Performed experiments and collected experimental data: BH, ER, and DC. Analyzed the data: BH, AW and HB.

Refined the mathematical model, performed computer simulations, and analyzed simulation data: GCS. Contributed reagents/materials/analysis tools: GCS and DC. Prepared the manuscript: BH, GCS, and DC.

### **3.1. Abstract**

The establishment and maintenance of correct KT-MT Correct chromosome segregation during mitosis relies on the mitotic apparatus, a complex macromolecular machine that specifically assembles during this cell cycle stage. We previously established a quantitative model to describe metaphase chromosome dynamics via MT-MT interactions mediated by viscoelastic linkages (Civelekoglu-Scholey et al., 2013). Here, we used this quantitative framework in combination with experimental approaches to characterize the metaphase and anaphase KT/chromosome dynamics in cells with merotelic KT attachments. Moreover, we investigated the role of Kif2a in correction of KT mis-attachments in PtK1 cells. We found that merotelic attachment not only diminishes the oscillation of the merotelically attached KT, but also alters the oscillation behavior of its normally attached sister KT in metaphase. Moreover, we found that a single merotelically attached KT could reduce the poleward movement rate of all other normally attached KTs in the same cell. Finally, we found that Kif2a inhibition reduced MT poleward flux and induced high rates of anaphase LCs, suggestive of reduced ability to correct KT-MT mis-attachments. This finding supports the model prediction that reduced MT poleward flux results in larger numbers of kMTs.

### **3.2. Introduction**

The establishment and maintenance of correct KT-MT attachment and chromosome positioning depend on the interplay between opposing forces controlled by regulatory molecules and spindle mechanics. As described in Chapter 2, we previously developed a quantitative framework integrating forces that control the positioning of amphitelically attached KT pairs during metaphase (Civelekoglu-Scholey et al., 2013) . The model describes and predicts many aspects of spindle dynamics. The next step we took was to extend this model and utilize the refined model to address

important biological questions. First, we investigated the metaphase chromosome dynamics associated with erroneous KT-MT attachment, specifically merotelic attachment. Erroneous KT-MT attachment arises frequently in healthy mitotic cells due to the stochastic nature of establishment of KT-MT attachments (Cimini et al., 2003), but most of these erroneous attachments are corrected before anaphase onset. This correction process depends upon microtubule dynamics fine-tuned by many mechanical and molecular signaling mechanisms, some of which have been extensively dissected and others that are not well understood. MT poleward flux is one such mechanism because, although there is evidence for a role of MT poleward flux in correction of KT mis-attachments (Ganem et al., 2005), the mechanism by which it does so is not clear. By combining our quantitative model with specifically-designed experiments, we dissected this problem, gaining new insight. We next investigated the dynamics of anaphase KTs. Anaphase is the phase during which the two sets of chromosomes move to opposing spindle poles of the elongating spindle. During this phase, the two sets of chromosomes must move sufficiently apart towards opposite spindle poles, so that they do not interfere with the abscission process at the spindle midzone. A key driver of this poleward chromosome movement is a pulling force coupled to K-fiber shortening. The shortening of K-fibers occurs as a result of kMT depolymerization, which in anaphase PtK1 cells appears to occur mostly at the plus end (Zhai et al., 1995). Previous studies have shown that anaphase cells with merotelically attached lagging chromosomes display slower rates of spindle elongation (anaphase B) compared to cells with normal chromosome segregation (Cimini et al., 2004), suggesting that merotelic KTs may affect overall spindle dynamics. Here, we investigated this possibility by quantitatively characterizing the KT/kMT dynamics in live cells with and without merotelically attached anaphase lagging chromosomes.

### **3.3. Results and Discussion**

#### **3.3.1. Metaphase dynamics of merotelic KTs**

The dynamics of sister KTs are closely coupled via a viscoelastic bond (Civelekoglu-Scholey et al., 2013; Dumont et al., 2012; Wan et al., 2012). However, previous observations suggested that merotelic KTs do not oscillate, whereas the normally attached sister of the merotelic KT continues to oscillate (Cimini et al., 2004) (Figure 3.1A). Our quantitative model can reproduce such behavior (Figure 3.1B), but predicts that the normally attached sister of a merotelic KT (Sister of merotelic) displays reduced oscillations. To test this prediction and further validate our mathematical model, we quantified the oscillation period of four sisters of merotelic KTs and compared it to previously reported oscillation period for amphitelic KTs (Wan et al., 2012). We found that the oscillation period for sisters of merotelic KTs was  $2.5 \pm 0.314$  min compared to 3.71 min reported for normal amphitelic KTs (Wan et al., 2012). Thus, merotelic KT attachment not only suppresses the oscillations of the merotelic KT itself, but also reduces the oscillations of its normally attached sister.

#### **3.3.2. Role of MT poleward flux in correction of KT mis-attachments**

In our mathematical model, MT poleward flux results from minus end depolymerization and poleward translocation of K-fibers (Civelekoglu-Scholey et al., 2013) and produces forces that are transduced to the KT and contribute to KT/chromosome oscillations about the metaphase plate. Thus, using our mathematical model, we could make predictions on how suppression of flux may affect the dynamics of kMTs and hence the correction of KT mis-attachments. Our model predicted that reduced MT poleward flux results in increased numbers of kMTs bound to individual

amphitelic KTs, with an average of 28 MTs in cells with reduced MT poleward flux compared to an average of 17 MTs bound to amphitelic KTs in cells with normal poleward flux. This increase in bound MTs can be explained by a decrease in turnover of kMTs, which is known to result in faulty correction of mis-attachments, particularly merotelic (Bakhoun et al., 2009b; Cimini et al., 2006). To experimentally suppress MT poleward flux, we injected cells with anti-Kif2a antibodies (Civelekoglu-Scholey et al., 2013). Kif2a is a MT depolymerizing kinesin 13 specifically enriched at the spindle poles from prometaphase through anaphase (Ganem et al., 2005) and is required for poleward flux in human cells (Ganem et al., 2005) and *Xenopus* extracts (Gaetz and Kapoor, 2004). In buffer-injected PtK1 cells in metaphase, we found a kMT poleward flux rate of  $0.74 \pm 0.28$   $\mu\text{m}/\text{min}$  ( $n = 8$ ), consistent with previous studies (Cameron et al., 2006). Injection of anti-Kif2a antibodies reduced the poleward flux rate to  $0.49 \pm 0.21$   $\mu\text{m}/\text{min}$  ( $n = 8$ ) (Civelekoglu-Scholey et al., 2013) (Figure 3.2A), thus making this experimental approach suitable for investigating the mechanism by which MT poleward flux may contribute to correction of KT mis-attachments.

To test the prediction that reduced MT poleward flux affects correction of merotelic KT attachments, we examined chromosome segregation in Hec1-GFP PtK1 cells (Figure 3.2B) microinjected with anti-Kif2a antibodies after bipolar spindle formation and found a dramatic increase in the number of cells exhibiting anaphase lagging chromosomes (Figure 3.2C). Anaphase lagging chromosomes are known to be merotelically attached (Cimini et al., 2001), which also seems to be the case for the lagging chromosomes of anti-Kif2a antibody-injected cells, whose KTs display a stretched appearance (Figure 3.2B). Injection of anti-Hec1 antibodies in PtK1 cells was previously shown to dramatically decrease kMT turnover and hence prevent correction of merotelic attachments, which resulted in high rates of anaphase lagging chromosomes (DeLuca et al., 2006). Similarly to this previous study, we found high rates of anaphase lagging chromosomes in cells

microinjected with anti-Hec1 antibodies (Figure 3.2C). However, co-injection of anti-Hec1 and anti-Kif2a antibodies increased the rate of anaphase lagging chromosomes only slightly above the rates observed in cells microinjected with anti-Kif2a antibody alone (Figure 3.2C), indicating that Kif2a, and presumably MT poleward flux, plays a major role in correction of KT mis-attachments.

To assess how Kif2a inhibition affected the turnover of kMTs, we performed FDAP (Fluorescence Dissipation After Photoactivation) experiments in PtK1 cells expressing PAGFP-tubulin (Figure 3.3). We found that the fraction of MTs bound to KTs was increased in anti-Kif2a-injected cells (Figure 3.3B), confirming the model predictions that larger numbers of MTs are bound to KTs in conditions of reduced flux. However, to our surprise, the  $t_{1/2}$  for kMTs was shorter in anti-Kif2a-injected vs. buffer-injected cells (Figure 3.3B). The parameters identified in these FDAP experiments will be used to refine the model and make new predictions that can explain higher numbers of kMTs, but reduced turnover rates. Despite the puzzling results in our FDAP experiments, overall our results support the idea that reduced MT poleward flux results in larger numbers of kMTs, impaired correction of KT mis-attachments, and chromosome mis-segregation in the form of anaphase lagging chromosomes.

### **3.3.3. Anaphase KT/chromosome dynamics**

As a further step toward building an integrated model of chromosome dynamics from metaphase through anaphase in PtK1 cells, we next focused on the dynamics of anaphase chromosome segregation and the relationship between dynamics of the mitotic apparatus and chromosome segregation errors.

The most prominent mechanical change between metaphase and the beginning of anaphase is the degradation of the cohesin proteins holding the sister chromatids together. In our mathematical

model, these proteins are represented by viscoelastic bonds linking the sister KTs (Civelekoglu-Scholey et al., 2013). In metaphase, tension on these viscoelastic bonds regulates turnover and polymerization/depolymerization rates of kMTs, and thus the length of the K-fiber. In model simulations, releasing the cohesin bonds between the sister chromatids and suppressing PEFs promotes kMT depolymerization and persistent poleward chromosome movement at a rate of 1.1  $\mu\text{m}/\text{min}$  (Figure 3.4A). To obtain experimental data on rates of anaphase KT poleward movement, we imaged PtK1 cells expressing HEC1-GFP protein as they progressed through anaphase and measured an average rate of  $0.43 \pm 0.24 \mu\text{m}/\text{min}$  during the first 5min after anaphase onset (Figure 3.4 B). Thus, the rate of poleward movement in PtK1 cells is slower than predicted by the mathematical model. However, this new information will allow us to further refine the model and address future questions.

Quantification of our experimental data showed that chromosome poleward movement in anaphase was complete within the first 5 min (Figure 3.5A), after which chromosomes further move apart through spindle elongation (anaphase B). We found that in cells with anaphase lagging chromosomes the initial phase of fast poleward chromosome movement was slowed down for most chromosomes in the spindle (Figure 3.5B). This suggests that the presence of a merotelic attachment may interfere with overall spindle dynamics and cause a global change in the poleward movement rate of all chromosomes in the spindle.

To test this hypothesis, we analyzed anaphase poleward movement of 166 normally attached KTs in normal cells without merotelic attachments and 73 normally attached KTs in cells with merotelically attached lagging chromosomes. As expected, we found that poleward movement of normally attached chromosomes was significantly slower in anaphase cells with merotelically attached lagging chromosomes compared to cells without lagging chromosomes (Figure 3.5C). This

is a striking observation suggesting a possible interplay between KT attachment state and overall dynamics of the mitotic apparatus.

### **3.3.4. How does kif2a inhibition affect anaphase chromosome dynamics**

As shown in Figure 3.2 and Chapter 2, Kif2a contributes to the maintenance of a proper MT poleward flux rate and inter-KT tension at metaphase, thus regulating mis-attachment correction. We then asked whether Kif2a played any role in controlling anaphase chromosome dynamics, which could be an additional mechanism explaining the observed increase in anaphase lagging chromosomes.

To address this question, we measured the anaphase chromosome poleward movement rate in anti-Kif2a-injected HEC1-GFP PtK1 cells. Because injection of Kif2a causes high rates of anaphase lagging chromosomes (Figure 3.2C) and because we found the presence of anaphase lagging chromosomes to impact the dynamics of the whole anaphase spindle (Figure 3.5), we grouped the anti-Kif2a injected cells into two separate categories: with and without lagging (Figure 3.6). Consistent with our previous finding (Figure 3.5), cells with lagging chromosomes displayed slower rates of chromosome poleward movement compared to buffer-injected cells. However, the rate of poleward movement in anti-Kif2a-injected cells without lagging chromosomes did not differ from the rate of poleward movement in buffer-injected cells (Figure 3.6 Green and Blue), although the initial KT-pole distance was larger in anti-Kif2a-injected cells because anti-Kif2a injection induces lengthening of the metaphase spindle (data not shown). The fact that inhibiting Kif2a does not affect the k-fiber shortening rate is not surprising given that MT poleward flux is not expected to play a

major role in anaphase. Indeed, in both LLC-PK (pig kidney epithelial) and PtK1 cells, flux was shown to diminish abruptly at the metaphase-anaphase transition (Zhai et al., 1995) and K-fiber shortening is believed to depend mainly on MT plus end depolymerization at the KT-MT interface. Thus, our results show that anaphase lagging chromosomes are not caused by impaired anaphase chromosome dynamics and further support the idea that the increased rates of anaphase lagging chromosomes in Kif2a-inhibited cells are the result of impaired correction of merotelic KT attachments.

### **3.4. Materials and Methods**

#### **3.4.1. Cell culture.**

PtK1, HEC1-GFP PtK1, and PAGFP-tubulin PtK1 cells were cultured in HAM's F-12 media (Invitrogen) supplemented with 5% Sodium Pyruvate (Invitrogen), 1% antibiotic-antimycotic (Invitrogen), and 10% fetal bovine serum (Invitrogen), and maintained at 37°C in a humidified CO<sub>2</sub> incubator. For experiments, cells were grown on sterilized acid-washed coverslips inside 35 mm Petri dishes for 48 hours before observation.

#### **3.4.2. Microinjection.**

Kif2a and HEC1 antibody microinjection was performed as previously described (Civelekoglu-Scholey et al., 2013). In brief, Kif2a antibodies were purified by IgG affinity purification (Nab Spin Kit, Thermo Scientific) from rabbit anti-Kif2a total serum (generous gift of Dr. Duane Compton, Dartmouth Medical School). For microinjection, both Kif2a and Hec1 9G3 (Abcam) antibodies were dialyzed and concentrated into HEK buffer (20 mM HEPES, 100 mM KCl, and 1 mM DTT, pH 7.7) to a final concentration of 1.45 mg/ml. Cells were injected with HEK buffer alone

(controls), Kif2a or Hec1 9G3 antibody solution diluted 1:1 in HEK buffer (Kif2a alone or Hec1 alone), or a 1:1 mixture of Kif2a and Hec1 9G3 antibodies (Kif2a + Hec1 antibody co-injectionin). For microinjection, coverslips with HEC1-GFP PtK1 cells were mounted into modified Rose chambers (Rieder and Hard, 1990) without the top coverslip and incubated at 37°C with Phenol Red-free L-15 media (Gibco) complemented with 4.5 g/l glucose and covered with mineral oil to prevent evaporation. A volume corresponding to about 5% of the cell volume was injected into late prometaphase/early metaphase cells using a Narishige micromanipulator (NT-88-V3, Narishige) and a Harvard Apparatus microinjection system (PLI-100A, Harvard Apparatus).

### **3.4.3. Microscopy and image acquisition.**

Microinjected cells were imaged with Nikon Eclipse Ti inverted microscope (Nikon Instruments Inc.) with Lumen 200PRO fluorescence illumination system (Prior Scientific). The microscope was equipped with motorized stage (Prior Scientific) and images were obtained with an HQ2 CCD camera (Photometrics), using a 100X/1.4NA Plan-Apochromatic phase-contrast objective lens. Digital images were acquired using the NIS Elements software (Nikon Instruments Inc.). For the microinjection experiments described in Figure 3.2 and 3.3, imaging began shortly after injection. Near-simultaneous phase contrast and single focal plane epifluorescence images were acquired every 20 seconds for at least 11 minutes.

### **3.4.4. Kinetochore tracking.**

Kinetochore tracking in cells injected with Alexa 488-anti-CENP-F (Cimini et al., 2004) was performed using a previously developed MatLab (Math-Works, Natick, MA) program (Wan et al., 2012). HEC1-GFP signals were tracked manually aided by the same MatLab program (Wan et al.,

2012). KT position was defined as the Alexa 488/GFP signal centroid based on a 2-D Gaussian fitting method (Wan et al., 2012).

#### **3.4.5. Photoactivation of PAGFP-Tubulin.**

FDAP experiments were conducted in buffer- and anti-Kif2a-injected cells. Moreover, a set of data was collected from cells treated with 10  $\mu$ M Taxol and used for photobleaching correction.

Photoactivation was performed using a Mosaic Photoactivation System (Photonic Instruments/Andor) consisting of digital diaphragm optical head with micromirror array, using a 100 W Olympus (U-RFL-T) mercury lamp and a dichroic mirror that transmits light at 365–435 nm and reflects above 435 nm (He and Cimini, submitted). One phase-contrast image of the cell of interest was acquired and, using the phase-contrast image on the screen, a  $\sim$ 0.5  $\mu$ m-wide (9 pixels with our set-up) line perpendicular to the spindle long axis and located on one side of the metaphase plate was activated with a pulse of 1-2 sec. Phase contrast and fluorescence images were acquired immediately after photoactivation and every 15 seconds thereafter for about 5 minutes.

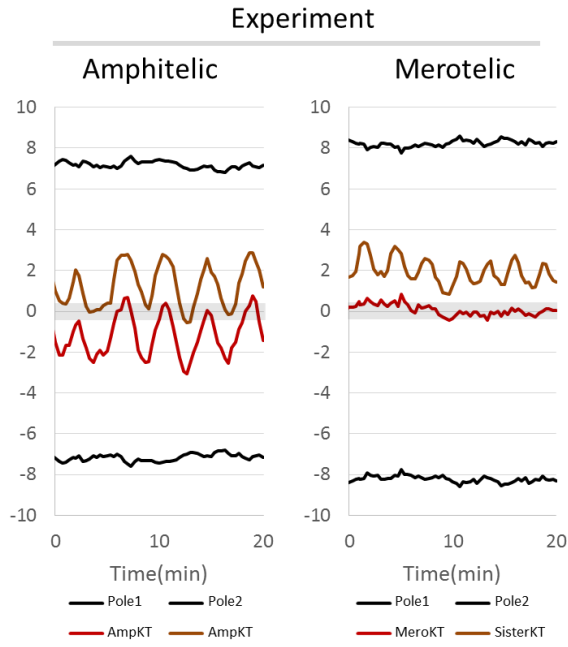
#### **3.4.6. MT poleward flux quantification.**

To measure MT poleward flux, we measured the change in distance between the activated of PAGFP line and the spindle pole using the NIS Elements software (Nikon Instruments Inc.).

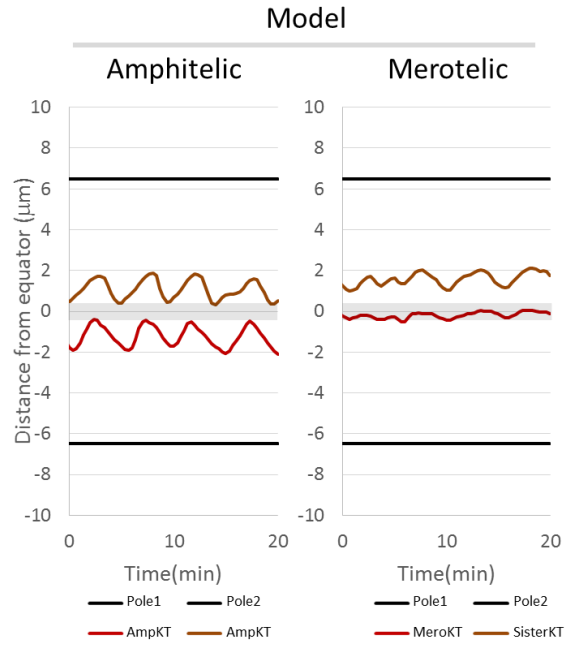
*3.4.7. Quantification of MT turnover rates.* In time lapse movie of photoactivated PAGFP-tubulin PtK1 cells, a rectangular region around the region of activation and an equivalent rectangular region on the opposite, non-activated, side of the spindle (for background fluorescence measurements) were selected. The total integrated fluorescence within those two regions at each time point was measured using NIS Elements software (Nikon Instruments Inc.). The rectangular regions for fluorescence and background measurements was moved at each time frame to follow the poleward

movement of the activated mark, except for Taxol-treated cells, in which the rectangular quantification regions was kept in the original location, as the mark does not move poleward. Fluorescence intensity at each time point was obtained by subtracting the background value from the value of the fluorescent mark. The measured values were then corrected for photobleaching by using measurements obtained from Taxol-treated cells and the resulting data were normalized to the  $t_0$  (time point immediately after photoactivation) value. Plots were generated for the different experimental conditions by averaging at each time point corrected data obtained from HEK buffer or anti-Kif2a injected PAGFP-tubulin PtK1 cells. The kinetics of fluorescence dissipation after photoactivation were then fit to a double exponential curve (Zhai et al., 1995), with equation  $y = A_1 * \exp(-k_1 * t) + A_2 * \exp(-k_2 * t)$ , where  $A_1$  and  $A_2$  represent the percentages of the total fluorescence contributed by non-KT and kMTs, respectively;  $k_1$  and  $k_2$  represent the rate constants of turnover/fluorescence dissipation for non-KT and kMTs, respectively; and  $t$  corresponds to the time after photoactivation. Microtubule half-lives ( $t_{1/2}$ ) were calculated as follows:  $t_{1/2} = \ln 2/k_1$  for non-KT MTs;  $t_{1/2} = \ln 2/k_2$  for kMTs.

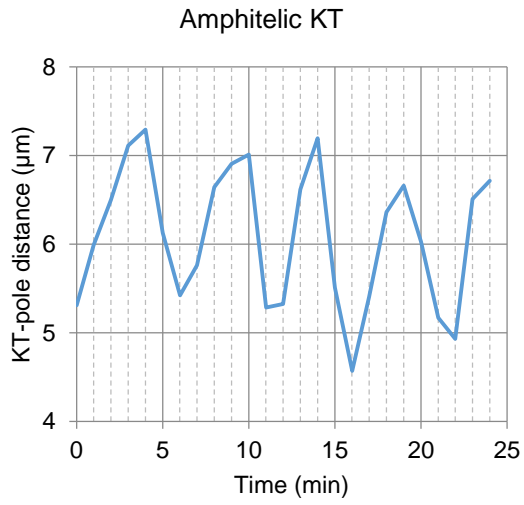
A



B



C



D

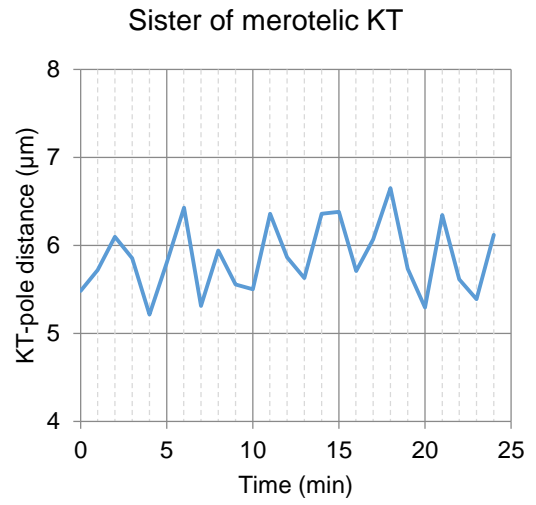
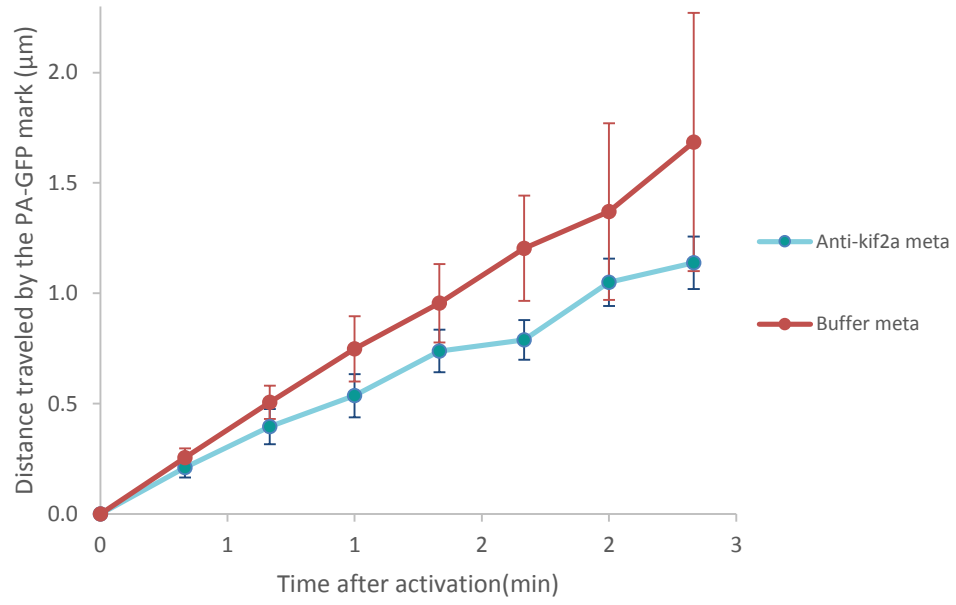


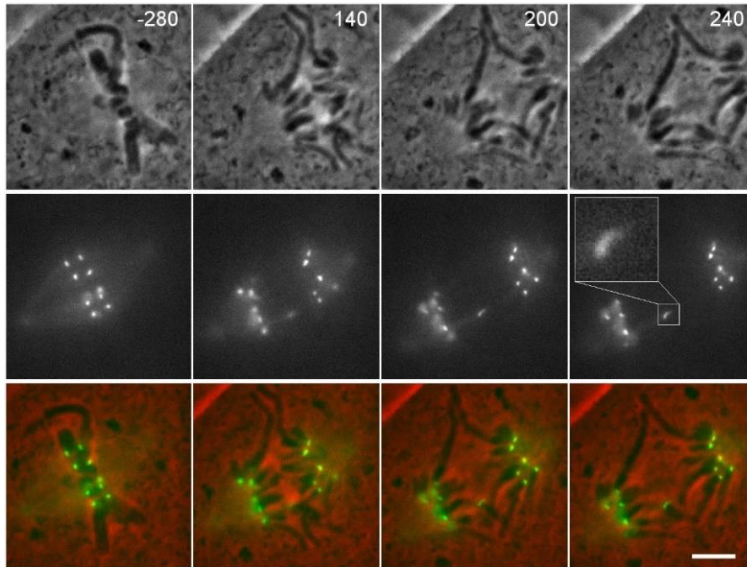
***Figure 3.1. Merotelic KT attachment changes the oscillation pattern of the normally attached sister.***

(A) Metaphase KT dynamics for amphitelic sister KTs (left) and a merotelic KT and its sister (right) quantified from PtK1 cells microinjected with Alexa488-anti-CENP-F antibodies and X-Rhodamins-labeled tubulin (Cimini et al., 2004). (B) Computer simulation result of metaphase KT dynamics for amphitelic sister KTs (left) and a merotelic KT and its sister (right). In both A and B, the brown and red lines represent KT positions relative to the spindle equator over time. In merotelic graphs, the red line represents the merotelically attached KT and the brown line corresponds to its normally attached sister. The black lines represent the spindle pole location relative to the spindle equator. (C-D) Changes in KT-pole distance (i.e., oscillations) for an amphitelic KT (C) and for the sister of a merotelic KT (D).

A



B



C

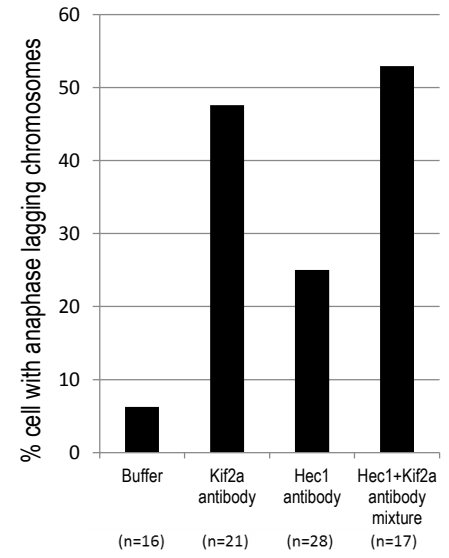
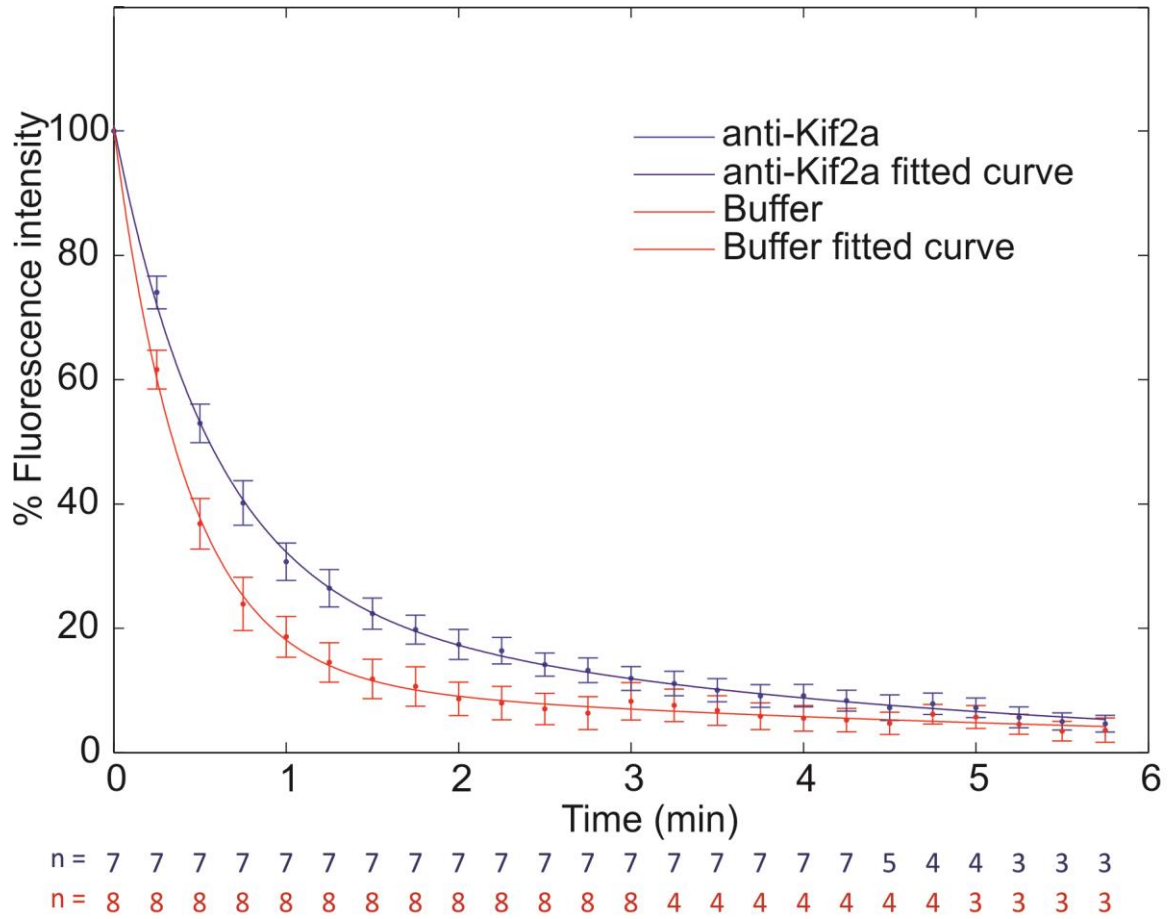


***Figure 3.2. Microinjection of anti-Kif2a antibodies results in reduced MT poleward flux and induces high rates of anaphase lagging chromosomes***

(A) Quantification of MT poleward flux in cells microinjected with buffer vs. anti-Kif2a antibodies.

The data are reported as average and standard error of the mean from 8 cells. (B) Example of GFP-HEC1 PtK1 cell microinjected with anti-Kif2a antibodies and displaying a LC Time stamps indicate elapsed time (in seconds) with respect to the time of anaphase onset. Scale bar, 5 $\mu$ m. The inset in the last time frame shows that the KT of the LC is stretched, which is a feature of merotelically attached KTs in anaphase. (C) Frequencies of LCs in GFP-HEC1 PtK1 cells injected as indicated in the X-axis labels.

A



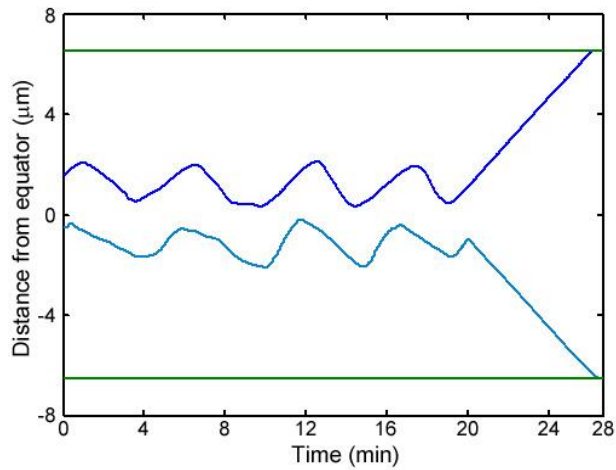
B

	MT Turnover						MT Poleward Flux	
	Non-Kinetochores MTs		Kinetochores MTs		R <sup>2</sup>	N	Mean ± SEM (µm/min)	N
	% ± SEM	t <sub>1/2</sub> (sec)	% ± SEM	t <sub>1/2</sub> (min)				
<b>Buffer</b>	88.43±2.68	17	11.99±2.35	3.80	0.9987	3-8	0.74±0.28	8
<b>Anti-Kif2a</b>	73.94±4.04	23	26.94±4.11	2.46	0.9991	3-7	0.49±0.21	8

***Figure 3.3. Quantification of MT dynamics by FDAP in buffer- vs. anti-Kif2a-injected cells.***

(A) Data from FDAP experiments. The filled circles represent the normalized and photobleaching-corrected mean fluorescence intensity values recorded at each time point after photoactivation. The bars represent the standard error of the mean at each time point. The lines represent the double exponential curves generated by nonlinear curve fitting. The n values below the graph indicate the sample size (number of cells analyzed) at each time point, with blue corresponding to anti-Kif2a-injected cells and red corresponding to buffer-injected cells (B) Table reporting the data obtained from the analysis in (A) and non-linear regression analysis (see materials and methods for details).

A



B

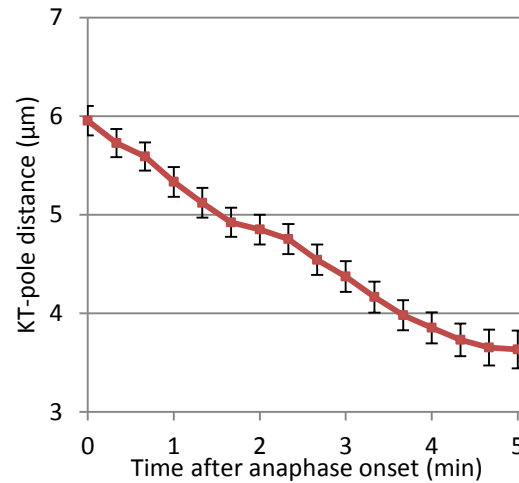


**Figure 3.4. Anaphase KT dynamics**

(A) The model developed for metaphase chromosome dynamics was used to simulate anaphase chromosome poleward movement after a period of chromosome oscillations at the metaphase plate. In the model, anaphase was initiated by simply cutting the cohesin bonds between the sister chromatids/KTs. This was sufficient to produce poleward KT movement. The graph shows the position of the sister KTs (shown in light and dark blue), and the spindle poles (shown in light and dark green) around the spindle equator. In the simulation, spindle pole separation is not occurring (no anaphase B). (B) Anaphase KT dynamics (poleward KT movement) in Hec1-GFP PtK1 cells. The data are reported as mean and standard error of the mean from 120 KTs.

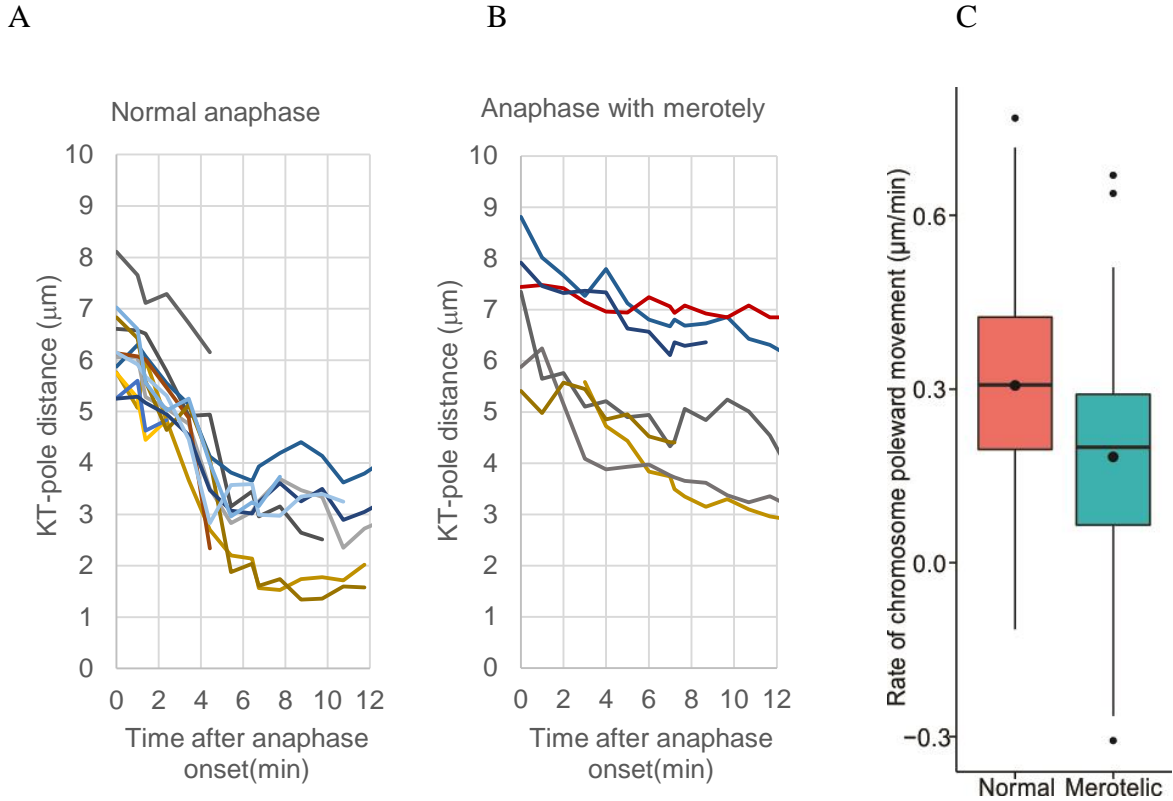


**Figure 3.5. Rates of KT poleward movement are reduced in anaphase cells with a merotelically attached LC.**

(A-B) Anaphase KT dynamics in a normal cell (A) and a cell with a merotelically attached LC (B). Each line represents the poleward movement of a single KT. The thick red line in (B) refers to the merotelically attached KT. (C) Comparison of poleward movement rates in cells with and without a merotelically attached LC over the 5 minutes after anaphase onset ( $p = 0.00001$ , Student t-test). Data from 166 KTs from normal cells and 73 normally attached KTs in cells with merotelically attached anaphase lagging chromosomes.

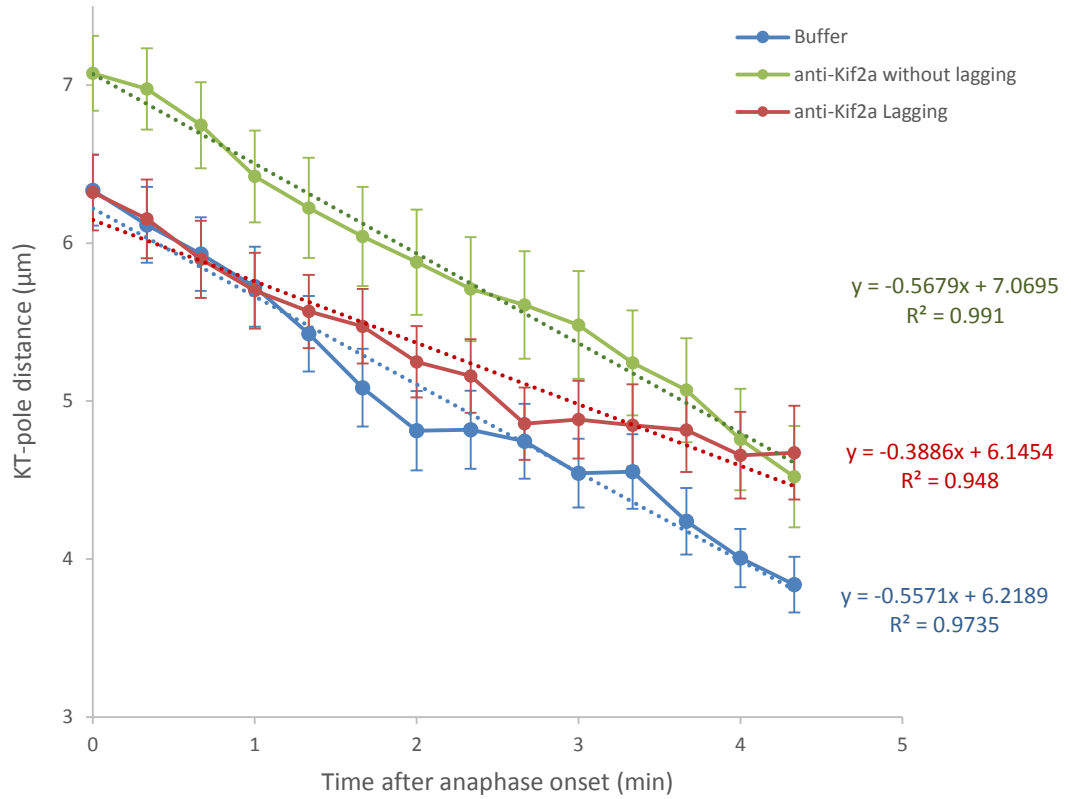


**Figure 3.6. KT poleward movement in buffer vs. anti-Kif2a-injected HEC1-GFP PtK1 cells**

Each data point in the graph reports mean and standard errors of the mean from 29-39 KT's. Anti-Kif2a injected cells were sorted in two groups consisting of cells in with (0.39 µm/min) or without LC (lagging) (0.57 µm/min). For the buffer injected control, poleward movement rate is 0.56 µm/min.

## **Chapter 4. Chromosomes missegregated into micronuclei contribute to CIN by missegregating at the next division**

Bin He<sup>1</sup>, Nisha Gnawali<sup>1,2</sup>, Albert W. Hinman<sup>1</sup>, Aaron J. Mattingly<sup>1,3</sup>, and Daniela Cimini<sup>1\*</sup>

<sup>1</sup>Department of Biological Sciences and Virginia Bioinformatics Institute, Virginia Tech, Blacksburg, VA, 24061 – USA

<sup>2</sup>Current address: Clinical Radiation Safety Department, VCU Medical Center, Richmond, VA, 23298 – USA

<sup>3</sup>Current address: Department of Cell & Tissue Biology, UCSF, San Francisco, CA, 94143 – USA

\*Corresponding author

Manuscript submitted

### **Author contributions**

Conceived and designed the experiments: BH and DC. Performed experiments: BH.

Analyzed the data: BH, NG, AWH, AJM. Contributed reagents/materials/analysis tools:

DC. Prepared the manuscript: BH and DC.

#### **4.1. Abstract**

Micronuclei (MNi) are extranuclear DNA-containing structures that form upon mitotic exit from unsegregated chromosome fragments or anaphase lagging (whole) chromosomes (LCs). MNi formed from whole chromosomes are of particular interest because LCs are frequently observed in both cancer and non-cancer cells, and are recognized as a major source of chromosomal instability (CIN) in cancer cells. Here, we generated a PtK1 cell line expressing a photoactivatable H2B histone to study the behavior of whole chromosome-containing MNi at the mitosis following their formation. We found that most micronucleated cells displayed some kind of chromosome segregation defect and that the missegregating chromosome was the one derived from the MN. Moreover, condensation of the chromosome within the MN was frequently delayed and associated with failure to align at the metaphase plate. Finally, micronucleated cells frequently displayed cytokinesis failure and tetraploidization. In summary, we find that chromosomes from MNi may trigger a CIN phenotype by missegregating at the mitosis following MN formation.

## 4.2 Introduction

Segregation of sister chromatids to opposite spindle poles during mitosis ensures equal chromosome distribution between the daughter cells. This is achieved through the attachment of sister chromatids to microtubules from opposite spindle poles in early mitosis. Individual sister chromatids can establish incorrect merotelic attachment by binding microtubules from both spindle poles (Cimini et al., 2001). When persisting through anaphase, some of these merotelically attached chromosomes can lag behind at the spindle equator when all the other chromosomes move to the spindle poles (Cimini et al., 2004; Cimini et al., 2003). Upon mitotic exit, an anaphase lagging chromosome (LC) forms a micronucleus (MN) enclosed in its own nuclear envelope separated from the main nucleus (Cimini et al., 2002). Chromosome fragments present at mitosis are also unable to move to the spindle pole and form micronuclei (MNi) upon mitotic exit. A number of simple MN-based techniques can be used to identify MNi (Fenech, 2000) and the combination of the MN assay with immunostaining for kinetochore (KT) proteins can be used to easily discriminate DNA fragment vs. LC-derived MNi (Degrassi and Tanzarella, 1988). Because of the ease of detection, MNi are extensively used as indicator of genetic damage, and high frequencies of MNi are found in cells with DNA repair or cell cycle checkpoint defects and in cells exposed to radiations or DNA damage-inducing chemicals or toxins (Fenech, 2000; Heddle and Carrano, 1977). Moreover, the frequency of MNi increases with age and is a biomarker for increased risk of cancer (Bonassi et al., 2001; Bonassi et al., 2007).

Despite the ample use of MN analysis as a measure of genetic damage, the basic biology of MNi and their impact on cell function are not fully understood. Some studies have reported higher rates of cell death in micronucleated (MNed) vs. non-MNed cells (Huang et al., 2011; Utani et al., 2010). However, the MNi in these studies were induced by ionizing radiation and replication stress,

respectively, thus raising the possibility that the increase in cell death may be due to high levels of genome-wide DNA damage and not simply to the presence of MNi. Other studies have shown that a number of cellular functions, including DNA replication, transcription, and DNA repair, are defective within the MN (Crasta et al., 2012; Hoffelder et al., 2004; Terradas et al., 2009). These defects were suggested to be, at least in part, caused by defective nuclear import due to abnormal assembly of the nuclear envelope/nuclear pore complex around the MN (Crasta et al., 2012; Hoffelder et al., 2004; Terradas et al., 2012). Moreover, the nuclear envelope of cancer cell MNi was shown to frequently collapse (Hatch et al., 2013), possibly explaining chromothripsis-like phenomena found concomitantly with MNi (Crasta et al., 2012). Nevertheless, MNi can also persist through subsequent cell cycles, as highlighted by live-cell imaging studies (Crasta et al., 2012; Huang et al., 2011; Utani et al., 2010).

The impact of whole chromosome-containing MNi on cell fate is of particular interest because such MNi originate from LCs, which represent the most common chromosome segregation defect found in chromosomally unstable cancer cells (Bakhoun et al., 2014; Thompson and Compton, 2008). Chromosome fragments, which would also give rise to MNi, are rarely observed in mitotic cells (Bakhoun et al., 2014). Although LCs are viewed as the major cause of chromosomal instability (CIN) in cancer cells (Bakhoun et al., 2014; Thompson and Compton, 2008), a recent study showed that a majority of LCs end up in the correct daughter cell in human colorectal cancer cells (Thompson and Compton, 2011), raising the question as to whether LCs have a real impact on CIN. Here, we addressed this question by examining chromosome segregation at the mitosis following the formation of whole chromosome-containing MNi in live PtK1 cells. To specifically follow the MN chromosome (mnChr), we generated a PtK1 cell line expressing photoactivatable GFP-tagged H2B histone.

### 4.3 Results and Discussion

Because spontaneous formation of MNi is rare in non-transformed mammalian cells, we used an STLC-washout protocol (see Material and Methods for details) to increase the frequency of LCs, which are known to form MNi upon mitotic exit (Cimini et al., 2002) (Figure 4.1A). This protocol allowed us to specifically study the fate and mitotic behavior of micronucleated (MNed) PtK1 cells at the mitosis following MN formation.

#### 4.3.1. Cells with whole-chromosome MNi are as likely as non-MNed cells to enter mitosis.

First, we asked whether MNed cells re-entered mitosis after MN formation. To this end, we fixed cells 24 hours after the STLC washout and determined the fraction of MNed vs. non-MNed cells re-entering mitosis by identifying cells positive for phosphorylated histone H3 (p-H3) staining (Figure 4.1B), but in which the nuclear envelope had not broken down. We found that this “prophase index” was similar between MNed and non-MNed cells (Figure 4.1C), thus indicating that the fraction of MNed cells re-entering mitosis was sufficiently large to allow analysis of MNed cells at the mitosis following MN formation. Consistent with this, long-term live cell imaging showed that the percentage of MNed cells re-entering mitosis during imaging was similar to that of randomly sampled non-MNed cells (27.4% and 26.7%, respectively; Figure 4.1D). Moreover, we found that only a very small portion of MNed cells died (2% in interphase and 0.7% in mitosis) during imaging (Figure 4.1D). Although these rates of cell death are higher than those observed in non-MNed cells (in which cell death was never recorded during imaging), they are much lower than those observed in cells with DNA damage-induced MNi (Huang et al., 2011; Utani et al., 2010), suggesting that the cell death observed in these previous studies was likely due to widespread DNA damage and not to the presence of a MN. Finally, we examined the integrity of the nuclear envelope in our

experimentally-induced whole chromosome MNi, to exclude the possibility that the membrane of such MNi was collapsing, as previously reported for cancer cell MNi (Hatch et al., 2013). As a measure of nuclear membrane integrity, we assessed the presence of the retinoblastoma protein (Rb) (Figure 4.1E), which was previously shown to be a good indicator of nuclear membrane integrity (Hatch et al., 2013). We found that most MNi retained Rb staining (Figure 4.1F), indicating that most of our whole-chromosome MNi did not experience membrane collapse/rupture. In conclusion, these data indicate that after formation of whole chromosome-containing MNi, MNed cells can re-enter mitosis with intact MNi. Thus, we used the STLC-washout protocol to induce the formation of MNed cells and study their behavior at the mitosis following their formation.

#### **4.3.2. MNed cells display high rates of chromosome segregation errors and further MN formation.**

To study the behavior of MNed cells at the mitosis following MN formation, we used the data from our long-term time-lapse phase-contrast imaging experiments (Figure 4.1D) and examined the MNed and non-MNed cells that underwent mitosis during imaging (Figure 4.2A-B). We found that MNed cells frequently displayed chromosome segregation errors, including chromosomes that never aligned at the metaphase plate (Figure 4.2A, C) and chromosomes that aligned, but lagged behind at the spindle equator in anaphase (Figure 4.2B-C). As a result of these chromosome segregation errors, in many cases (41.5%) MNi formed in one or both of the daughter cells (Figure 4.2A-C). Moreover, MNi also formed in daughter cells of MNed cells undergoing mitosis with no detectable chromosome segregation errors (Figure 4.2C). Only a small portion (~11%, 4 out of 36) of MNed cells segregated their chromosomes without visible defects and yielded daughter cells without MNi (Figure 4.2C). Overall, most MNed cells displayed chromosome segregation errors (Figure 4.2D) at

the mitosis following MN formation.

#### **4.3.3. The mnChr is responsible for the segregation errors.**

Although in some cases it was possible to identify the mnChr as the missegregating chromosome in MNed cells imaged by phase-contrast (Figure 4.2A), in many other cases, it was not clear whether the mnChr or some other chromosome was the one missegregating (Figure 4.2B). However, the high rates of chromosome missegregation in MNed cells compared to non-MNed cells (Figure 4.2D) suggested that the mnChr may indeed be the missegregating chromosome in most cases. To test this, we generated a PtK1 cell line stably expressing photoactivatable-GFP-tagged H2B histone (H2B-PAGFP PtK1) and used it to specifically mark the entire MN (i.e., the mnChr). Preliminary experiments in which we activated the entire nucleus of prophase cells showed that photoactivation of H2B did not affect chromosome segregation. Moreover, as a control for MN activation, we activated a chromosomal region within prophase nuclei (Figure 4.3A) and found that missegregation of these nuclear chromosomes was very rare (Figure 4.3D-F). To track the mnChr, we initially followed MNed cells by phase contrast and photoactivated the MN at the time of nuclear envelope breakdown (as detected for the main nucleus). In the vast majority of cases, the mnChr displayed some kind of segregation defect (Figure 4.3F). These included anaphase bridges (Figure 4.3D), anaphase lagging (Figure 4.3E), and chromosomes that never aligned at the metaphase plate (Figure 4.3E). Some of these chromosome segregation defects were also associated with further MN formation upon mitotic exit (Figure 4.3E). It is important to note that none of the cells with MN photoactivation displayed missegregation of chromosomes from the main nucleus, confirming that the chromosome missegregation events observed in MNed cells involve the mnChr and not chromosomes from the primary nucleus. In some cases, although the mnChr displayed apparently

normal condensation (Figures 2A and 3B) and even aligned at the metaphase plate (Figure 4.3B), upon separation, the two sister chromatids failed to segregate properly and ended up in the same daughter cell (Figures 2A and 3B), in some cases within the same MN (Figure 4.2A). This is a clear example of segregation of two sister chromatids to the same daughter cell, a phenomenon that is traditionally referred to as nondisjunction and leads to numerical chromosome aberrations in the daughter cells. In other cases, the missegregation event was even more obvious, as the mnChr did not align at the metaphase plate prior to anaphase onset. This behavior suggests that some mnChrs may be ineffective at mounting a mitotic checkpoint response, which typically delays anaphase onset until all chromosomes have become attached to microtubules and aligned at the metaphase plate (Lara-Gonzalez et al., 2012). This defective mnChr behavior could be due to defective nuclear pore assembly around MNi (Crasta et al., 2012; Hoffelder et al., 2004; Terradas et al., 2012), as the nuclear pore was shown to play a key role in the assembly of an anaphase inhibitor at a pre-mitotic stage (Rodriguez-Bravo et al., 2014). Moreover, intact nuclear pores are also expected to be critical for import of outer KT proteins required for recruitment of mitotic checkpoint proteins (Cheeseman and Desai, 2008). In support of a possible defect in import of outer KT proteins inside the MN, we found live prophase MNed cells in which the outer KT protein Hec1 was not recruited to the MN at a time when it was clearly associated with the chromosomes within the main nucleus (Figure 4.S1).

#### **4.3.4. Delayed condensation of the mnChr and cytokinesis failure in MNed cells.**

In our live cell images, we noticed that the DNA in the MN frequently appeared less condensed compared to the chromosomes within the main nucleus prior to or at the time of nuclear envelope breakdown (see for instance -6, 0, and 3 min frames in Figure 4.2B and Figure 4.4A). In some cases, condensation of the mnChr increased after nuclear envelope breakdown, but did not reach the levels

of condensation observed for chromosomes in the main nucleus (Figure 4.4A). These observations suggested that condensation of the mnChr was generally delayed compared to chromosomes in the main nucleus. We thus assessed MN condensation by quantifying the fluorescence intensity of histone H3 Ser10 phosphorylation (p-H3) in the MN as compared to the main nucleus within individual MNed prophase cells. As expected, the intensity of p-H3 gradually increased during prophase (Figure 4.4B), but in most MNed cells, the levels of p-H3 were lower in the MN compared to the main nucleus (Figure 4.4C-D), so that in ~90% of MNed cells, the level of p-H3 in the main nucleus was higher than that found in the MN. Thus, chromosome condensation is significantly delayed inside the MN compared to the main nucleus. This finding adds to the observation that DNA replication can be still ongoing in the MN when the main nucleus is in the G2 phase of the cell cycle (Crasta et al., 2012). In some cases, condensation of the mnChr seemed to be stimulated upon breakdown of the main nucleus' nuclear envelope, similarly to the phenomenon observed upon fusion of mitotic and interphase cells (Johnson and Rao, 1970). However, in other cases the mnChr seemed to persist in an undercondensed state (Figure 4.4A). This undercondensation could explain the increased rates of cytokinesis failure in MNed vs. non-MNed cells we observed in our phase-contrast live-cell imaging experiments (Figure 4.5A-C). As shown in Figure 4.5A, in some MNed cells, the undercondensed mnChr persisted at the spindle equator as all other chromosomes moved to the poles. The mnChr was unable to clear the spindle equator area upon furrow ingression, remained trapped by the cytokinetic furrow (Figure 4.5A-B), and eventually resulted in furrow regression (Figure 4.5B). Interestingly, cytokinesis failure was specifically induced by lagging/unaligned mnChrs, but not by STLC-induced LCs. Indeed, none of the 59 anaphase lagging chromosomes we followed upon STLC washout (Figure 4.1A) became trapped at the cleavage furrow. Instead, these chromosomes, which displayed normal condensation, were displaced to one side of the ingressing furrow and formed MNi (Figure 4.1A), as previously described (Cimini et al.,

2002).

#### **4.3.5. Conclusion**

In summary, our data show that mnChrs are particularly prone to missegregation and can display a variety of abnormal mitotic behaviors (see Figure 4.5D for summary of mnChr segregation errors observed in this study), including segregation of two sister chromatids to the same daughter cell (Figure 4.5D), a phenomenon not commonly observed when LCs arise for the first time (Thompson and Compton, 2011), and trapping within the cleavage furrow (likely due to mnChr marked undercondensation), a behavior we never observed for “first-time” LCs. The trapping of mnChr in the cytokinetic furrow is particularly significant because it can lead to cytokinesis failure and hence tetraploidy, a condition known to contribute to CIN by either increased rates of chromosome missegregation (Ganem et al., 2007) or by increased tolerance to aneuploidy (Dewhurst et al., 2014). Thus, by missegregating at the cell division following MN formation, whole chromosome MNi trigger a series of chromosome missegregation events that will lead to CIN. Because CIN is a common feature of cancer cells, our finding that MNi can represent the first step toward the acquisition of a CIN phenotype can explain the previously observed link between MN frequency and increased cancer risk (Bonassi et al., 2007).

## **4.4. Materials and Methods**

### **4.4.1. Generation of H2B-PAGFP PtK1 cell line.**

A PtK1 cell line stably expressing the H2B gene fused to PAGFP was produced through the transduction of retroviral particles according to the instructions for high-titer retrovirus production provided by Clontech. A H2B-PAGFPN1 plasmid was initially obtained as a kind gift from Dr. Jon Pines (The Gurdon Institute, University of Cambridge, UK). The H2B-PAGFP gene was then subcloned into the Not I and Hind III sites of the pLPCX retroviral vector (Clontech Laboratories, Inc.) that harbors the  $\Psi^+$  packaging sequence. In order to produce high efficiency, replication-incompetent, retroviral particles, packaging GP2-293 cells (Clontech Laboratories, Inc.), which carry the viral *gag* and *pol* genes, were transfected with the H2B-PAGFPpLPCX plasmid together with the pVSV-G vector (Clontech Laboratories, Inc.) that provided the viral envelope gene (*env*). The resulting retroviral particles were used to infect PtK1 cells that were subsequently placed under selection in Puromycin-containing media to obtain the final H2B-PAGFP cell line used in this study.

### **4.4.2. Cell culture and treatment.**

PtK1, H2B-PAGFP PtK1, and HEC1-GFP PtK1 (Civelekoglu-Scholey et al., 2013) cells were cultured in Ham's F-12 media (Invitrogen) supplemented with 10% Fetal Bovine Serum (Invitrogen), 1 mM sodium pyruvate (Invitrogen), 14 mM sodium bicarbonate (Fisher Scientific), 1% antibiotic-antimycotic (Invitrogen), and maintained at 37°C in a humidified CO<sub>2</sub> incubator. For live cell imaging, cells were either grown on glass-bottom dishes and imaged using a stage top incubator (Tokai Hit) or were grown on sterilized coverslips inside 35 mm Petri dishes, transferred into a modified Rose chamber (Rieder and Hard, 1990) with top coverslip, and imaged on a

microscope stage heated by an air stream incubator (Nevtek). To induce LCs and MNi, cells were incubated in 20  $\mu$ M STLC for 3 hours. The drug was then washed out by rinsing the cells 4 times with warm media. Cells were then re-incubated in fresh Ham's F-12 media for 24 hours before immunostaining or live-cell imaging. For live-cell imaging, cells were placed in phenol-free L-15 media (Gibco) with 4.5 g/liter glucose.

#### **4.4.3. Immunofluorescence staining, image acquisition, and image analysis.**

For histone H3 Ser10 phosphorylation (p-H3) and Rb immunofluorescence, PtK1 cells were fixed in freshly prepared 4% formaldehyde for 20 minutes. Cells were then permeabilized in 0.5% Triton X-100 in PHEM buffer (60mM Pipes, 25mM HEPES, 10mMEGTA, 1mM MgSO<sub>4</sub>, pH 7.0) for 10 min. Cells were next incubated for one hour at room temperature in a blocking solution consisting of 10% boiled goat serum in PHEM buffer, followed by overnight incubation at 4°C in primary antibodies. Next, cells were subjected to 4 five-minute washes in PBS with 0.1% Tween 20 (PBST) and then incubated for 45 minutes at room temperature with secondary antibodies. Cells were finally washed (4x5 min) in PBST, stained with DAPI, washed again, and mounted in an antifade solution (90% glycerol, 10% Tris buffer, 0.5-1% n-Propyl gallate). The antibodies were all diluted in 5% boiled goat serum as follows: rabbit anti-phospho-(Ser10)histone H3 (Millipore), 1:100; mouse anti-Rb(4H1) (Cell Signaling Technology), 1:200; Red-X-goat anti-rabbit (Jackson ImmunoResearch laboratories inc.), 1:100; Red-X-goat anti-mouse (Jackson ImmunoResearch laboratories inc.), 1:200.

Imunostained PtK1 cells were imaged on a swept field confocal unit (Prairie Technologies) attached to a Nikon Eclipse TE-2000U inverted microscope. The microscope was equipped with a 100 $\times$ /1.4 NA Plan-Apochromatic phase-contrast objective lens, phase-contrast transillumination, transmitted

light shutter, and automated ProScan stage (Prior Scientific). The confocal head was accessorized with multiband pass filter set for illumination at 405, 488, 561, and 640 nm, and illumination was obtained through an Agilent monolithic laser combiner (MLC400) controlled by a four channel acousto-optic tunable filter. Digital images were acquired with a HQ2 CCD camera (Photometrics). Acquisition time, Z-axis position, laser line power, and confocal system were all controlled by NIS Elements AR software (Nikon Instruments Inc.) on a PC computer (Dell). Z-series optical sections through each cell analyzed were obtained at 0.6  $\mu\text{m}$  steps.

Quantification of histone H3 phosphorylation (p-H3) was performed in ImageJ with background intensity subtraction adapted from (Hoffman et al., 2001). For MN intensity, the DNA signal visualized by DAPI was used to draw a polygon (with area =  $A_{\text{Inner(MN)}}$  and mean fluorescence intensity =  $I_{\text{Inner(MN)}}$ ) approximately corresponding to the MN area. A larger outer polygon (with area =  $A_{\text{Outer(MN)}}$  and mean fluorescence intensity =  $I_{\text{Outer(MN)}}$ ) was traced around the MN polygon in an off-centered position, so that it would not overlap with the main nucleus and was traced in a way that it extended beyond the MN; the same thing was done for the main nucleus (see Figure 4.S2, top diagram). Both DAPI and p-H3 fluorescence intensities were quantified for each MNed cell to obtain p-H3 fluorescence intensity relative to the DAPI fluorescence intensity. A nucleus to micronucleus ratio was then calculated and reported in Figure 4.4D. A detailed description of the method used for these fluorescence intensity quantifications is reported in Figure 4.S2.

#### **4.4.4. Phase-contrast live-cell imaging**

Phase-contrast live-cell imaging was performed on a Nikon Eclipse Ti inverted microscope equipped with phase-contrast transillumination, transmitted light shutter (Sutter Instruments), ProScan automated stage (Prior Scientific), and HQ2 CCD camera (Photometrics). Image

acquisition, light shutter, and XYZ-axis positions were all controlled by NIS Elements AR software (Nikon) on a PC computer. For short-term phase-contrast live-cell imaging (Figure 4.1A), cells were imaged in a modified Rose chamber and maintained at  $\sim 36^{\circ}\text{C}$  by means of an air stream incubator (Nevtek). For initial analysis of MN formation (Figure 4.1A), multiple monopolar cells were identified, the XYZ coordinates were recorded, and then images of individual cells were acquired every minute throughout mitosis, up to 90 minutes, using a 60x/1.4 NA Plan-Apochromatic phase contrast objective. For long-term phase-contrast live cell imaging (Figures 1D, 2A-B, and 5A-B), cells were imaged in 35 mm Petri dishes in a stage top incubator (Tokai Hit), with temperature set at  $\sim 36^{\circ}\text{C}$ . 10 or more MNed cells were selected and the XYZ coordinates recorded. The same number of non-MNed cells were selected by selecting one non-MNed cell within the same field of view and positioned next to the selected MNed cells. Image acquisition was performed as described above, except that images were acquired every 2-3 minutes for 17-80 hours using a 40x/0.6 NA Plan Fluor ELWD phase contrast objective. The data collected in these experiments were used to determine the ability of MNed cells to re-enter mitosis after MN formation compared to non-MNed cells (Figure 4.1D); the cells going through mitosis during the period of imaging were then further analyzed to determine chromosome segregation defects (Figure 4.2); finally, the cells imaged beyond mitosis were analyzed to measure the rates of cleavage furrow regression (Figure 4.5A-C).

#### **4.4.5. Chromosome photoactivation and imaging**

H2B-PAGFP PtK1 cells were either grown into glass-bottom dishes (MatTek) or grown on coverslips and then transferred into a modified Rose chamber with top coverslip filled with Phenol red-free L-15 media (Gibco). The day following MN induction, cells were placed on a Nikon Eclipse Ti microscope equipped with transmitted light shutter, Lumen 200PRO fluorescence

illumination system (Prior Scientific), HQ2 CCD camera (Photometrics), and ProScan automated stage (Prior Scientific). Temperature was controlled by either (for Rose chambers) an air stream incubator (Nevtek) or (for glass-bottom dishes) by a stage top incubator (Tokai Hit). Up to 40 MNed cells were initially identified, the XYZ coordinates recorded, and cells followed by phase-contrast microscopy acquiring images every 2-5 minutes with 60x/1.4 NA Plan-Apochromatic phase contrast objective lens. The cells were monitored until any of the cells reached late prophase, as determined by the level of condensation of chromosomes in the primary nucleus. At that time, imaging was interrupted to perform photoactivation of the MN, a condensed chromosome in the main nucleus (used as control), or both. Photoactivation was performed using a Mosaic Photoactivation System (Photonic Instruments/Andor) consisting of digital diaphragm optical head with micromirror array, using a 100 W Olympus (U-RFL-T) mercury lamp and a dichroic mirror that transmits light at 365–435 nm and reflects above 435 nm. One phase-contrast image of the cell of interest was acquired and, using the phase-contrast image on the screen, a region of interest was selected around the MN, around a chromosome within the main nucleus, or both, and photoactivation was achieved by illumination of the region(s) of interest through five focal planes at 0.6  $\mu\text{m}$  intervals, with pulses of 100 ms at each focal plane. Imaging was resumed after photoactivation by acquiring fluorescence and phase-contrast images. Initially, fluorescence images were acquired sporadically, and mitotic events were monitored by phase-contrast imaging, until the cell reached late metaphase, at which time fluorescence and phase-contrast images were acquired simultaneously to capture chromosome segregation events involving the activated chromosomes.

## **Acknowledgements**

We would like to thank Jon Pines (The Gurdon Institute, University of Cambridge, UK) for providing the initial H2B-PAGFPN1 plasmid. We are also indebted to Pat Casey (Duke University, Durham, NC, USA), who allowed the generation of the H2B-PAGF PtK1 cell line in his laboratory and former Casey lab member Dan Kaplan, who was instrumental in assisting with the generation of the cell line. We are also grateful to Ted Salmon (University of North Carolina at Chapel Hill, NC, USA) for allowing DC to generate the H2B-PAGF PtK1 cell line during her postdoctoral training in his lab and for critical reading of the manuscript. Finally, we would like to thank all the members of the Cimini lab for useful discussion and helpful comments. This work was partly supported by NSF grant MCB-0842551 to DC. Additional funding was provided by HFSP grant RGY0069/2010 to DC.

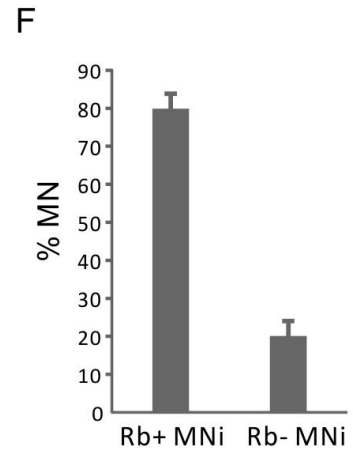
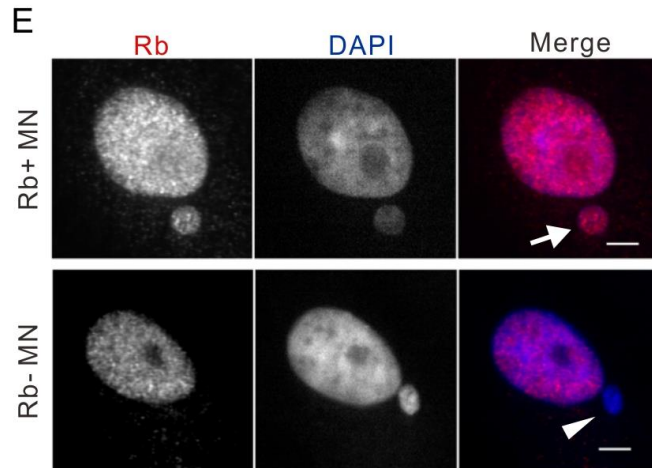
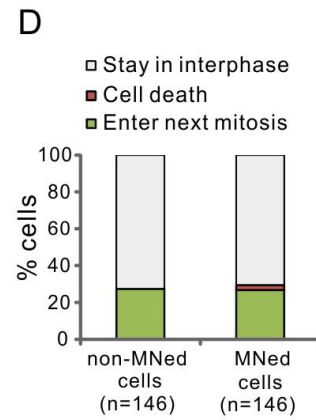
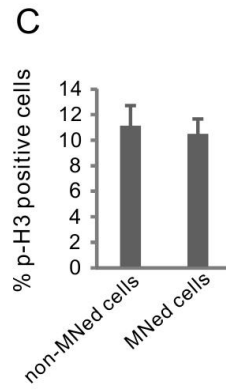
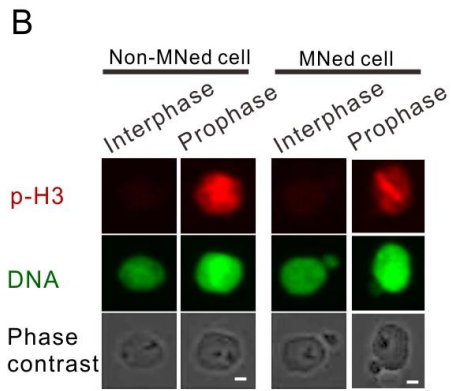
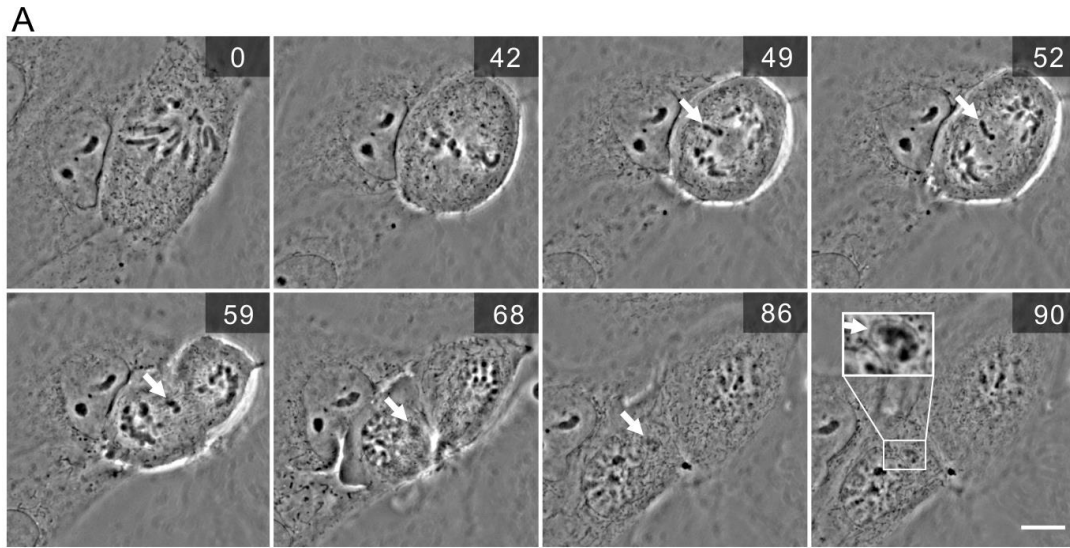


***Figure 4.1. MNed PtK1 cells progress through the cell cycle and maintain integrity of MN envelope***

(A) Still images from time-lapse phase contrast movie showing formation of whole chromosome-containing MNi in PtK1 cells after STLC washout. White arrow indicates the LC and the MN it forms upon mitotic exit. Inset in the last frame shows a 2X enlargement of the newly formed MN. Time stamps represent elapsed time in minutes. Scale bar, 10  $\mu\text{m}$ . (B) pH3 immunostaining (red) used to identify MNed prophase cells. MNi in prophase cells were identified by DAPI staining (green) and phase contrast microscopy. Scale bar, 5  $\mu\text{m}$ . (C) Quantification of pH3-positive MNed and non-MNed cells showing similar numbers of prophase cells within the two subpopulations. The data reported represent the average of three independent experiments in which a total of 1319-1351 cells were analyzed, with 98-114 cells being MNed. (D) Quantification of proliferation and death rates in MNed and non-MNed cells obtained by long term time-lapse phase contrast microscopy. (E) Loss of nuclear localization of the retinoblastoma (Rb) protein is used as a marker for nuclear envelope rupture (Hatch et al., 2013). Intact (arrow) and ruptured (arrowhead) MN in fixed PtK1 cells immunostained for Rb (left/red). The RB- MN is clearly visible by DAPI staining (middle/blue). Scale bar, 5  $\mu\text{m}$ . (F) Quantification of Rb<sup>+</sup> vs. Rb<sup>-</sup> MNi shows that most of the MNi maintained nuclear localization of Rb protein, which is indicative of intact nuclear envelope. The data represent the mean  $\pm$  s.e.m. calculated from three independent experiments in which 179-291 MNed cells were analyzed.

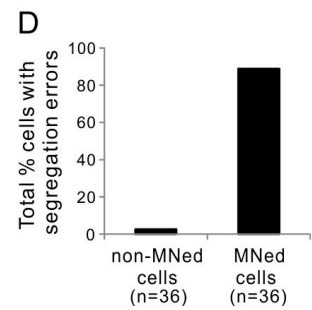
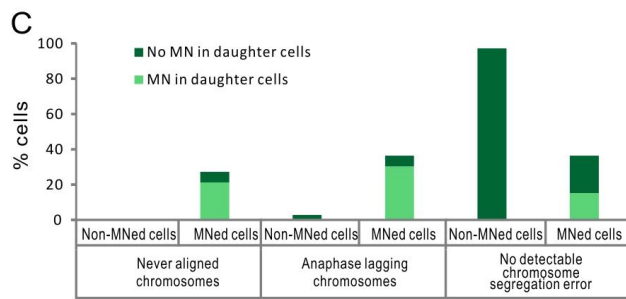
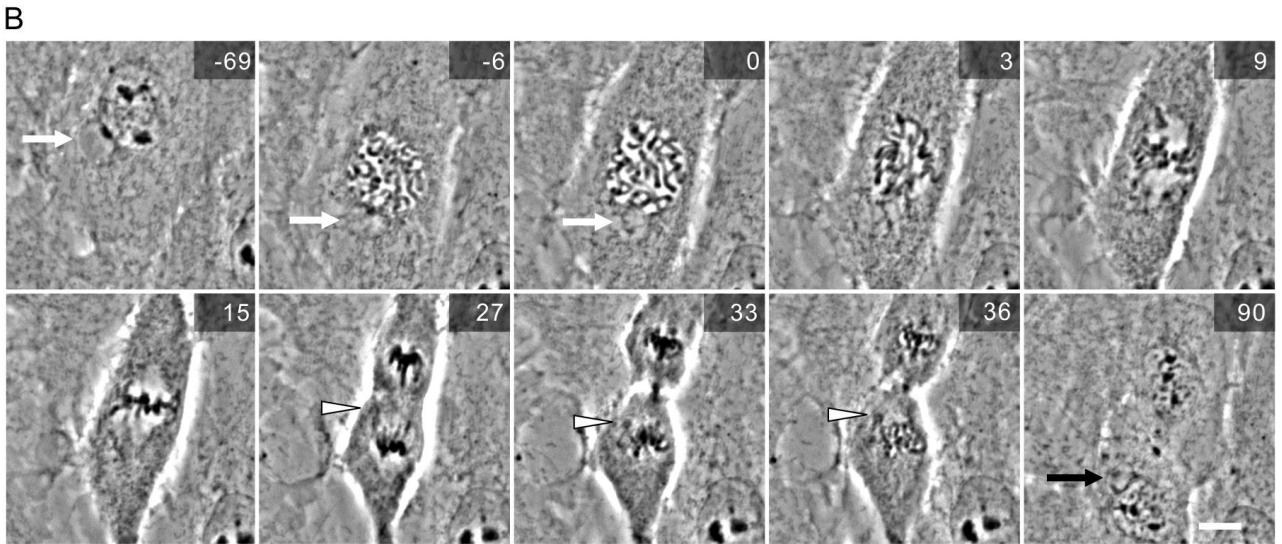
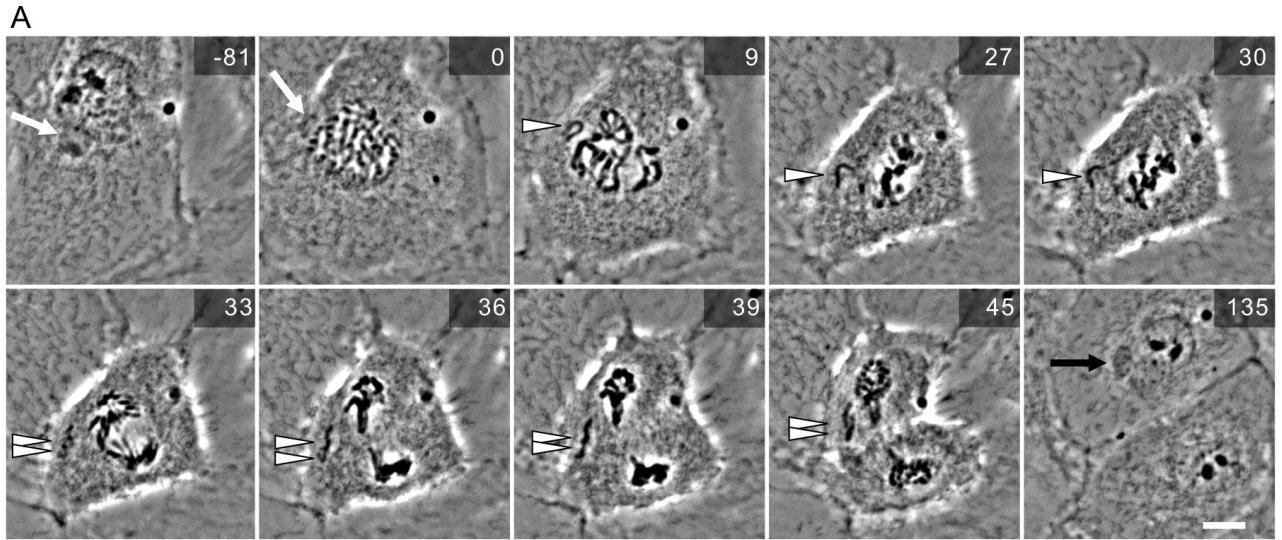


***Figure 4.2. High rates of chromosome segregation errors in MNed cells***

(A-B) Representative time-lapse phase contrast micrographs of MNed cells that enter mitosis and display chromosome segregation errors. White arrows point at the MNi; white arrowheads indicate missegregating chromosomes/chromatids; black arrows indicate the newly formed MNi in one of the daughter cells. Scale bar, 10  $\mu$ m. (A) MNed cell with a missegregating chromosome that never aligns at the metaphase plate. After anaphase onset, the sister chromatids appear to separate from each other, but fail to move to the spindle poles. Instead, they lag near the cell equator and end up in the same MN in one daughter cell. (B) In this cell, when the nuclear envelope of the main nucleus breaks down, the mnChr appears under-condensed. The mnChr becomes mingled with the rest of the chromosomes, but at the end of mitosis a LC becomes visible and gives rise to a new MN in one of the daughter cells upon mitotic exit. (C) Quantification of chromosome segregation errors in live cell experiments. (D) Percentage of cells displaying at least one chromosome segregation error.

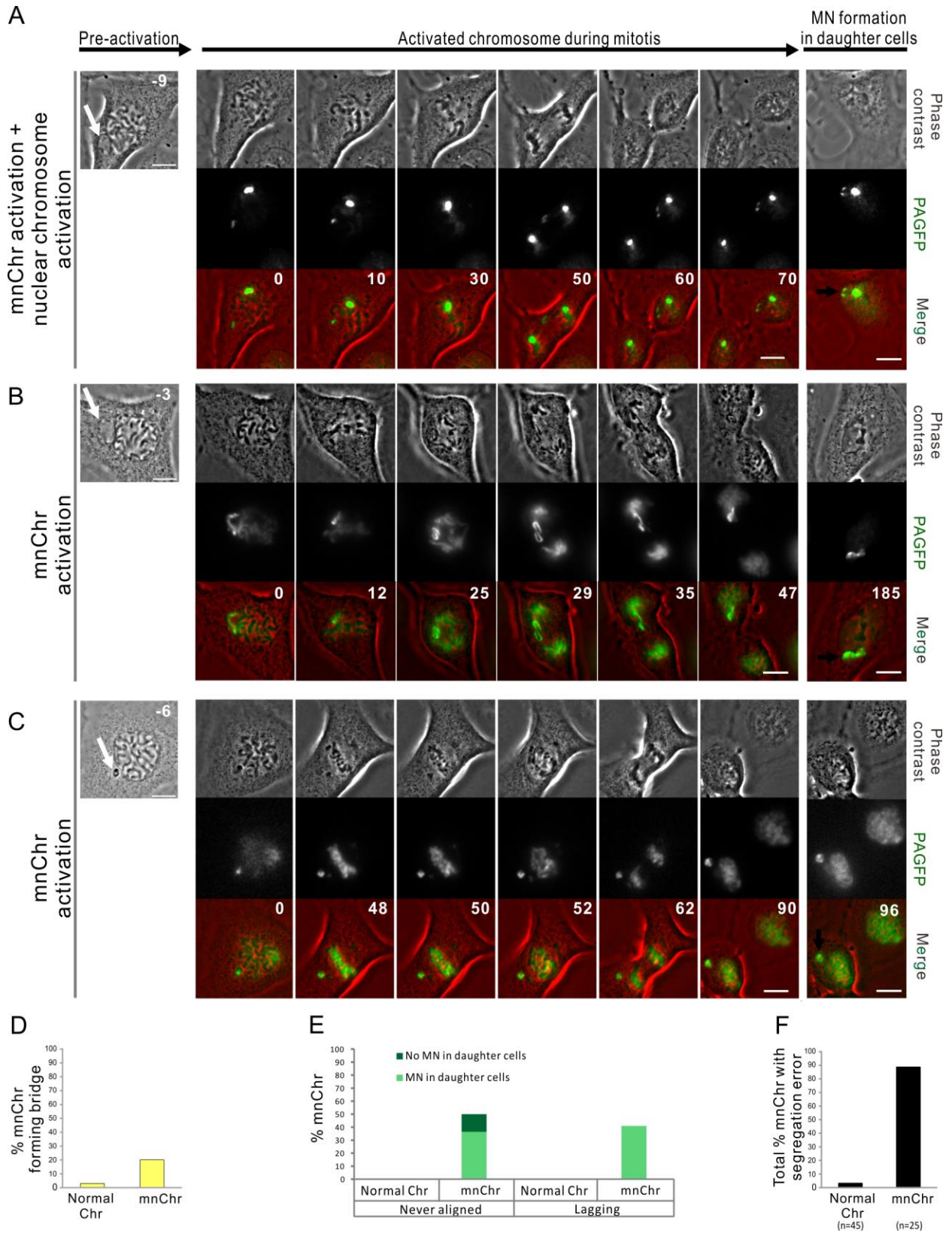


**Figure 4.3. MN photoactivation shows that the mnChr is responsible for the segregation errors observed in MNed cells**

(A-C) Chromosomes in the main nucleus and/or in MNi (white arrow) were marked by photoactivation of H2B-PAGFP in PtK1 cells. Right panels in A-C show the MNed cell prior to photoactivation, and the white arrow points at the MN. The remaining panels show still images from time-lapse movies acquired after fluorescence photoactivation, with the frame on the right corresponding to a late time point to show MN formation (black arrow) in one of the daughter cells. For each cell, phase contrast images are shown in the top row, fluorescence images are shown in the middle row, and the overlay is shown in the bottom row. Time stamps indicate elapsed time in minutes. Scale bars, 10  $\mu\text{m}$ . (A) One small region (corresponding to one chromosome) within the main nucleus and the mnChr were activated in this cell. The images show that the chromosome from the main nucleus segregates correctly, whereas the sister chromatids from the mnChr lag behind, ending up in the same daughter cell and in the same MN. (B) The mnChr aligns at the metaphase plate and its sister chromatids separate at anaphase onset. However, they lag behind, co-segregate to the same daughter cell, and form two MNi upon mitotic exit. (C) The mnChr in this cell never aligns at the metaphase plate, persists in the same position throughout mitosis, and re-forms a MN in one of the daughter cells upon mitotic exit. (D-E) Quantification of various chromosome segregation errors in photoactivation experiments. Normal Chr refers to photoactivated chromosomes within the main nucleus of a MNed cell. (H) Percentage of photoactivated chromosomes displaying at least one segregation error.

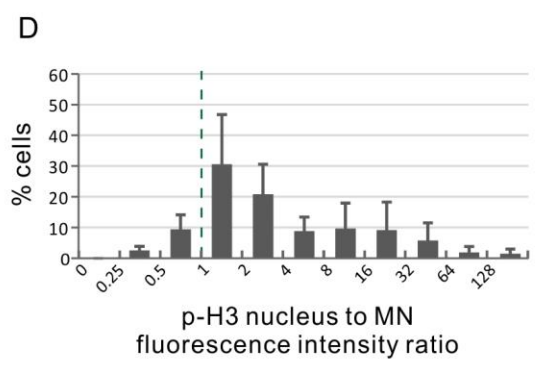
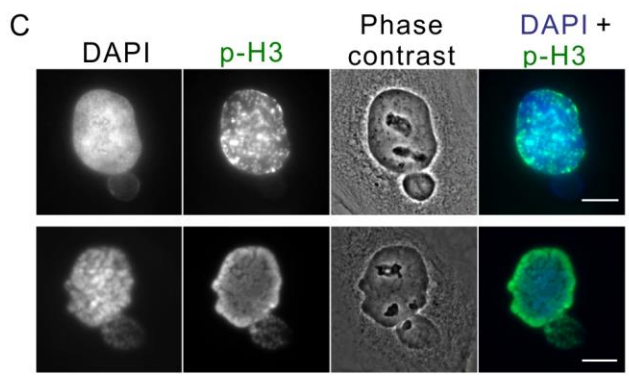
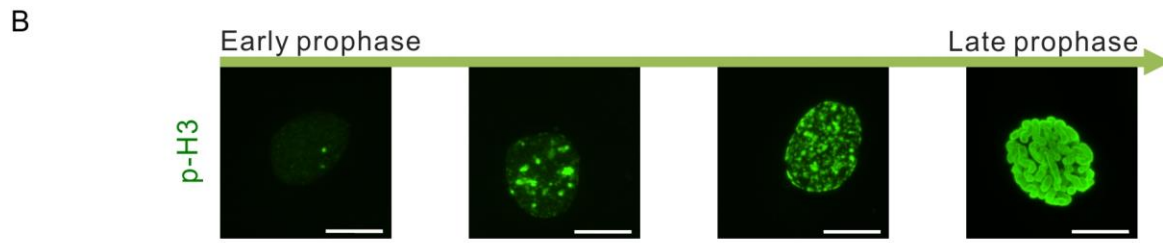
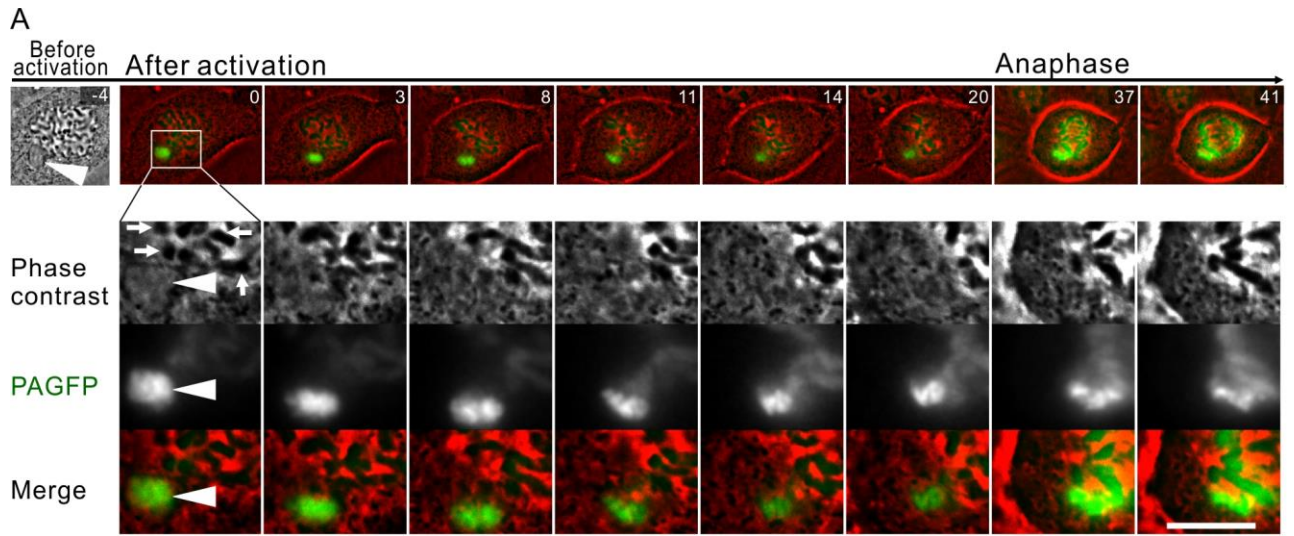


***Figure 4.4. Delayed chromosome condensation of mnChrs***

(A) Photoactivated mnChr (white arrowhead) appears clearly under-condensed compared to the chromosomes in the main nucleus. The time stamps indicate elapsed time in minutes. At  $t = 0$  min, the nuclear envelope of the main nucleus breaks down and the chromosomes (white arrows) are visibly condensed, as shown by their phase-dense appearance in the phase contrast images. However, at this time point, the mnChr does not appear condensed by phase contrast and the fluorescence of the activated PAGFP appears dispersed. During mitosis, the mnChr gradually condenses, but with a substantial delay that prevents its normal movement and segregation. Scale bars, 10  $\mu\text{m}$ . (B) Fluorescence images of prophase cells immunostained for p-H3. The images show cells with progressively increasing levels of p-H3 fluorescence. Cells with intense and widespread p-H3 staining also display significant chromosome condensation, indicative of late prophase stage. Scale bars, 10  $\mu\text{m}$ . (C) p-H3 staining of MNed cells shows differences in fluorescence intensities between the MN and the main nucleus within the same cell. Scale bars, 10  $\mu\text{m}$ . (D) Quantification of normalized (p-H3/DAPI) nucleus/MN fluorescence intensity ratio in MNed cells. The data, reported as mean  $\pm$  s.e.m., are from three independent experiments, with a total of 218 MNed cells analyzed.

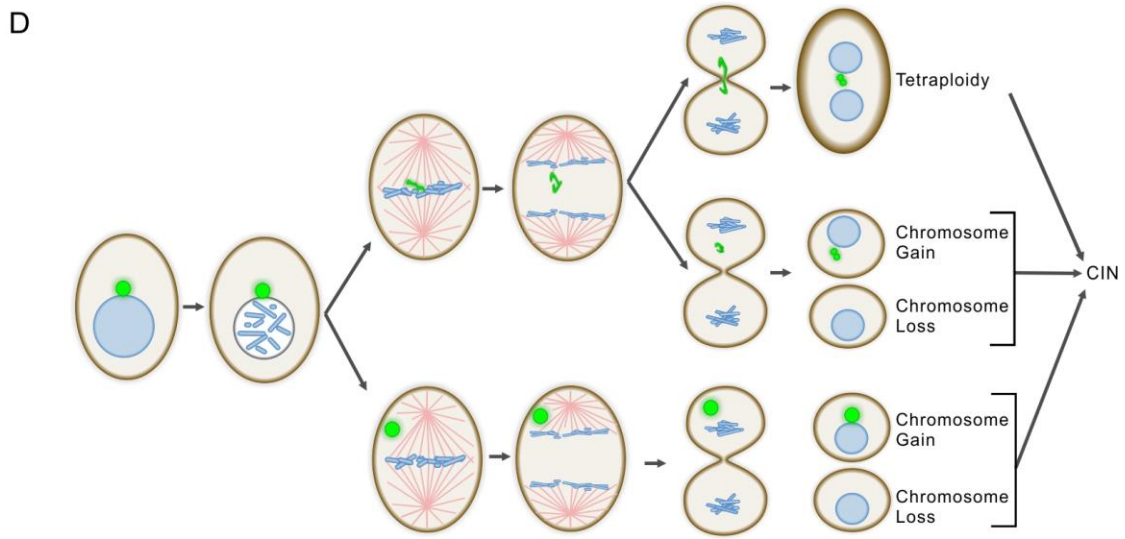
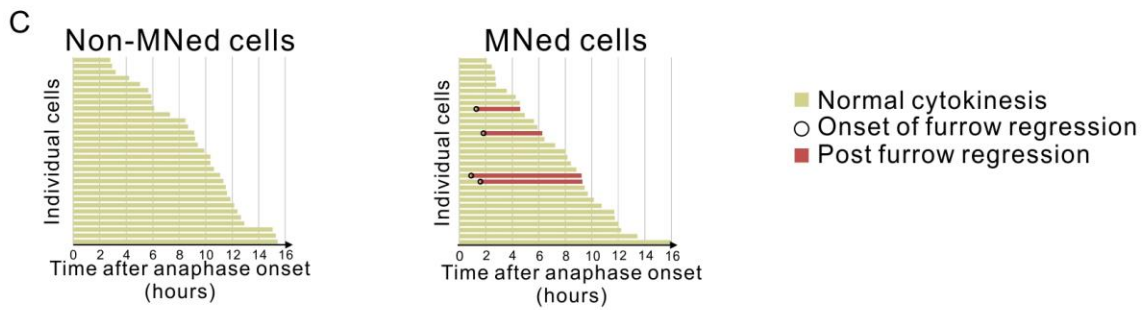
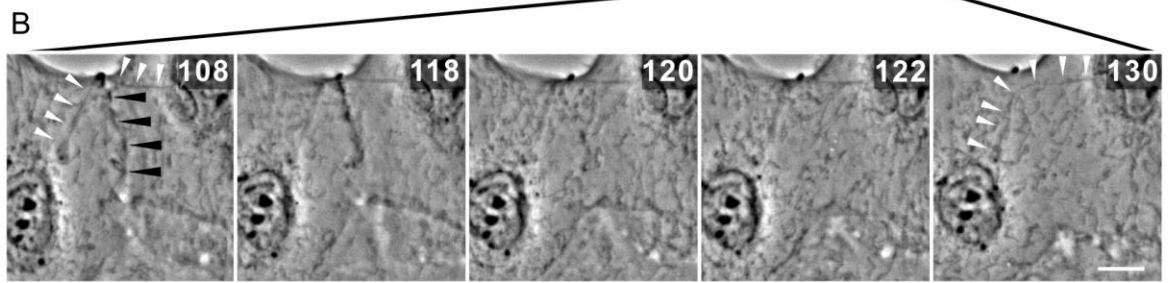
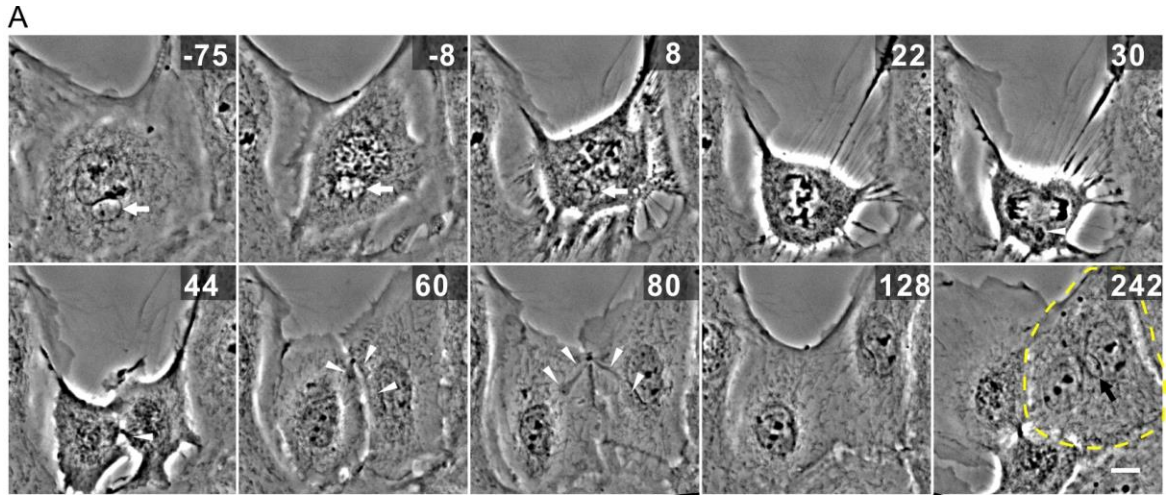


***Figure 4.5. Cytokinesis failure in MNed cells***

(A) Phase contrast still images from time-lapse movie of a MNed PtK1 cell undergoing mitosis and in which an undercondensed chromosome becomes trapped by the cleavage furrow causing furrow regression, and hence cytokinesis failure and tetraploidy. Time stamps indicate elapsed time in minutes. White arrows in the first three frames point at the MN and the mnChr. White arrowheads indicate the chromosome becoming trapped by the cleavage furrow starting at 119 min, and then becoming decondensed and stretched across the midbody region. Eventually, the cleavage furrow regresses, giving rise to a binucleate cell (marked by yellow dashed line in the 317 min frame) with MN (black arrow). (B) Close up view of the cleavage furrow region (black arrowheads) to highlight the time window during which furrow regression occurs. Note the quick disappearance of the cleavage furrow after the 118 min time point. At 130 min, the constriction between the two nuclei is largely relaxed and the trapped chromatin (white arrowheads) has lost its association with the cell cortex and the midbody remnant. (C) Analysis of normal cytokinesis vs. furrow regression in MNed and non-MNed cells. Chromatin trapped in the cleavage furrow was in some cases observed in MNed cells exhibiting cleavage furrow regression. None of the cleavage furrows in non-MNed cells regressed. (D) Schematic summary of the major findings of this study, illustrating the propensity of mnChrs to missegregate at the mitosis following MN formation. Such propensity to missegregate makes MNi a major source of CIN.

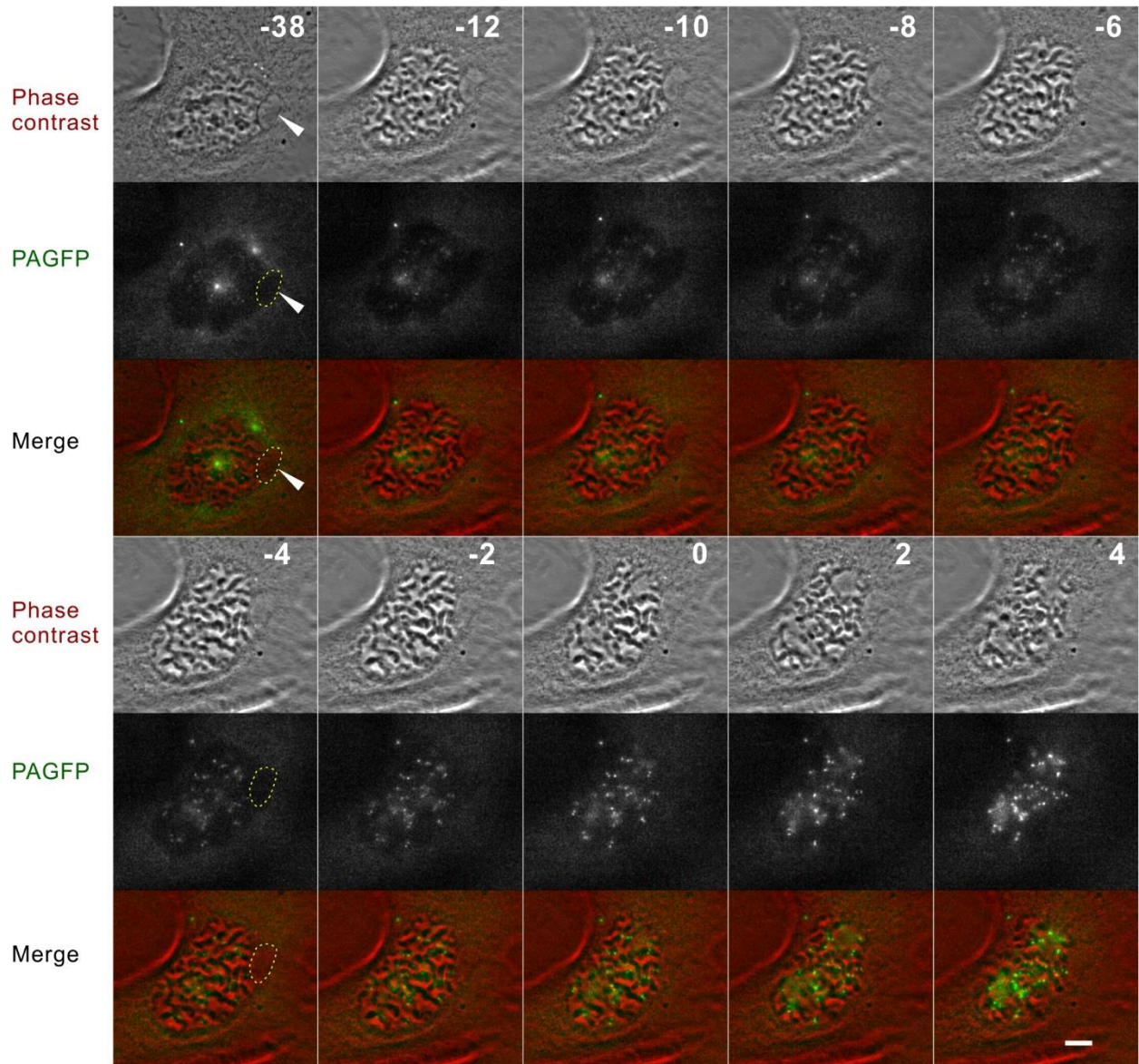
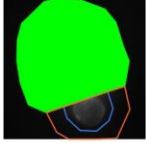
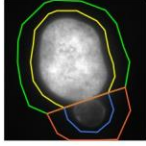
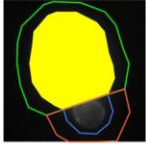


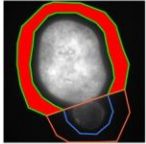
**Figure S4.1. Hec1 loading in MN.** Hec1-GFP PtK1 cell with MN (white arrowhead) imaged during prophase. The white dotted line demarcates the MN boundaries in some of the frames. The time stamps indicate elapsed time in minutes, with 0 min corresponding to nuclear envelope breakdown. No Hec1 can be detected in the MN even at later time points (e.g., -2 min), when significant amounts of Hec1 are associated with the chromosomes within the main nucleus. Scale bar, 5  $\mu$ m.



$A_{outer(N)}$  = area of outer polygon for nucleus  
 $I_{outer(N)}$  = mean fluorescence intensity of outer polygon for nucleus



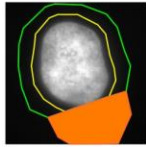
$A_{inner(N)}$  = area of inner polygon for nucleus  
 $I_{inner(N)}$  = mean fluorescence intensity of inner polygon for nucleus



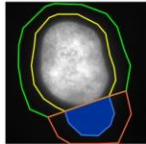
$A_{background(N)} = A_{outer(N)} - A_{inner(N)}$   
 $I_{background(N)} = (A_{outer(N)} \times I_{outer(N)} - A_{inner(N)} \times I_{inner(N)}) \div A_{background(N)}$

$$I\text{-Total}_{(N)} = A_{inner(N)} \times (I_{inner(N)} - I_{background(N)})$$

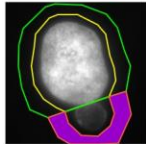
$$Relative\text{-}p\text{-H3}_{(N)} = \frac{I\text{-Total}_{(N)(p\text{-H3})}}{I\text{-Total}_{(N)(DAPI)}}$$



$A_{outer(MN)}$  = area of outer polygon for MN  
 $I_{outer(MN)}$  = mean fluorescence intensity of outer polygon for MN



$A_{inner(MN)}$  = area of inner polygon for MN  
 $I_{inner(MN)}$  = mean fluorescence intensity of inner polygon for MN



$A_{background(MN)} = A_{outer(MN)} - A_{inner(MN)}$   
 $I_{background(MN)} = (A_{outer(MN)} \times I_{outer(MN)} - A_{inner(MN)} \times I_{inner(MN)}) \div A_{background(MN)}$

$$I\text{-Total}_{(MN)} = A_{inner(MN)} \times (I_{inner(MN)} - I_{background(MN)})$$

$$Relative\text{ }p\text{-H3}_{(MN)} = \frac{I\text{-Total}_{(MN)(p\text{-H3})}}{I\text{-Total}_{(MN)(DAPI)}}$$

$$p\text{-H3 nucleus to MN fluorescence intensity ratio} = \frac{Relative\text{-}p\text{-H3}_{(N)}}{Relative\text{-}p\text{-H3}_{(MN)}}$$

Figure S4.2. Description of the method used to quantify p-H3 fluorescence intensity for Figure 4D.

## Chapter 5. Conclusions and future directions

This work established a quantitative model for KT-MT attachment and forces driving chromosome oscillation in PtK1 cells (Chapter 2). The model not only reproduced many aspects of experimentally observed chromosome dynamics, but also made predictions that were confirmed experimentally (Civelekoglu-Scholey et al., 2013). Although our current model can fully reproduce and explain the observed metaphase chromosome/KT behavior, it could be expanded in the future by considering the contribution of motor proteins to chromosome oscillation. Experimental inhibition of motor protein function could be achieved by microinjection of antibodies against -dynein or CENP-E, two KT-associated motor proteins that play important roles in chromosome dynamics in other model systems (Civelekoglu-Scholey et al., 2006).

The model was next used to assist addressing questions on the relationship between spindle dynamics and fidelity of chromosome segregation (Chapter 3). The model predicted that reducing MT poleward flux would result in larger numbers of MTs bound to KTs. This suggests that correction of KT mis-attachments, which relies on turnover of kMTs, would be impaired and therefore higher rates of chromosome mis-segregation would be expected. Indeed, experimental reduction of MT poleward flux, achieved by inhibiting Kif2a, lead to increased rates of chromosome mis-segregation in the form of LCs. FDAP data showed that after Kif2a inhibition, which results in reduced MT poleward flux, the portion of KT-bound MTs was increased, confirming the model prediction. However, the turnover rate of non-KT MTs was slower. This result is surprising because it is not clear how KTs can be bound to more MTs compared to KTs in control cells despite the  $t_{1/2}$  of individual MTs being shorter than that measured in control cells. Our computational model can be used to investigate and explain this discrepancy. Moreover, in order to get a more complete understanding of the role of Kif2a in regulation spindle dynamics, more aspects of mitotic dynamics

could be quantified in Kif2a-inhibited cells. These include oscillation amplitude and period and spindle length at anaphase onset.

An interesting phenomenon observed in chapter 3 is that the presence of a single merotelic attachment strongly correlated with global decrease in the rate of KT poleward movement in early anaphase. The reason of this global effect is an interesting question since it may help us understand possible links between position of a LC and timing of mitotic exit, which may be important for the fate of LC-derived MNi. One possible cause of this global effect could be the cross-linking of the merotelic K-fiber to other K-fibers and inter-polar MTs through motor proteins (e.g., kinesin 5) and/or other microtubule-associated proteins. The mathematical model could be used to test this hypothesis and make predictions that could later tested by designing appropriate experiments.

Although cells have many mechanisms ensuring accurate chromosome segregation, merotelic attachment is known to escape the mitotic checkpoint and when merotelic attachments are not corrected before anaphase onset, they can lead to LCs, which can then form MNi upon mitotic exit. The fate and impact of whole chromosomes mis-segregated into MNi (mnChrs) was the last effort of this work (Chapter 4). About 90% of all mnChrs examined were found to mis-segregate at the mitosis following MN formation. Thus this work established a direct link between LCs and aneuploidy. However, we also found some variability in the behavior of MNi, with some mnChrs condensing much less than others. The reason for this variation is unknown and will be very interesting to investigate in the future. The variation may already arise at the time when MNi form, or even before, when the chromatin lags behind in anaphase. Because LCs are positioned in a region of the cell that normally should be void of chromatin by telophase, they may be surrounded by wrong molecular signals/enzymatic activities, some of which may interfere with de-condensation of the LC and/or formation of the NE around the MN. Aurora B kinase activity could be such a candidate signal. Aurora B kinase activity is high on condensed chromosomes throughout prophase

to metaphase, then at anaphase a phosphorylation gradient is present in the cell cytoplasm with high kinase activity/substrate phosphorylation at the spindle equator and low kinase activity/substrate phosphorylation at the poles, where the chromosomes are positioned (Fuller et al., 2008). Because LCs lag behind at the spindle equator, they will be exposed to high kinase activity, and this may affect chromosome de-condensation or formation of new NE around the LC. It would be interesting to test this hypothesis by altering Aurora B activity. Another approach to study the relationship between location of LC at anaphase and the fate of MN is simply by long term live cell imaging and analysis of MN behavior depending on its position at the time of formation. Parameters like the distance between the LC and the majority of chromosomes at the time of NE reformation, or the distance between the LC and the midbody can be used to describe the location of the LC/MN. The location measurements could then be related to the fate and behavior of mnChr at the following mitosis. Finally, another important issue would be investigating the behavior of mnChr during further rounds of divisions. Long term live cell imaging of MNed cells could be used to monitor cell death rates, segregation defect rates, and mitotic timing through multiple cell cycles. It would also be interesting to test whether segregation defects become more severe during subsequent cell cycles.

## References

- Aist, J., H. Liang, and M. Berns. 1993. Astral and spindle forces in PtK2 cells during anaphase B: a laser microbeam study. *J Cell Sci.* 104:1207-1216.
- Akiyoshi, B., K.K. Sarangapani, A.F. Powers, C.R. Nelson, S.L. Reichow, H. Arellano-Santoyo, T. Gonen, J.A. Ranish, C.L. Asbury, and S. Biggins. 2010. Tension directly stabilizes reconstituted kinetochore-microtubule attachments. *Nature.* 468:576-579.
- Anderson, D.J., and M.W. Hetzer. 2007. Nuclear envelope formation by chromatin-mediated reorganization of the endoplasmic reticulum. *Nat Cell Biol.* 9:1160-1166.
- Anderson, D.J., and M.W. Hetzer. 2008a. The life cycle of the metazoan nuclear envelope. *Current Opinion in Cell Biology.* 20:386-392.
- Anderson, D.J., and M.W. Hetzer. 2008b. Shaping the endoplasmic reticulum into the nuclear envelope. *J Cell Sci.* 121:137-142.
- Anderson, D.J., J.D. Vargas, J.P. Hsiao, and M.W. Hetzer. 2009. Recruitment of functionally distinct membrane proteins to chromatin mediates nuclear envelope formation in vivo. *The Journal of Cell Biology.* 186:183-191.
- Andrews, P.D., Y. Ovechkina, N. Morrice, M. Wagenbach, K. Duncan, L. Wordeman, and J.R. Swedlow. 2004. Aurora B Regulates MCAK at the Mitotic Centromere. *Developmental Cell.* 6:253-268.
- Asbury, C.L., J.F. Tien, and T.N. Davis. 2011. Kinetochores' gripping feat: conformational wave or biased diffusion? *Trends Cell Biol.* 21:38-46.
- Babu, J.R., K.B. Jeganathan, D.J. Baker, X. Wu, N. Kang-Decker, and J.M. van Deursen. 2003. Rae1 is an essential mitotic checkpoint regulator that cooperates with Bub3 to prevent chromosome missegregation. *The Journal of Cell Biology.* 160:341-353.
- Bader, J.R., and K.T. Vaughan. 2010. Dynein at the kinetochore: Timing, Interactions and Functions. *Semin Cell Dev Biol.* 21:269-275.
- Bakhom, S.F., G. Genovese, and D.A. Compton. 2009a. Deviant kinetochore microtubule dynamics underlie chromosomal instability. *Current Biology.* 19:1937-1942.
- Bakhom, S.F., W.T. Silkworth, I.K. Nardi, J.M. Nicholson, D.A. Compton, and D. Cimini. 2014. The mitotic origin of chromosomal instability. *Current biology : CB.* 24:R148-149.
- Bakhom, S.F., S.L. Thompson, A.L. Manning, and D.A. Compton. 2009b. Genome stability is ensured by temporal control of kinetochore-microtubule dynamics. *Nature cell biology.* 11:27-35.
- Barber, T.D., K. McManus, K.W.Y. Yuen, M. Reis, G. Parmigiani, D. Shen, I. Barrett, Y. Nouhi, F. Spencer, S. Markowitz, V.E. Velculescu, K.W. Kinzler, B. Vogelstein, C. Lengauer, and P. Hieter. 2008. Chromatid cohesion defects may underlie chromosome instability in human colorectal cancers. *Proceedings of the National Academy of Sciences.* 105:3443-3448.
- Bonassi, S., M. Fenech, C. Lando, Y.P. Lin, M. Ceppi, W.P. Chang, N. Holland, M. Kirsch-Volders, E. Zeiger, S. Ban, R. Barale, M.P. Bigatti, C. Bolognesi, C. Jia, M. Di Giorgio, L.R. Ferguson, A. Fucic, O.G. Lima, P. Hrelia, A.P. Krishnaja, T.K. Lee, L. Migliore, L. Mikhalevich, E. Mirkova, P. Mosesso, W.U. Muller, Y. Odagiri, M.R. Scarffi, E. Szabova, I. Vorobtsova, A. Vral, and A. Zijno. 2001. HUMAN MicroNucleus project: international database comparison for results with the cytokinesis-block micronucleus assay in human lymphocytes: I. Effect of laboratory protocol, scoring criteria, and host factors on the frequency of micronuclei. *Environmental and molecular mutagenesis.* 37:31-45.
- Bonassi, S., A. Znaor, M. Ceppi, C. Lando, W.P. Chang, N. Holland, M. Kirsch-Volders, E. Zeiger, S. Ban, R. Barale, M.P. Bigatti, C. Bolognesi, A. Cebulska-Wasilewska, E. Fabianova, A. Fucic, L. Hagmar, G. Joksic, A. Martelli, L. Migliore, E. Mirkova, M.R. Scarfi, A. Zijno, H. Norppa, and M. Fenech. 2007. An increased micronucleus frequency in peripheral blood lymphocytes predicts the risk of cancer in humans. *Carcinogenesis.* 28:625-631.
- Boveri, T. 1888. Zellen-Studien. *II Fischer, Jena.*

- Boveri, T. 1914. The Origin of Malignant Tumours.
- Boveri, T. 2008. Concerning the Origin of Malignant Tumours by Theodor Boveri. Translated and annotated by Henry Harris. *J Cell Sci.* 121:1-84.
- Brinkley, B.R. 2001. Managing the centrosome numbers game: from chaos to stability in cancer cell division. *Trends in Cell Biology.* 11:18-21.
- Brust-Mascher, I., and J.M. Scholey. 2002. Microtubule Flux and Sliding in Mitotic Spindles of *Drosophila* Embryos. *Mol. Biol. Cell.* 13:3967-3975.
- Cameron, L.A., G. Yang, D. Cimini, J.C. Canman, O. Kisurina-Evgenieva, A. Khodjakov, G. Danuser, and E. Salmon. 2006. Kinesin 5-independent poleward flux of kinetochore microtubules in PtK1 cells. *The Journal of cell biology.* 173:173-179.
- Canman, J.C., L.A. Cameron, P.S. Maddox, A. Straight, J.S. Tirnauer, T.J. Mitchison, G. Fang, T.M. Kapoor, and E.D. Salmon. 2003. Determining the position of the cell division plane. *Nature.* 424:1074-1078.
- Catalan, J., J. Surrallés, G.C.-M. Falck, K. Autio, and H. Norppa. 2000. Segregation of sex chromosomes in human lymphocytes. *Mutagenesis.* 15:251-255.
- Cheeseman, I.M., J.S. Chappie, E.M. Wilson-Kubalek, and A. Desai. 2006. The Conserved KMN Network Constitutes the Core Microtubule-Binding Site of the Kinetochore. *Cell.* 127:983-997.
- Cheeseman, I.M., and A. Desai. 2008. Molecular architecture of the kinetochore-microtubule interface. *Nat Rev Mol Cell Biol.* 9:33-46.
- Cimini, D. 2007. Detection and Correction of Merotelic Kinetochore Orientation by Aurora B and its Partners. *Cell Cycle.* 6:1558-1564.
- Cimini, D. 2008. Merotelic kinetochore orientation, aneuploidy, and cancer. *Biochimica et Biophysica Acta (BBA) - Reviews on Cancer.* 1786:32-40.
- Cimini, D., L. Cameron, and E. Salmon. 2004. Anaphase spindle mechanics prevent mis-segregation of merotelically oriented chromosomes. *Current biology : CB.* 14:2149 - 2155.
- Cimini, D., and F. Degrossi. 2005. Aneuploidy: a matter of bad connections. *Trends in Cell Biology.* 15:442-451.
- Cimini, D., D. Fioravanti, E.D. Salmon, and F. Degrossi. 2002. Merotelic kinetochore orientation versus chromosome mono-orientation in the origin of lagging chromosomes in human primary cells. *J Cell Sci.* 115:507-515.
- Cimini, D., B. Howell, P. Maddox, A. Khodjakov, F. Degrossi, and E. Salmon. 2001. Merotelic kinetochore orientation is a major mechanism of aneuploidy in mitotic mammalian tissue cells. *J Cell Biol.* 153:517 - 527.
- Cimini, D., B. Moree, J. Canman, and E. Salmon. 2003. Merotelic kinetochore orientation occurs frequently during early mitosis in mammalian tissue cells and error correction is achieved by two different mechanisms. *J Cell Sci.* 116:4213 - 4225.
- Cimini, D., X. Wan, C. Hirel, and E. Salmon. 2006. Aurora kinase promotes turnover of kinetochore microtubules to reduce chromosome segregation errors. *Current biology : CB.* 16:1711 - 1718.
- Civelekoglu-Scholey, G., B. He, M. Shen, X. Wan, E. Roscioli, B. Bowden, and D. Cimini. 2013. Dynamic bonds and polar ejection force distribution explain kinetochore oscillations in PtK1 cells. *The Journal of cell biology.* 201:577-593.
- Civelekoglu-Scholey, G., and J.M. Scholey. 2007. Mitotic motors: kinesin-5 takes a brake. *Current biology.* 17:R544-R547.
- Civelekoglu-Scholey, G., D. Sharp, A. Mogilner, and J. Scholey. 2006. Model of chromosome motility in *Drosophila* embryos: adaptation of a general mechanism for rapid mitosis. *Biophysical journal.* 90:3966-3982.
- Cleveland, D.W., Y. Mao, and K.F. Sullivan. 2003. Centromeres and Kinetochores: From Epigenetics to Mitotic Checkpoint Signaling. *Cell.* 112:407-421.
- Conde, C., and A. Caceres. 2009. Microtubule assembly, organization and dynamics in axons and dendrites. *Nat Rev Neurosci.* 10:319-332.
- Coppin, C.M., D.W. Pierce, L. Hsu, and R.D. Vale. 1997. The load dependence of kinesin's mechanical cycle. *Proc Natl Acad Sci U S A.* 94:8539-8544.

- Courtheoux, T., G. Gay, Y. Gachet, and S. Tournier. 2009. Ase1/Prc1-dependent spindle elongation corrects merotelically during anaphase in fission yeast. *J Cell Biol.* 187:399-412.
- Crasta, K., N.J. Ganem, R. Dagher, A.B. Lantermann, E.V. Ivanova, Y. Pan, L. Nezi, A. Protopopov, D. Chowdhury, and D. Pellman. 2012. DNA breaks and chromosome pulverization from errors in mitosis. *Nature.* 482:53-58.
- D'Ambrosio, C., C.K. Schmidt, Y. Katou, G. Kelly, T. Itoh, K. Shirahige, and F. Uhlmann. 2008. Identification of cis-acting sites for condensin loading onto budding yeast chromosomes. *Genes & development.* 22:2215-2227.
- Dai, W., Q. Wang, T. Liu, M. Swamy, Y. Fang, S. Xie, R. Mahmood, Y.-M. Yang, M. Xu, and C.V. Rao. 2004. Slippage of mitotic arrest and enhanced tumor development in mice with BubR1 haploinsufficiency. *Cancer research.* 64:440-445.
- de Lartigue, J., I. Brust-Mascher, and J.M. Scholey. 2011. Anaphase B spindle dynamics in *Drosophila* S2 cells: Comparison with embryo spindles. *Cell Div.* 6.
- Dechant, R., and M. Glotzer. 2003. Centrosome Separation and Central Spindle Assembly Act in Redundant Pathways that Regulate Microtubule Density and Trigger Cleavage Furrow Formation. 4:333-344.
- Degrassi, F., and C. Tanzarella. 1988. Immunofluorescent staining of kinetochores in micronuclei: a new assay for the detection of aneuploidy. *Mutat Res.* 203:339-345.
- DeLuca, J.G., W.E. Gall, C. Ciferri, D. Cimini, A. Musacchio, and E. Salmon. 2006. Kinetochores microtubule dynamics and attachment stability are regulated by Hec1. *Cell.* 127:969-982.
- Dembo, M., D.C. Torney, K. Saxman, and D. Hammer. 1988. The reaction-limited kinetics of membrane-to-surface adhesion and detachment. *Proc R Soc Lond B Biol Sci.* 234:55-83.
- Desai, A., P.S. Maddox, T.J. Mitchison, and E.D. Salmon. 1998. Anaphase A Chromosome Movement and Poleward Spindle Microtubule Flux Occur At Similar Rates in *Xenopus* Extract Spindles. *The Journal of Cell Biology.* 141:703-713.
- Dewhurst, S.M., N. McGranahan, R.A. Burrell, A.J. Rowan, E. Gronroos, D. Endesfelder, T. Joshi, D. Mouradov, P. Gibbs, R.L. Ward, N.J. Hawkins, Z. Szallasi, O.M. Sieber, and C. Swanton. 2014. Tolerance of whole-genome doubling propagates chromosomal instability and accelerates cancer genome evolution. *Cancer discovery.* 4:175-185.
- Ditchfield, C., V.L. Johnson, A. Tighe, R. Ellston, C. Haworth, T. Johnson, A. Mortlock, N. Keen, and S.S. Taylor. 2003. Aurora B couples chromosome alignment with anaphase by targeting BubR1, Mad2, and Cenp-E to kinetochores. *The Journal of cell biology.* 161:267-280.
- Dobles, M., V. Liberal, M.L. Scott, R. Benezra, and P.K. Sorger. 2000. Chromosome Missegregation and Apoptosis in Mice Lacking the Mitotic Checkpoint Protein Mad2. *Cell.* 101:635-645.
- Dumont, S., E. Salmon, and T.J. Mitchison. 2012. Deformations within moving kinetochores reveal different sites of active and passive force generation. *Science.* 337:355-358.
- Eggert, U.S., T.J. Mitchison, and C.M. Field. 2006. Animal Cytokinesis: From Parts List to Mechanisms. *Annual Review of Biochemistry.* 75:543-566.
- El-Alfy, M., J.P. Turner, N.J. Nadler, D.F. Liu, and C.P. Leblond. 1994. Subdivision of the mitotic cycle into eleven stages, on the basis of the chromosomal changes observed in mouse duodenal crypt cells stained by the DNA-specific feulgen reaction. *The Anatomical Record.* 238:289-296.
- Evans, E. 2001. Probing the relation between force--lifetime--and chemistry in single molecular bonds. *Annu Rev Biophys Biomol Struct.* 30:105-128.
- Fang, G., H. Yu, and M.W. Kirschner. 1998. The checkpoint protein MAD2 and the mitotic regulator CDC20 form a ternary complex with the anaphase-promoting complex to control anaphase initiation. *Genes & Development.* 12:1871-1883.
- Fenech, M. 2000. The in vitro micronucleus technique. *Mutat Res.* 455:81-95.
- Foltz, D.R., L.E.T. Jansen, B.E. Black, A.O. Bailey, J.R. Yates, and D.W. Cleveland. 2006. The human CENP-A centromeric nucleosome-associated complex. *Nat Cell Biol.* 8:458-469.
- Forer, A. 1965. Local reduction of spindle fiber birefringence in living *Nephrotoma suturalis* (Loew) spermatocytes induced by ultraviolet microbeam irradiation. *The Journal of cell biology.* 25:95-117.

- Fuller, B.G., M.A. Lampson, E.A. Foley, S. Rosasco-Nitcher, K.V. Le, P. Tobelmann, D.L. Brautigan, P.T. Stukenberg, and T.M. Kapoor. 2008. Midzone activation of aurora B in anaphase produces an intracellular phosphorylation gradient. *Nature*. 453:1132-1136.
- Funabiki, H., I. Hagan, S. Uzawa, and M. Yanagida. 1993. Cell cycle-dependent specific positioning and clustering of centromeres and telomeres in fission yeast. *The Journal of Cell Biology*. 121:961-976.
- Gaetz, J., and T.M. Kapoor. 2004. Dynein/dynactin regulate metaphase spindle length by targeting depolymerizing activities to spindle poles. *The Journal of cell biology*. 166:465-471.
- Ganem, N.J., and D.A. Compton. 2006. Functional roles of poleward microtubule flux during mitosis. *Cell Cycle*. 5:481-485.
- Ganem, N.J., S.A. Godinho, and D. Pellman. 2009. A mechanism linking extra centrosomes to chromosomal instability. *Nature*. 460:278-282.
- Ganem, N.J., Z. Storchova, and D. Pellman. 2007. Tetraploidy, aneuploidy and cancer. *Curr Opin Genet Dev*. 17:157-162.
- Ganem, N.J., K. Upton, and D.A. Compton. 2005. Efficient mitosis in human cells lacking poleward microtubule flux. *Current biology*. 15:1827-1832.
- Gardner, M.K., and D.J. Odde. 2006. Modeling of chromosome motility during mitosis. *Curr Opin Cell Biol*. 18:639-647.
- Gatlin, J.C., A. Matov, G. Danuser, T.J. Mitchison, and E.D. Salmon. 2010. Directly probing the mechanical properties of the spindle and its matrix. *The Journal of Cell Biology*. 188:481-489.
- Gay, G., T. Courtheoux, C. Reyes, S. Tournier, and Y. Gachet. 2012. A stochastic model of kinetochore-microtubule attachment accurately describes fission yeast chromosome segregation. *J Cell Biol*. 196:757-774.
- Goto, H., Y. Yasui, A. Kawajiri, E.A. Nigg, Y. Terada, M. Tatsuka, K.-i. Nagata, and M. Inagaki. 2003. Aurora-B Regulates the Cleavage Furrow-specific Vimentin Phosphorylation in the Cytokinetic Process. *Journal of Biological Chemistry*. 278:8526-8530.
- Grishchuk, E.L., M.I. Molodtsov, F.I. Ataulakhanov, and J.R. McIntosh. 2005. Force production by disassembling microtubules. *Nature*. 438:384-388.
- Hanks, S., K. Coleman, S. Reid, A. Plaja, H. Firth, D. FitzPatrick, A. Kidd, K. Mehes, R. Nash, N. Robin, N. Shannon, J. Tolmie, J. Swansbury, A. Irrthum, J. Douglas, and N. Rahman. 2004. Constitutional aneuploidy and cancer predisposition caused by biallelic mutations in BUB1B. *Nat Genet*. 36:1159-1161.
- Hanks, S., K. Coleman, B. Summersgill, B. Messahel, D. Williamson, K. Pritchard-Jones, J. Strefford, J. Swansbury, A. Plaja, J. Shipley, and N. Rahman. 2006. Comparative genomic hybridization and BUB1B mutation analyses in childhood cancers associated with mosaic variegated aneuploidy syndrome. *Cancer Letters*. 239:234-238.
- Hatch, E.M., A.H. Fischer, T.J. Deerinck, and M.W. Hetzer. 2013. Catastrophic nuclear envelope collapse in cancer cell micronuclei. *Cell*. 154:47-60.
- Hauf, S., R.W. Cole, S. LaTerra, C. Zimmer, G. Schnapp, R. Walter, A. Heckel, J. van Meel, C.L. Rieder, and J.M. Peters. 2003. The small molecule Hesperadin reveals a role for Aurora B in correcting kinetochore-microtubule attachment and in maintaining the spindle assembly checkpoint. *J Cell Biol*. 161:281-294.
- Hayden, J.H., S.S. Bowser, and C.L. Rieder. 1990. Kinetochores capture astral microtubules during chromosome attachment to the mitotic spindle: direct visualization in live newt lung cells. *The Journal of Cell Biology*. 111:1039-1045.
- Heddle, J.A., and A.V. Carrano. 1977. The DNA content of micronuclei induced in mouse bone marrow by gamma-irradiation: evidence that micronuclei arise from acentric chromosomal fragments. *Mutat Res*. 44:63-69.
- Hetzer, M.W. 2010. The Nuclear Envelope. *Cold Spring Harbor Perspectives in Biology*. 2:a000539.
- Hill, T.L. 1985. Theoretical problems related to the attachment of microtubules to kinetochores. *Proc Natl Acad Sci U S A*. 82:4404-4408.

- Hirano, T., R. Kobayashi, and M. Hirano. 1997. Condensins, Chromosome Condensation Protein Complexes Containing XCAP-C, XCAP-E and a Xenopus Homolog of the Drosophila Barren Protein. *Cell*. 89:511-521.
- Hirota, T., D. Gerlich, B. Koch, J. Ellenberg, and J.-M. Peters. 2004. Distinct functions of condensin I and II in mitotic chromosome assembly. *Journal of cell science*. 117:6435-6445.
- Hoffelder, D.R., L. Luo, N.A. Burke, S.C. Watkins, S.M. Gollin, and W.S. Saunders. 2004. Resolution of anaphase bridges in cancer cells. *Chromosoma*. 112:389-397.
- Hoffman, D.B., C.G. Pearson, T.J. Yen, B.J. Howell, and E.D. Salmon. 2001. Microtubule-dependent changes in assembly of microtubule motor proteins and mitotic spindle checkpoint proteins at ptk1 kinetochores. *Mol Biol Cell*. 12:1995-2009.
- Holland, A.J., and D.W. Cleveland. 2009. Boveri revisited: chromosomal instability, aneuploidy and tumorigenesis. *Nat Rev Mol Cell Biol*. 10:478-487.
- Howard, J. 2001. Mechanics of motor proteins and the cytoskeleton. Sinauer Associates, Publishers, Sunderland, Mass. xvi, 367 p. pp.
- Hoyt, M.A., L. Totis, and B.T. Roberts. 1991. *S. cerevisiae* genes required for cell cycle arrest in response to loss of microtubule function. *Cell*. 66:507-517.
- Huang, Y., H. Hou, Q. Yi, Y. Zhang, D. Chen, E. Jiang, Y. Xia, M. Fenech, and Q. Shi. 2011. The fate of micronucleated cells post X-irradiation detected by live cell imaging. *DNA repair*. 10:629-638.
- Inoue, S., and E. Salmon. 1995. Force generation by microtubule assembly/disassembly in mitosis and related movements. *Mol. Biol. Cell*. 6:1619-1640.
- Janson, M.E., M.E. de Dood, and M. Dogterom. 2003. Dynamic instability of microtubules is regulated by force. *J Cell Biol*. 161:1029-1034.
- Jaqaman, K., E.M. King, A.C. Amaro, J.R. Winter, J.F. Dorn, H.L. Elliott, N. Mchedlishvili, S.E. McClelland, I.M. Porter, M. Posch, A. Toso, G. Danuser, A.D. McAinsh, P. Meraldi, and J.R. Swedlow. 2010. Kinetochore alignment within the metaphase plate is regulated by centromere stiffness and microtubule depolymerases. *The Journal of Cell Biology*. 188:665-679.
- Joglekar, A.P., and J.G. DeLuca. 2009. Chromosome segregation: Ndc80 can carry the load. *Current biology : CB*. 19:R404-407.
- Joglekar, A.P., and A.J. Hunt. 2002. A simple, mechanistic model for directional instability during mitotic chromosome movements. *Biophys J*. 83:42-58.
- Johnson, R.T., and P.N. Rao. 1970. Mammalian cell fusion: induction of premature chromosome condensation in interphase nuclei. *Nature*. 226:717-722.
- Kalitsis, P., E. Earle, K.J. Fowler, and K.H.A. Choo. 2000. Bub3 gene disruption in mice reveals essential mitotic spindle checkpoint function during early embryogenesis. *Genes & Development*. 14:2277-2282.
- Ke, K., J. Cheng, and A.J. Hunt. 2009. The distribution of polar ejection forces determines the amplitude of chromosome directional instability. *Curr Biol*. 19:807-815.
- Khodjakov, A., R.W. Cole, B.F. McEwen, K.F. Buttle, and C.L. Rieder. 1997. Chromosome fragments possessing only one kinetochore can congress to the spindle equator. *The Journal of cell biology*. 136:229-240.
- Khodjakov, A., R.W. Cole, B.R. Oakley, and C.L. Rieder. 2000. Centrosome-independent mitotic spindle formation in vertebrates. *Current Biology*. 10:59-67.
- Khodjakov, A., L. Copenagle, M.B. Gordon, D.A. Compton, and T.M. Kapoor. 2003. Minus-end capture of preformed kinetochore fibers contributes to spindle morphogenesis. *The Journal of Cell Biology*. 160:671-683.
- Kirschner M, M.T. 1986. Beyond self-assembly: from microtubules to morphogenesis. *Cell*. 9:329-342.
- Kline-Smith, S.L., A. Khodjakov, P. Hergert, and C.E. Walczak. 2004. Depletion of centromeric MCAK leads to chromosome congression and segregation defects due to improper kinetochore attachments. *Molecular biology of the cell*. 15:1146-1159.
- Knowlton, A.L., W. Lan, and P.T. Stukenberg. 2006. Aurora B Is Enriched at Merotelic Attachment Sites, Where It Regulates MCAK. *Current Biology*. 16:1705-1710.

- Kops, G.J.P.L., D.R. Foltz, and D.W. Cleveland. 2004. Lethality to human cancer cells through massive chromosome loss by inhibition of the mitotic checkpoint. *Proceedings of the National Academy of Sciences of the United States of America*. 101:8699-8704.
- Koshland, D., and A. Strunnikov. 1996. MITOTIC CHROMOSOME CONDENSATION. *Annual Review of Cell and Developmental Biology*. 12:305-333.
- Kristen M Johansen, J.J. 2007. Cell and Molecular Biology of the Spindle Matrix. *International Review of Cytology*. 263:155-206.
- Kronebusch, P.J., and G.G. Borisy. 1982. Mechanics of anaphase B movement. In *Biological Functions of Microtubules and Related Structures* (ed. H. Sakai, H. Mohri and G. G. Borisy), pp. 233-245. Academic Press: Tokyo.
- LaFountain, J.R., R. Oldenbourg, R.W. Cole, and C.L. Rieder. 2001. Microtubule flux mediates poleward motion of acentric chromosome fragments during meiosis in insect spermatocytes. *Molecular biology of the cell*. 12:4054-4065.
- Lan, W., X. Zhang, S.L. Kline-Smith, S.E. Rosasco, G.A. Barrett-Wilt, J. Shabanowitz, D.F. Hunt, C.E. Walczak, and P.T. Stukenberg. 2004. Aurora B Phosphorylates Centromeric MCAK and Regulates Its Localization and Microtubule Depolymerization Activity. *Current Biology*. 14:273-286.
- Lara-Gonzalez, P., F.G. Westhorpe, and S.S. Taylor. 2012. The spindle assembly checkpoint. *Curr Biol*. 22:R966-980.
- Lee, E.A., M.K. Keutmann, M.L. Dowling, E. Harris, G. Chan, and G.D. Kao. 2004. Inactivation of the mitotic checkpoint as a determinant of the efficacy of microtubule-targeted drugs in killing human cancer cells. *Molecular cancer therapeutics*. 3:661-669.
- Lengronne, A., Y. Katou, S. Mori, S. Yokobayashi, G.P. Kelly, T. Itoh, Y. Watanabe, K. Shirahige, and F. Uhlmann. 2004. Cohesin relocation from sites of chromosomal loading to places of convergent transcription. *Nature*. 430:573-578.
- Lengronne, A., J. McIntyre, Y. Katou, Y. Kanoh, K.-P. Hopfner, K. Shirahige, and F. Uhlmann. 2006. Establishment of sister chromatid cohesion at the S. cerevisiae replication fork. *Molecular cell*. 23:787-799.
- Li, R., and A.W. Murray. 1991. Feedback control of mitosis in budding yeast. *Cell*. 66:519-531.
- Loughlin, R., B. Riggs, and R. Heald. 2008. SnapShot: motor proteins in spindle assembly. *Cell*. 134:548-548. e541.
- Maddox, P., A. Desai, K. Oegema, T.J. Mitchison, and E.D. Salmon. 2002. Poleward microtubule flux is a major component of spindle dynamics and anaphase a in mitotic Drosophila embryos. *Current biology : CB*. 12:1670-1674.
- Maddox, P., A. Straight, P. Coughlin, T.J. Mitchison, and E.D. Salmon. 2003. Direct observation of microtubule dynamics at kinetochores in Xenopus extract spindles implications for spindle mechanics. *The Journal of cell biology*. 162:377-382.
- Magidson, V., C.B. O'Connell, J. Lončarek, R. Paul, A. Mogilner, and A. Khodjakov. 2011. The spatial arrangement of chromosomes during prometaphase facilitates spindle assembly. *Cell*. 146:555-567.
- Maiato, H., J. DeLuca, E.D. Salmon, and W.C. Earnshaw. 2004a. The dynamic kinetochore-microtubule interface. *J Cell Sci*. 117:5461-5477.
- Maiato, H., and M. Lince-Faria. 2010. The perpetual movements of anaphase. *Cellular and Molecular Life Sciences*. 67:2251-2269.
- Maiato, H., C.L. Rieder, and A. Khodjakov. 2004b. Kinetochore-driven formation of kinetochore fibers contributes to spindle assembly during animal mitosis. *The Journal of Cell Biology*. 167:831-840.
- Maresca, T.J., and E.D. Salmon. 2009. Intrakinetochore stretch is associated with changes in kinetochore phosphorylation and spindle assembly checkpoint activity. *J Cell Biol*. 184:373-381.
- May, K.M., and K.G. Hardwick. 2006. The spindle checkpoint. *J Cell Sci*. 119:4139-4142.
- McEwen, B.F., A.B. Heagle, G.O. Cassels, K.F. Buttle, and C.L. Rieder. 1997. Kinetochore Fiber Maturation in PtK1 Cells and Its Implications for the Mechanisms of Chromosome Congression and Anaphase Onset. *The Journal of Cell Biology*. 137:1567-1580.

- McIntosh, J.R., E.L. Grishchuk, M.K. Morphey, A.K. Efremov, K. Zhudenkov, V.A. Volkov, I.M. Cheeseman, A. Desai, D.N. Mastronarde, and F.I. Ataullakhanov. 2008. Fibrils Connect Microtubule Tips with Kinetochores: A Mechanism to Couple Tubulin Dynamics to Chromosome Motion. *135:322-333*.
- McIntosh, J.R., E.L. Grishchuk, and R.R. West. 2002. Chromosome-microtubule interactions during mitosis. *Annu Rev Cell Dev Biol.* 18:193-219.
- McIntosh, J.R., P.K. Hepler, and D.G.V. Wie. 1969. Model for Mitosis. *Nature.* 224:659-663.
- Michel, L.S., V. Liberal, A. Chatterjee, R. Kirchwegger, B. Pasche, W. Gerald, M. Dobles, P.K. Sorger, V.V.V.S. Murty, and R. Benezra. 2001. MAD2 haplo-insufficiency causes premature anaphase and chromosome instability in mammalian cells. *Nature.* 409:355-359.
- Minissi, S., F. Degrossi, C. Tanzarella, and B. Gustavino. 1999. Direct and indirect non-disjunction in the origin of trisomy in cultured human lymphocytes. *Mutagenesis.* 14:557-562.
- Mitchison, T., and M. Kirschner. 1984. Dynamic instability of microtubule growth. *Nature.* 312:237-242.
- Mitchison, T.J. 1989. Polewards microtubule flux in the mitotic spindle: evidence from photoactivation of fluorescence. *The Journal of Cell Biology.* 109:637-652.
- Mogilner, A., R. Wollman, G. Civelekoglu-Scholey, and J. Scholey. 2006. Modeling mitosis. *Trends in cell biology.* 16:88-96.
- Morgan, D.O. 2007. The Cell Cycle: Principles of Control (Primers in Biology). *London:New Science Press Ltd:297*.
- Morrow, C.J., A. Tighe, V.L. Johnson, M.I.F. Scott, C. Ditchfield, and S.S. Taylor. 2005. Bub1 and aurora B cooperate to maintain BubR1-mediated inhibition of APC/CCdc20. *J Cell Sci.* 118:3639-3652.
- Mosch, B., M. Morawski, A. Mittag, D. Lenz, A. Tarnok, and T. Arendt. 2007. Aneuploidy and DNA Replication in the Normal Human Brain and Alzheimer's Disease. *J. Neurosci.* 27:6859-6867.
- Mullins, J., and J. Biesele. 1977. Terminal phase of cytokinesis in D-98S cells. *The Journal of Cell Biology.* 73:672-684.
- Munne, S. 2006. Chromosome abnormalities and their relationship to morphology and development of human embryos. *Reproductive BioMedicine Online.* 12:234-253.
- Munne, S., and J. Cohen. 1998. Chromosome abnormalities in human embryos. *Hum Reprod Update.* 4:842-855.
- Musacchio, A., and E.D. Salmon. 2007. The spindle-assembly checkpoint in space and time. *Nat Rev Mol Cell Biol.* 8:379-393.
- Nasmyth, K., and C.H. Haering. 2009. Cohesin: Its Roles and Mechanisms. *Annual Review of Genetics.* 43:525-558.
- Newport, J. 1987. Nuclear reconstitution in vitro: Stages of assembly around protein-free DNA. *Cell.* 48:205-217.
- Nigg, E.A. 2006. Origins and consequences of centrosome aberrations in human cancers. *International Journal of Cancer.* 119:2717-2723.
- O'Connell, C.B., and A.L. Khodjakov. 2007. Cooperative mechanisms of mitotic spindle formation. *J Cell Sci.* 120:1717-1722.
- Ohi, R., T. Sapra, J. Howard, and T.J. Mitchison. 2004. Differentiation of Cytoplasmic and Meiotic Spindle Assembly MCAK Functions by Aurora B-dependent Phosphorylation. *Mol. Biol. Cell.* 15:2895-2906.
- Onn, I., J.M. Heidinger-Pauli, V. Guacci, E. Ünal, and D.E. Koshland. 2008. Sister Chromatid Cohesion: A Simple Concept with a Complex Reality. *Annual Review of Cell and Developmental Biology.* 24:105-129.
- Palmer, D.K., K. O'Day, H.L. Trong, H. Charbonneau, and R.L. Margolis. 1991. Purification of the centromere-specific protein CENP-A and demonstration that it is a distinctive histone. *Proceedings of the National Academy of Sciences of the United States of America.* 88:3734-3738.
- Paul, R., R. Wollman, W.T. Silkworth, I.K. Nardi, D. Cimini, and A. Mogilner. 2009. Computer simulations predict that chromosome movements and rotations accelerate mitotic spindle assembly without compromising accuracy. *Proceedings of the National Academy of Sciences.* 106:15708-15713.

- Pearson, G., F. Robinson, T. Beers Gibson, B.-e. Xu, M. Karandikar, K. Berman, and M.H. Cobb. 2001. Mitogen-activated protein (MAP) kinase pathways: regulation and physiological functions 1. *Endocrine reviews*. 22:153-183.
- Peters, J.-M. 2006. The anaphase promoting complex/cyclosome: a machine designed to destroy. *Nat Rev Mol Cell Biol*. 7:644-656.
- Peterson, J.B., and H. Ris. 1976. Electron-microscopic study of the spindle and chromosome movement in the yeast *Saccharomyces cerevisiae*. *Journal of cell science*. 22:219-242.
- Pihan, G.A., and S.J. Doxsey. 1999. The mitotic machinery as a source of genetic instability in cancer. *Seminars in Cancer Biology*. 9:289-302.
- Pollard, T.D. 2010. Mechanics of cytokinesis in eukaryotes. *Current Opinion in Cell Biology*. 22:50-56.
- Pollard, T.D., and J.-Q. Wu. 2010. Understanding cytokinesis: lessons from fission yeast. *Nat Rev Mol Cell Biol*. 11:149-155.
- Powers, A.F., A.D. Franck, D.R. Gestaut, J. Cooper, B. Graczyk, R.R. Wei, L. Wordeman, T.N. Davis, and C.L. Asbury. 2009. The Ndc80 kinetochore complex forms load-bearing attachments to dynamic microtubule tips via biased diffusion. *Cell*. 136:865-875.
- Qi, H., U. Rath, Y. Ding, Y. Ji, M.J. Blacketer, J. Girton, J. Johansen, and K.M. Johansen. 2005. EAST interacts with Megator and localizes to the putative spindle matrix during mitosis in *Drosophila*. *Journal of Cellular Biochemistry*. 95:1284-1291.
- Qi, H., U. Rath, D. Wang, Y.-Z. Xu, Y. Ding, W. Zhang, M.J. Blacketer, M.R. Paddy, J. Girton, J. Johansen, and K.M. Johansen. 2004. Megator, an Essential Coiled-Coil Protein that Localizes to the Putative Spindle Matrix during Mitosis in *Drosophila*. *Mol. Biol. Cell*. 15:4854-4865.
- Quintyne, N.J., J.E. Reing, D.R. Hoffelder, S.M. Gollin, and W.S. Saunders. 2005. Spindle multipolarity is prevented by centrosomal clustering. *Science*. 307:127-129.
- Rajagopalan, H., and C. Lengauer. 2004. Aneuploidy and cancer. *Nature*. 432:338-341.
- Ramadan, K., R. Bruderer, F.M. Spiga, O. Popp, T. Baur, M. Gotta, and H.H. Meyer. 2007. Cdc48/p97 promotes reformation of the nucleus by extracting the kinase Aurora B from chromatin. *Nature*. 450:1258-1262.
- Rath, U., D. Wang, Y. Ding, Y.Z. Xu, H. Qi, M.J. Blacketer, J. Girton, J. Johansen, and K.M. Johansen. 2004. Chromator, a novel and essential chromodomain protein interacts directly with the putative spindle matrix protein skeleton. *Journal of Cellular Biochemistry*. 93:1033-1047.
- Rehen, S.K., M.J. McConnell, D. Kaushal, M.A. Kingsbury, A.H. Yang, and J. Chun. 2001. Chromosomal variation in neurons of the developing and adult mammalian nervous system. *Proc Natl Acad Sci U S A*. 98:13361-13366.
- Rehen, S.K., Y.C. Yung, M.P. McCreight, D. Kaushal, A.H. Yang, B.S.V. Almeida, M.A. Kingsbury, K.M.S. Cabral, M.J. McConnell, B. Anliker, M. Fontanoz, and J. Chun. 2005. Constitutional Aneuploidy in the Normal Human Brain. *J. Neurosci*. 25:2176-2180.
- Rieder, C.L. 2005. Kinetochore fiber formation in animal somatic cells: dueling mechanisms come to a draw. *Chromosoma*. 114:310-318.
- Rieder, C.L., and S.P. Alexander. 1990. Kinetochores are transported poleward along a single astral microtubule during chromosome attachment to the spindle in newt lung cells. *The Journal of Cell Biology*. 110:81-95.
- Rieder, C.L., R.W. Cole, A. Khodjakov, and G. Sluder. 1995. The checkpoint delaying anaphase in response to chromosome monoorientation is mediated by an inhibitory signal produced by unattached kinetochores. *The Journal of cell biology*. 130:941-948.
- Rieder, C.L., S. Faruki, and A. Khodjakov. 2001. The centrosome in vertebrates: more than a microtubule-organizing center. *Trends in Cell Biology*. 11:413-419.
- Rieder, C.L., and R. Hard. 1990. Newt lung epithelial cells: cultivation, use, and advantages for biomedical research. *Int Rev Cytol*. 122:153-220.
- Rieder, C.L., and H. Maiato. 2004. Stuck in Division or Passing through: What Happens When Cells Cannot Satisfy the Spindle Assembly Checkpoint. *Developmental Cell*. 7:637-651.

- Rieder, C.L., and E.D. Salmon. 1998. The vertebrate cell kinetochore and its roles during mitosis. *Trends Cell Biol.* 8:310-318.
- Rieder, C.L., A. Schultz, R. Cole, and G. Sluder. 1994. Anaphase onset in vertebrate somatic cells is controlled by a checkpoint that monitors sister kinetochore attachment to the spindle. *The Journal of Cell Biology.* 127:1301-1310.
- Rodriguez-Bravo, V., J. Maciejowski, J. Corona, H.K. Buch, P. Collin, M.T. Kanemaki, J.V. Shah, and P.V. Jallepalli. 2014. Nuclear pores protect genome integrity by assembling a premitotic and Mad1-dependent anaphase inhibitor. *Cell.* 156:1017-1031.
- Rogers, G.C., S.L. Rogers, T.A. Schwimmer, S.C. Ems-McClung, C.E. Walczak, R.D. Vale, J.M. Scholey, and D.J. Sharp. 2004. Two mitotic kinesins cooperate to drive sister chromatid separation during anaphase. *Nature.* 427:364-370.
- Roos, U.-P. 1973a. Light and electron microscopy of Rat kangaroo cells in mitosis. *Chromosoma.* 40:43-82.
- Roos, U.-P. 1976. Light and electron microscopy of rat kangaroo cells in mitosis. *Chromosoma.* 54:363-385.
- Roos, U.P. 1973b. Light and electron microscopy of rat kangaroo cells in mitosis. *Chromosoma.* 41:195-220.
- Salic, A., J.C. Waters, and T.J. Mitchison. 2004. Vertebrate shugoshin links sister centromere cohesion and kinetochore microtubule stability in mitosis. *Cell.* 118:567-578.
- Salmon, E.D., D. Cimini, L.A. Cameron, and J.G. DeLuca. 2005. Merotelic kinetochores in mammalian tissue cells. *Philosophical Transactions of the Royal Society B: Biological Sciences.* 360:553-568.
- Santaguida, S., and A. Musacchio. 2009. The life and miracles of kinetochores. *EMBO J.* 28:2511-2531.
- Saunders, A.M., J. Powers, S. Strome, and W.M. Saxton. 2007. Kinesin-5 acts as a brake in anaphase spindle elongation. *Current Biology.* 17:R453-R454.
- Scholey, J.M., I. Brust-Mascher, and A. Mogilner. 2003. Cell division. *Nature.* 422:746-752.
- Schrader, P. 1944. Mitosis. The movements of the chromosomes in cell division. *New York.*
- Schwartzman, J.-M., R. Sotillo, and R. Benezra. 2010. Mitotic chromosomal instability and cancer: mouse modelling of the human disease. *Nat Rev Cancer.* 10:102-115.
- Sharp, D.J., H.M. Brown, M. Kwon, G.C. Rogers, G. Holland, and J.M. Scholey. 2000. Functional Coordination of Three Mitotic Motors in Drosophila Embryos. *Mol. Biol. Cell.* 11:241-253.
- Shuster, C.B., and D.R. Burgess. 1999. Parameters That Specify the Timing of Cytokinesis. *The Journal of Cell Biology.* 146:981-992.
- Silkworth, W.T., I.K. Nardi, L.M. Scholl, and D. Cimini. 2009. Multipolar Spindle Pole Coalescence Is a Major Source of Kinetochore Mis-Attachment and Chromosome Mis-Segregation in Cancer Cells. *PLoS ONE.* 4:e6564.
- Skibbens, R., V. Skeen, and E. Salmon. 1993. Directional instability of kinetochore motility during chromosome congression and segregation in mitotic newt lung cells: a push-pull mechanism. *The Journal of Cell Biology.* 122:859-875.
- Skibbens, R.V. 2009. Establishment of sister chromatid cohesion. *Current Biology.* 19:R1126-R1132.
- Sluder, G. 2005. Two-way traffic: centrosomes and the cell cycle. *Nat Rev Mol Cell Biol.* 6:743-748.
- Sprague, B.L., C.G. Pearson, P.S. Maddox, K.S. Bloom, E.D. Salmon, and D.J. Odde. 2003. Mechanisms of microtubule-based kinetochore positioning in the yeast metaphase spindle. *Biophys J.* 84:3529-3546.
- Steigemann, P., and D.W. Gerlich. 2009. Cytokinetic abscission: cellular dynamics at the midbody. *Trends in Cell Biology.* 19:606-616.
- Storchova, Z., and C. Kuffer. 2008. The consequences of tetraploidy and aneuploidy. *Journal of cell science.* 121:3859-3866.
- Stumpff, J., Y. Du, C.A. English, Z. Maliga, M. Wagenbach, C.L. Asbury, L. Wordeman, and R. Ohi. 2011. A tethering mechanism controls the processivity and kinetochore-microtubule plus-end enrichment of the kinesin-8 Kif18A. *Mol Cell.* 43:764-775.
- Stumpff, J., M. Wagenbach, A. Franck, C.L. Asbury, and L. Wordeman. 2012. Kif18A and Chromokinesins Confine Centromere Movements via Microtubule Growth Suppression and Spatial Control of Kinetochore Tension. *Dev Cell.* 22:1017-1029.
- Sumner, A.T. 2003. Chromosomes: Organization and Function. *Blackwell Publishing.*

- Svoboda, K., and S.M. Block. 1994. Force and velocity measured for single kinesin molecules. *Cell*. 77:773-784.
- Takata, H., S. Uchiyama, N. Nakamura, S. Nakashima, S. Kobayashi, T. Sone, S. Kimura, S. Lahmers, H. Granzier, S. Labeit, S. Matsunaga, and K. Fukui. 2007. A comparative proteome analysis of human metaphase chromosomes isolated from two different cell lines reveals a set of conserved chromosome-associated proteins. *Genes to Cells*. 12:269-284.
- Tanaka, T.U., and A. Desai. 2008. Kinetochore-microtubule interactions: the means to the end. *Current Opinion in Cell Biology*. 20:53-63.
- Terradas, M., M. Martin, L. Hernandez, L. Tusell, and A. Genesca. 2012. Nuclear envelope defects impede a proper response to micronuclear DNA lesions. *Mutat Res*. 729:35-40.
- Terradas, M., M. Martin, L. Tusell, and A. Genesca. 2009. DNA lesions sequestered in micronuclei induce a local defective-damage response. *DNA repair*. 8:1225-1234.
- Thompson, S.L., and D.A. Compton. 2008. Examining the link between chromosomal instability and aneuploidy in human cells. *The Journal of cell biology*. 180:665-672.
- Thompson, S.L., and D.A. Compton. 2011. Chromosome missegregation in human cells arises through specific types of kinetochore-microtubule attachment errors. *Proc Natl Acad Sci U S A*. 108:17974-17978.
- Toba, S., T.M. Watanabe, L. Yamaguchi-Okimoto, Y.Y. Toyoshima, and H. Higuchi. 2006. Overlapping hand-over-hand mechanism of single molecular motility of cytoplasmic dynein. *Proc Natl Acad Sci U S A*. 103:5741-5745.
- Torosantucci, L., M. De Santis, C. Cenciarelli, W. Rens, and F. Degrossi. 2009. Aneuploidy in mitosis of PtK1 cells is generated by random loss and nondisjunction of individual chromosomes. *J Cell Sci*. 122:3455-3461.
- Tsai, M.-Y., S. Wang, J.M. Heidinger, D.K. Shumaker, S.A. Adam, R.D. Goldman, and Y. Zheng. 2006. A Mitotic Lamin B Matrix Induced by RanGTP Required for Spindle Assembly. *Science*. 311:1887-1893.
- Uchida, K.S., K. Takagaki, K. Kumada, Y. Hirayama, T. Noda, and T. Hirota. 2009. Kinetochore stretching inactivates the spindle assembly checkpoint. *J Cell Biol*. 184:383-390.
- Utani, K., Y. Kohno, A. Okamoto, and N. Shimizu. 2010. Emergence of micronuclei and their effects on the fate of cells under replication stress. *PLoS One*. 5:e10089.
- Valentine, M.T., P.M. Fordyce, T.C. Krzysiak, S.P. Gilbert, and S.M. Block. 2006. Individual dimers of the mitotic kinesin motor Eg5 step processively and support substantial loads in vitro. *Nat Cell Biol*. 8:470-476.
- VandenBeldt, K.J., R.M. Barnard, P.J. Hergert, X. Meng, H. Maiato, and B.F. McEwen. 2006. Kinetochores use a novel mechanism for coordinating the dynamics of individual microtubules. *Curr Biol*. 16:1217-1223.
- Varga, V., J. Helenius, K. Tanaka, A.A. Hyman, T.U. Tanaka, and J. Howard. 2006. Yeast kinesin-8 depolymerizes microtubules in a length-dependent manner. *Nat Cell Biol*. 8:957-962.
- Varga, V., C. Leduc, V. Bormuth, S. Diez, and J. Howard. 2009. Kinesin-8 motors act cooperatively to mediate length-dependent microtubule depolymerization. *Cell*. 138:1174-1183.
- Verde, F., M. Dogterom, E. Stelzer, E. Karsenti, and S. Leibler. 1992. Control of microtubule dynamics and length by cyclin A- and cyclin B-dependent kinases in *Xenopus* egg extracts. *J Cell Biol*. 118:1097-1108.
- Vladimirou, E., E. Harry, N. Burroughs, and A.D. McAinsh. 2011. Springs, clutches and motors: driving forward kinetochore mechanism by modelling. *Chromosome Res*. 19:409-421.
- Wadsworth, P., and A. Khodjakov. 2004. E pluribus unum: towards a universal mechanism for spindle assembly. *Trends in cell biology*. 14:413-419.
- Walker, D.L., D. Wang, Y. Jin, U. Rath, Y. Wang, J. Johansen, and K.M. Johansen. 2000. Skeletor, a Novel Chromosomal Protein That Redistributes during Mitosis Provides Evidence for the Formation of a Spindle Matrix. *The Journal of Cell Biology*. 151:1401-1412.

- Walker, R., and M. Sheetz. 1993. Cytoplasmic microtubule-associated motors. *Annual review of biochemistry*. 62:429-451.
- Walker, R.A., E.T. O'Brien, N.K. Pryer, M.F. Soboeiro, W.A. Voter, H.P. Erickson, and E.D. Salmon. 1988. Dynamic instability of individual microtubules analyzed by video light microscopy: rate constants and transition frequencies. *The Journal of Cell Biology*. 107:1437-1448.
- Wan, X., D. Cimini, L.A. Cameron, and E. Salmon. 2012. The coupling between sister kinetochore directional instability and oscillations in centromere stretch in metaphase PtK1 cells. *Molecular biology of the cell*. 23:1035-1046.
- Wan, X., R.P. O'Quinn, H.L. Pierce, A.P. Joglekar, W.E. Gall, J.G. DeLuca, C.W. Carroll, S.-T. Liu, T.J. Yen, B.F. McEwen, P.T. Stukenberg, A. Desai, and E.D. Salmon. 2009. Protein Architecture of the Human Kinetochore Microtubule Attachment Site. *Cell*. 137:672-684.
- Weaver, B.A.A., and D.W. Cleveland. 2006. Does aneuploidy cause cancer? *Current Opinion in Cell Biology*. 18:658-667.
- Weaver, B.A.A., A.D. Silk, C. Montagna, P. Verdier-Pinard, and D.W. Cleveland. 2007. Aneuploidy Acts Both Oncogenically and as a Tumor Suppressor. 11:25-36.
- Weinberg, R.A. 2006. The Biology of Cancer. *Garland Science*.
- Wheatley, S.P., and Y. Wang. 1996. Midzone microtubule bundles are continuously required for cytokinesis in cultured epithelial cells. *The Journal of Cell Biology*. 135:981-989.
- Wignall, S.M., R. Deehan, T.J. Maresca, and R. Heald. 2003. The condensin complex is required for proper spindle assembly and chromosome segregation in *Xenopus* egg extracts. *The Journal of Cell Biology*. 161:1041-1051.
- Williams, B.R., V.R. Prabhu, K.E. Hunter, C.M. Glazier, C.A. Whittaker, D.E. Housman, and A. Amon. 2008. Aneuploidy Affects Proliferation and Spontaneous Immortalization in Mammalian Cells. *Science*. 322:703-709.
- Xiong, B., and J.L. Gerton. 2010. Regulators of the Cohesin Network. *Annual Review of Biochemistry*. 79.
- Yadav, V., and S. Mukherji. 2011. Length-dependent dynamics of microtubules. *Physical review. E, Statistical, nonlinear, and soft matter physics*. 84:062902.
- Yang, A.H., D. Kaushal, S.K. Rehen, K. Kriedt, M.A. Kingsbury, M.J. McConnell, and J. Chun. 2003. Chromosome Segregation Defects Contribute to Aneuploidy in Normal Neural Progenitor Cells. *J. Neurosci*. 23:10454-10462.
- Yu, H. 2002. Regulation of APC-Cdc20 by the spindle checkpoint. *Current Opinion in Cell Biology*. 14:706-714.
- Yu, R., W. Lu, J. Chen, C.J. McCabe, and S. Melmed. 2003. Overexpressed Pituitary Tumor-Transforming Gene Causes Aneuploidy in Live Human Cells. *Endocrinology*. 144:4991-4998.
- Zhai, Y., P.J. Kronebusch, and G.G. Borisy. 1995. Kinetochore microtubule dynamics and the metaphase-anaphase transition. *The Journal of cell biology*. 131:721-734.
- Zhang, N., G. Ge, R. Meyer, S. Sethi, D. Basu, S. Pradhan, Y.-J. Zhao, X.-N. Li, W.-W. Cai, A.K. El-Naggar, V. Baladandayuthapani, F.S. Kittrell, P.H. Rao, D. Medina, and D. Pati. 2008. Overexpression of Separase induces aneuploidy and mammary tumorigenesis. *Proceedings of the National Academy of Sciences*. 105:13033-13038.
- Zheng, Y., and M.-Y. Tsai. 2006. The Mitotic Spindle Matrix: A Fibro-Membranous Lamin Connection *Cell Cycle*. 5:2345-2347.
- Zhou, H., J. Kuang, L. Zhong, W.-I. Kuo, J. Gray, A. Sahin, B. Brinkley, and S. Sen. 1998. Tumour amplified kinase STK15/BTAK induces centrosome amplification, aneuploidy and transformation. *Nat Genet*. 20:189-193.